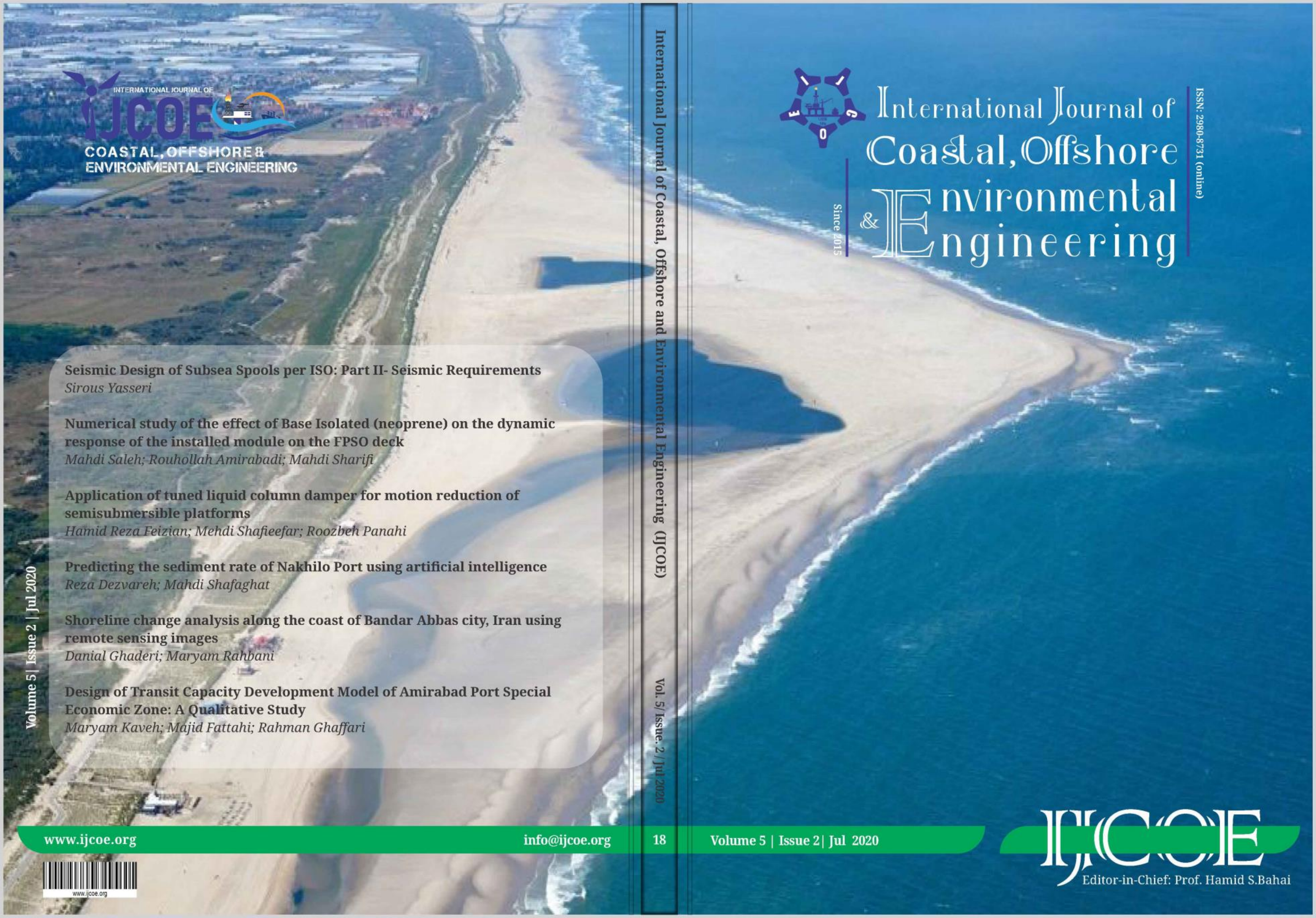

INTERNATIONAL JOURNAL OF
IJCOE
COASTAL, OFFSHORE &
ENVIRONMENTAL ENGINEERING

Seismic Design of Subsea Spools per ISO: Part II- Seismic Requirements
Sirous Yasseri

Numerical study of the effect of Base Isolated (neoprene) on the dynamic response of the installed module on the FPSO deck
Mahdi Saleh; Rouhollah Amirabadi; Mahdi Sharifi

Application of tuned liquid column damper for motion reduction of semisubmersible platforms
Hamid Reza Feizian; Mehdi Shafieefar; Roozbeh Panahi

Predicting the sediment rate of Nakhilo Port using artificial intelligence
Reza Dezvareh; Mahdi Shafaghat

Shoreline change analysis along the coast of Bandar Abbas city, Iran using remote sensing images
Danial Ghaderi; Maryam Rahbani

Design of Transit Capacity Development Model of Amirabad Port Special Economic Zone: A Qualitative Study
Maryam Kaveh; Majid Fattahi; Rahman Ghaffari

Volume 5| Issue 2 | Jul 2020

www.ijcoe.org **info@ijcoe.org**

www.ijcoe.org

International Journal of Coastal, Offshore and Environmental Engineering (IJCOE)

Vol. 5/ Issue. 2 / Jul 2020

18

International Journal of Coastal, Offshore & Environmental Engineering

Since 2015

ISSN: 2980-8731 (online)

Volume 5 | Issue 2| Jul 2020

IJCOE

Editor-in-Chief: Prof. Hamid S.Bahai

International Journal of
Coastal, Offshore
& Environmental
Engineering
Since 2015
ISSN: 2980-8731 (online)

In The Name of God

Message from the Editor-in-Chief

The IJCOE journal office was established in 2015,and its first issue was published in 2016. TheIJCOE covers a wide range of research in thefields of oceanography & ocean technology, aswell as marine industries & marine engineering.The editorial board of IJCOE consists of nearly130 of the greatest scientists and researchersfrom over 30 countries worldwide, and thejournal's review board comprises 1,000 membersfrom all five continents. The membership andapplication process for joining the editorial andreview boards of this journal is ongoing. IJCOE isa research-academic quarterly journal that haspublication and distribution permissions fromthe Press Organization and permission topublish scientific-research articles from theMinistry of Science, Research, and Technology(MSRT) with an "A" rating. It also holds a "Q1"rating from the ISC institute with an impactfactor (IF) of approximately 0.43 and isconsidered a "core journal" (prestigious andoutstanding journal). IJCOE is an open-accessjournal and allows the download and receipt ofaccepted articles in full text for free. It respectsand adheres to copyright and COPE regulations.The journal's office operates 24/7, providingservices to researchers. In addition to publishinga regular quarterly journal, IJCOE has 16 specialissues on specific topics in preparation. It alsoprovides conditions for publishing specializedbooks, references, and handbooks. Moreover, itis ready to cooperate with the secretariats ofreputable international conferences to publishtheir selected and outstanding articles. IJCOEevaluates, appraises, and publishes books,articles, and the scientific achievements andfindings of esteemed researchers and scientistsworldwide who are innovating and conductingin-depth research in the "important and strategicfield of the maritime technology & Oceanengineering." It welcomes any form of jointcooperation with universities, research institutes,and related research centers at the national,regional, and international levels, and extends ahand for collaboration.

Classification of Editorial Board in IJCOE

Editor-in-Chief

Director-in-Chief

Deputy Editor

Executive Managers

English Text Editor

Technical Editor

International Editorial Board

National Editorial Board

Editorial Board Associate

Editorial Board Assistant

Guest Editorial Board

Advisory Board

Administrative Coordinator

Honorary Board Member

Methodology Advisor

Author Benefits

- Open Access
- Rapid Publication
- Thorough Peer-Review
- No Copyright Constraints
- Coverage by Leading Indexing Services
- Discounts On Article Processing Charges (APC)
- No Space Constraints, No restriction on the maximum length of the papers, number of figures or colors

INTERNATIONAL JOURNAL OF
IJCOE
COASTAL, OFFSHORE &
ENVIRONMENTAL ENGINEERING

Aims of IJCOE

Hydrodynamics

Marine equipment

Structural mechanics

Ocean environmental predictions

Stochastic calculations Experimental

Automatic Control of Marine Systems

Scope of IJCOE

Marine Hazards

Ocean Acoustics

Naval Architecture

Ocean Engineering

Coastal Engineering

Marine Meteorology

Marine Earth Sciences

Underwater Technology

Marine Renewable Energy

Polar & Arctic Engineering

Marine Renewable Energy

Marine Geography & Geodesy

Marine Environmental Engineering

Automatic Control of Marine Systems

Hydro Physics & Physical Oceanography

Type of papers

- Case Studies
- Book Reviews
- Review Article
- Letters to the Editor
- Methodology Papers
- Editorials and Commentaries
- Response or Rejoinder Papers
- Perspective or Opinion Papers
- Conceptual or Theoretical Papers
- Meta-Analysis and Systematic Reviews
- Short Communications or Brief Reports
- Research Articles (Original Research Papers)

Scientific Research Journal

Ministry of Science, Research And Technology (MSRT)

Jurnal Ranking 2023: A

Ministry Of Science, Research And Technology (ISC)

Citation Impact 2022: 0.429

Quartile 2022 : Q1

Core Collection

IJCOE is a Member of

- CIVILICA
- Google Scholar
- Jouroscope
- COPE
- ISC
- JREF.IR
- DOAJ DIRECTORY OF OPEN ACCESS JOURNALS
- ISSN
- Researcher.Life
- doi Crossref mEDRA
- iThenticate
- magiran
- OPEN ACCESS
- pistetn
- ResearchGate
- Regional Information Center for Science and Technology RICEST
- ScienceGate
- Scilit
- SID
- website.informer.com
- WEBrate

Cantact Us

Office 1 | Research Institute of Meteorology and Atmospheric Science

Address | Tehran, Shahid Kharrazi Highway, Pajoohesh Blvd, Research Institute of Meteorology and Atmospheric Science, Sand and Dust Storm International Research Center (SDS-IRC), No. 13, 1st floor.

Phone | +982144787652

Postal code | 13611-14977

website | www.rimac.ac.ir

Office 2 | Iranian National Institute for Oceanography and Atmospheric Science

Address | Tehran, Dr. Fatemi Gharbi St., Shahid Etemadzade St., No. 3, third floor.

Phone | +982166944873

Postal code | 13389 – 14118

website | www.inio.ac.ir

Email | Info@ijcoe.org

Website | www.ijcoe.org

Follow Us

www.ijcoe.org

INTERNATIONAL JOURNAL OF IJCOE COASTAL, OFFSHORE & ENVIRONMENTAL ENGINEERING

Volume & Issue:

Volume 5, Issue 2, July 2020

Number of Articles: 6

Content

Seismic Design of Subsea Spools per ISO: Part II- Seismic Requirements 1
Sirous Yasseri

Numerical study of the effect of Base Isolated (neoprene) on the dynamic response of the installed module on the FPSO deck 15
Mahdi Saleh; Rouhollah Amirabadi; Mahdi Sharifi

Application of tuned liquid column damper for motion reduction of semisubmersible platforms 23
Hamid Reza Feizian; Mehdi Shafieefar; Roozbeh Panahi

Predicting the sediment rate of Nakhilo Port using artificial intelligence 41
Reza Dezvareh; Mahdi Shafaghat

Shoreline change analysis along the coast of Bandar Abbas city, Iran using remote sensing images 51
Danial Ghaderi; Maryam Rahbani

Design of Transit Capacity Development Model of Amirabad Port Special Economic Zone: A Qualitative Study 65
Maryam Kaveh; Majid Fattahi; Rahman Ghaffari

INTERNATIONAL JOURNAL OF
COASTAL & OFFSHORE ENGINEERING

IJCOE Vol.5/No. 2/Summer 2020 (1-13)

Available online at www.ijcoe.org

Seismic Design of Subsea Spools per ISO:

Part II- Seismic Requirements

Sirous F. Yasseri

Brunel University London; Sirous.Yasseri@Brunel.ac.uk;

ARTICLE INFO

Article History:
Received: 28 Aug. 2020
Accepted: 09 Dec. 2020

Keywords:
Subsea Spools
Soil- spool interaction
ISO 19902
ISO 19901
Earthquake
ALE and ELE

ABSTRACT

The ISO requires a two-level seismic qualification, namely Extreme Level Earthquake (ELE) and Accidental Level Earthquake (ALE) where damages that do not lead to leak is acceptable. ISO accepts both the response spectrum method and the time history approach. Since the spool-soil system behaves non-linearly, the time domain analyses must be performed for both levels. ISO requires 7 real earthquakes scaled for the site to be used for each seismic level and the system must pass at least 50% of the cases.

Best estimate soil models were developed to represent soil conditions at the manifolds locations in Part I. A set of 10 real earthquake time histories were propagated through the soil column for each location. The resulting ground motion at the surface was computed using a nonlinear model. The frequency-dependent ratio of spectra acceleration at the mudline to the stiff soil outcrop spectral acceleration (Spectral Amplification Ratio or SAR) was computed for each time history. The mean SAR was then used to modify the stiff soil hazard results from the PSHA to obtain design response spectra at the mudline.

This is the second part of three interlinked papers summarises the state of art for the benefit of practitioners of subsea engineering.

1. Introduction

This is the second part of a three-part paper dealing with the seismic design of subsea spools [32 and 33]. The seismic requirements for offshore structure design are covered in ISO 19901-2 and 19902. ISO balances the reliability and the potential consequences of undesirable performance. ISO methodology considers different soil, geologic conditions, and seismotectonic regions, and it is sensitive to input data and can account for the site characteristics uncertainties.

ISO requires each installation to withstand two earthquake intensity levels with prescribed acceptable performance. The first level is an Extreme Level Earthquake (ELE). The return period of the ELE depends on the commercial consequences of the installation's poor performance, which should have a reasonably low likelihood of being exceeded during the installation's service life. Installations should be designed so that little or no damage occurs when subjected to the ELE. Two objectives of the ELE design are,

- the ELE should ensure that the design is not susceptible to damage during relatively frequent seismic shaking at the site, and
- The design for ELE should endow enough strength revere to minimize the design changes required to meet the performance criteria of the Abnormal Level Earthquake (ALE).

The second level is ALE, which is a rare, intense earthquake with a very low probability of being exceeded during the life of the installation. The ALE design check is performed using nonlinear analysis methods with the performance objective being the life safety and protection of the environment, but significant damage is acceptable. ISO criteria allow the use of a site-specific probabilistic seismic hazard analysis to define these two events. Doing this requires:

- Review geotechnical data for spools and manifold locations.
- Definition of soil amplification models for the manifold locations;
- Site response analysis to determine amplification/de-amplification of ground motion for ALE and 10,000 year return periods;
- Utilize amplification factors to define elastic response spectra at mudline for ALE and

10,000 year return periods. Define ELE mudline spectra based on Cr factor;

- Extract amplified acceleration time histories at mudline, and 15 m and 30 m below seafloor acceleration for the manifold location.

The method of analysis is straightforward. Best estimate soil models were developed to represent soil conditions at manifold locations. A set of 10 real earthquake time histories were propagated through the soil column for each location. The resulting ground motion at the surface was computed using a nonlinear model. The frequency-dependent ratio of spectra acceleration at the mudline to the stiff soil outcrop spectral acceleration (Spectral Amplification Ratio or SAR) was computed for each time history.

The mean SAR was then used to modify the stiff soil hazard results from the PSHA to obtain design response spectra at the mudline. As SAR is nonlinear with the intensity of ground shaking, the analysis is repeated for each return period scaling the input time histories of the target stiff soil PGA.

Acceleration time histories were also developed for the design. Seven earthquake accelerograms were considered. The horizontal components of the records were propagated through the soil profile and the corresponding motions extracted at mudline, 15 m, and 30 m penetration. The vertical motions are not expected to be significantly altered by the soil column and the original motions may be considered. The horizontal and vertical components were then scaled to the design elastic response spectra in the range of fundamental period of the structure (1 to 3 s for horizontal, 0.50 to 0.75 s for vertical). Time history data are provided for the ELE, ALE, and 10,000 year return periods.

2. ISO19902 Methodology

Annex B of ISO 1992-2 contains 1,000-year rock outcrop spectral acceleration associated with a single degree of freedom oscillator period of 0.2s and 1.0 second for worldwide locations. This information is used to determine the seismic load, especially for those sites that the simplified seismic design and analysis are acceptable. The site seismic zone is then determined from Table 1. Spectral acceleration $S_{a,map}(1.0)$ as shown in the ISO Worldwide Seismic Maps [ISO 19902-2 [16]]is used to define the site seismic zone.

Table1: Site Seismic Zone according to ISO 19902-2 [16]

$S_{a,map}(1,0)$	< 0,03 *g*	0,03 *g* to 0,10 *g*	0,11 *g* to 0,25 *g*	0,26 *g* to 0,45 *g*	> 0,45 *g*
Seismic zone	0	1	2	3	4

ISO then requires deciding the exposure level according to Table 2. The installation exposure level is defined in terms of the target annual probability of failure. Here, L1 is for the high consequence and L3 is for low consequence failure and if there is no pollution potential. (L2 is being removed in the updated code.)

Table 2: Relationship between exposure level and the annual probability of failure (Table 1 of ISO)

Exposure level	P_f (annual probability of failure)
L1	$4 \times 10^{-4} = 1 / 2{,}500$
L2	$1 \times 10^{-3} = 1 / 1{,}000$
L3	$2.5 \times 10^{-3} = 1 / 400$

Table 3 defines the seismic risk categories using the exposure level and the seismic zone category.

Table3: Seismic Risk Categories (ISO 19901-2)

Site seismic zone	Exposure level		
	L3	L2	L1
0	SRC 1	SRC 1	SRC 1
1	SRC 2	SRC 2	SRC 3
2	SRC 2	SRC 2	SRC 4
3	SRC 2	SRC 3	SRC 4
4	SRC 3	SRC 4	SRC 4

There is no requirement to conduct a seismic evaluation and for the risk category SCR 1 and SRC 2, thus the simplified method can be used. The standard procedure that adapts a standardized seismic hazard graph (Figure 2 of ISO 19902 [16]- the Code's response spectrum) can be used which simplifies calculations. For SRC 3 case, either the simplified or the detailed approach may be used. Depending on the seismic risk category the simplified method may produce a conservative design, thus it is best to use the detailed method. For SRC 4 the detailed method must be used.

For structures that are classified as seismic risk Category 3 or 4, it is recommended that the design response acceleration spectra be developed by detailed probabilistic seismic hazard analysis.

3. Probabilistic Seismic Risk Assessment

The probabilistic seismic assessment consists of the following elements:

- Development of earthquake **source-zonation** models
- Development of **earthquake recurrence relationships** and maximum magnitudes for each earthquake source zone
- Selection of appropriate **strong-motion attenuation** relationships
- Explicit incorporation of aleatory (randomness) and epistemic (modeling) **variability and uncertainty**
- **Probabilistic seismic hazard analyses** (PSHA)
- Development of generic and site-specific seismic design criteria

These elements are summarized below and in the flow chart given in Figure 1. The first three elements represent what is referred to as a seismotectonic model.

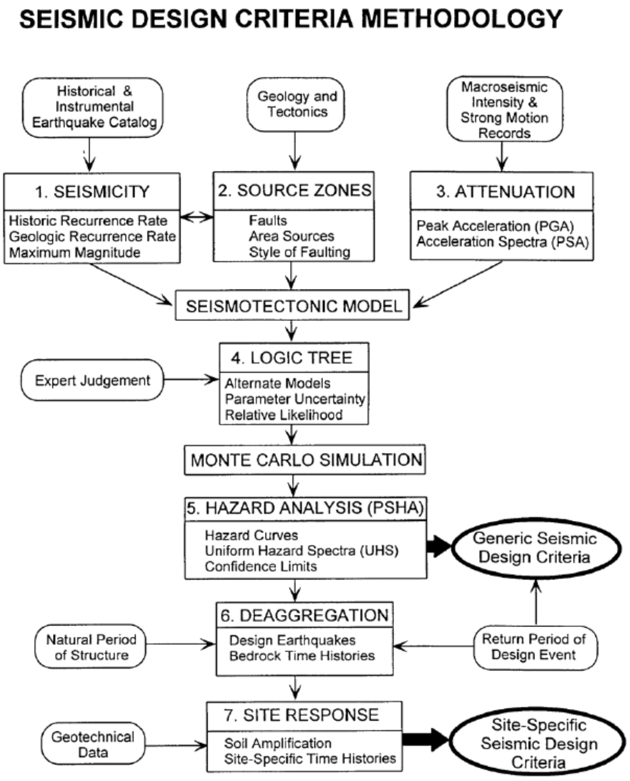

Figure 1: Flow chart showing the elements of the seismic design criteria methodology

3.1. Earthquake Source Zonation

Earthquake source zones are faults or seismotectonic provinces in which earthquakes are assumed to occur randomly with the same rate per unit length for fault sources or rate per unit area for area sources. The development of earthquake source zones entails identifying seismogenic sources—active faults or regions of diffuse seismicity. These sources are modeled as either individual faults or areas of similar seismicity and tectonic setting. Individual faults are modeled as three-dimensional vertical or dipping planes to properly account for the distribution of earthquake rupture with depth. Area sources also contain model faults that are assumed to be uniformly distributed concerning location and orientation (i.e. strike). Seismogenic sources are identified from information on the geology, tectonics, and historical seismicity of the region.

3.2. Earthquake Recurrence Relationship

Earthquake recurrence relationships quantify the frequency and size of earthquakes that are expected to occur in each earthquake source zone. Earthquake recurrence rates are estimated using the truncated exponential recurrence relationship originally proposed by Cornell and Vanmarcke [5]. Maximum magnitudes for individual faults are computed from relationships between earthquake magnitude and rupture dimensions developed by Wells and Coppersmith [31]. Maximum magnitudes for the area or distributed fault sources are estimated from historical seismicity, regional tectonics, the maximum lengths of mapped faults.

3.3. Strong Motion Attenuation

Attenuation relationships are used to predict strong ground-motion parameters from earthquake source and wave-propagation characteristics in the region of interest. The selected attenuation relationships are chosen to represent as closely as possible the tectonic environment of the earthquake source regions and the local site conditions of interest. An appropriate reference site condition is chosen for each site of interest to select a specific set of attenuation relationships to use in the seismic hazard analysis

3.4. Variability and Uncertainty

There are two types of variability—aleatory and epistemic—that can be included in a PSHA. Aleatory variability accounts for randomness associated with the size, location, and frequency of earthquakes together with other random effects inherent to the prediction of a parameter from a specific model assuming that the model is correct. Modeling uncertainty is a primary reason for inadequate predictive models and the variability in the employed data used for the models. Aleatory variability is included directly in the PSHA calculations utilizing mathematical integration. PSHA includes epistemic uncertainty which is done by explicitly including alternative hypotheses and models through the construction of a logic tree, and sampling the logic tree by a simulation method such as the Monte Carlo approach.

Each alternative hypothesis in the logic tree is given a subjective weight corresponding to its estimated likelihood of being correct. These alternative hypotheses will account for uncertainty in earthquake source zonation, maximum magnitude, recurrence rate, location and segmentation of seismogenic faults, type of faulting, distribution of seismicity between faults and area sources, as well as the ground-motion attenuation relationships[29].

3.5. Probabilistic Seismic Hazard Analysis (PSHA)

The hazard or probability of exceedance of a specified value of ground motion is calculated for each alternative hypothesis and set of model parameters selected utilizing Monte Carlo sampling of the logic-tree using a computational methodology similar to that first proposed by Cornell [6].

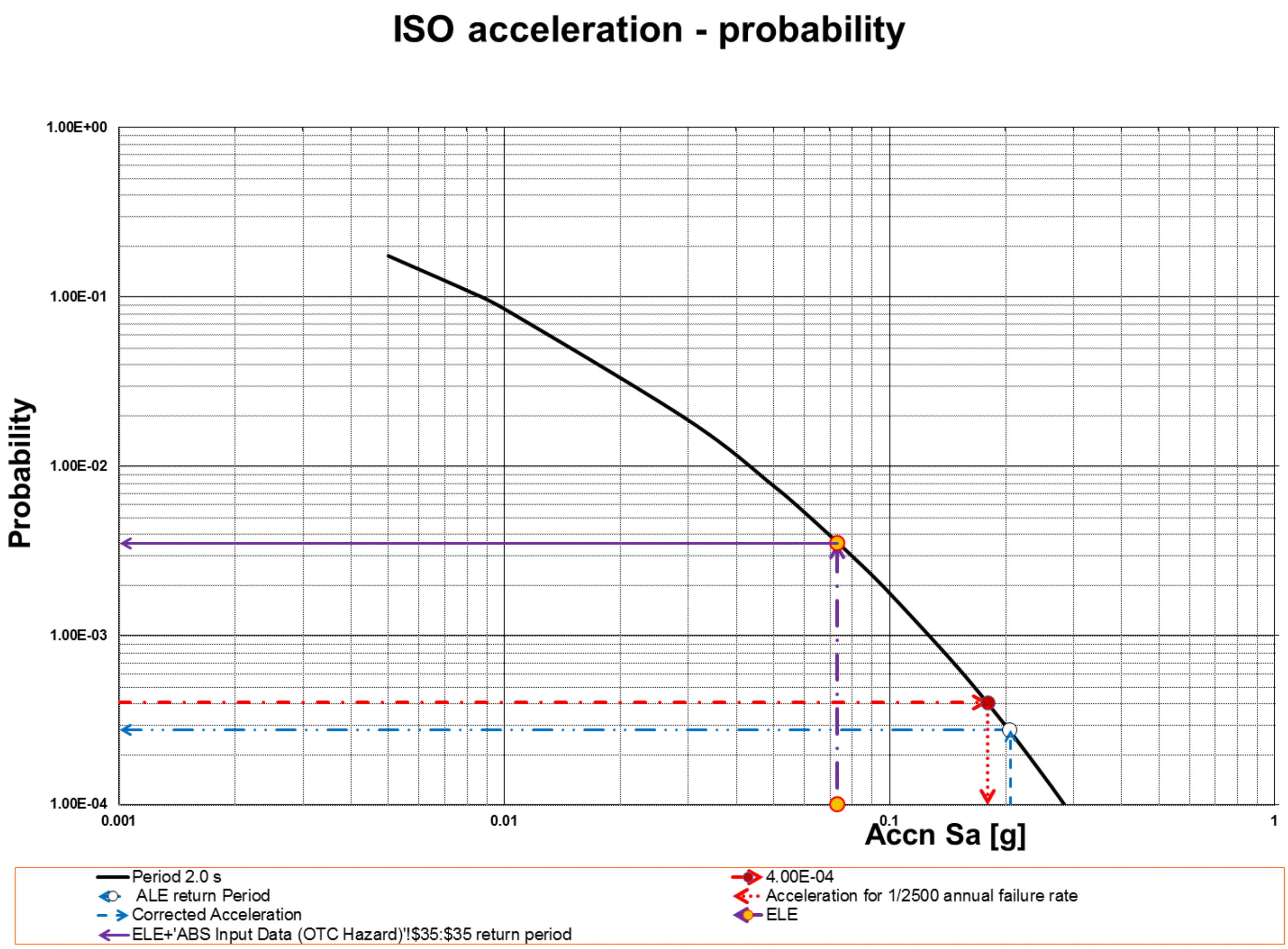

ISO 19902 and ISO 19901-2 Return Period Derivation

NB: Assumed Values

Exposure Levels L1, L2 and L3 :
Section 6.6 and Table 6.6.1, p. 20 to 22

L1 SD-Alpha Tdom = ~ 7 secs (?)

L1 SD-Beta Tdom = ~ 4 secs (?)

L2 - L3 (?) Manifold Tdom = ~ 0.5 secs (?) (Ref. Cooper, 2005)

Ref: *"ISO Seismic Design Guidelines for Offshore Platforms"*
Banon, H., Cornell, C.A., Crouse, C.B., Marshall, P.W. and Nadim, F.
20th Offshore Mechanics and Arctic Engineering Conf. - OMAE 2001
Rio de Janeiro, Brazil, 3rd - 8th June 2001

Notes:

Pf =	**Probability of Failure**	
SRC =	**Seismic Risk Category**	
aR =	**Seismic Hazard Curve Slope**	ISO 19901-2 Figs 4 [a&b] p. 20 & 21
Cc =	**Correction Factor**	ISO 19901-2 Table 10 p. 19
Cr =	**Seismic Reserve Capacity Factor**	ISO 19902 Table 11.3.1 p. 61
Tdom =	**Structure Dominant Modal Period**	ISO 19901-2 Sec. 8.4 p. 19

*Sa, ALE (Tdom) = Cc * Sa, pf (Tdom)*

Sa, ELE (Tdom) = Sa, ALE (Tdom) / Cr

Refs.
1. BS EN ISO 19901-2: Petroleum and Natural Gas Industries - Specific Requirements for Offshore Structures — Part 2: Seismic Design Procedures and Criteria
2. BS EN ISO 19902: 20 Petroleum and Natural Gas Industries - Fixed Steel Offshore Structures

ISO 19902 and 19901-2 Input Constants **ISO 19901-2 Site Seismic Zone 3**

NB: Rounded Values

ISO 19901- Exposure Level	pf	SRC	aR [0,5 s]	Cc [0.5 s]	aR [4.0 s]	Cc [4.0 s]	Cr	ISO Class; Tdom	Sa, pf	Sa, ALE	Sa, ELE	ALE RP	ELE RP
L1	4 × 10−4 = 1/2 500	4	1.80	1.19	2.15	1.141	2.8	L1; 4.0 secs	0.068g	0.074g	0.0260g	2.8 × 10−4 = 1/3600	3.3 × 10−3 = 1/300
							[2.4]	L1; 4.0 secs	0.068g	0.074g	0.0308g	2.8 × 10−4 = 1/3600	2.20 x 10-3 = 1/450
							2.8	L1: 2.0 secs	0.170g	0.202g	0.072g	3.0 x 10-4 = 1/3300	3.5 x 10-3 = 1/285
							[2.4]	L1: 2.0 secs	0.170g	0.202g	0.084g	3.0 x 10-4 = 1/3300	2.6 x 10-3 = 1/385
L2	1 × 10−3 = 1/1 000	3	1.90	1.17	2.30	1.132	2.5	L2; 0.5 secs	0.400g	0.468g	0.187g	6.7 × 10−4 = 1/1500	6.7 x 10-3 = 1/150
L3	2.5 × 10−3 = 1/400	2	2.00	1.15	2.65	1.114	2.0	L3; 0.5 secs	0.280g	0.322g	0.161g	2 × 10−3 = 1/500	1 x 10-2 = 1/100

Figure 2: Typical Seismic Hazard Curve for T = T_{dom}

The input to the PSHA analyses is selected using the Monte Carlo simulation. The results of the simulations are then used to determine ground-shaking amplitudes and response spectra for specified fractiles as a function of the return period. Because of the complexity of the calculations, the probabilistic seismic hazard analyses are performed using a computer software package specifically developed to be used with a logic-tree formulation.

3.6. Re-aggregation of PSHA Results

The development of time histories for input to the dynamic site-response analysis requires knowledge of the magnitudes and distances that dominate the calculated ground-shaking hazard at the return periods and structural periods of interest. These magnitudes and distances define the design earthquakes and are determined from a process referred to as "de-aggregation." For this purpose, the hazard for a given return period is partitioned into several magnitudes and distance bins. Then the relative contribution to the hazard in each bin is determined by the division of the bin exceedance frequency and the total exceedance frequency of all bins. The 'mode' is the bins with the largest relative contributions, that identify those earthquakes that are the largest contributors to the total hazard. If no clear modes emerge as the dominant one, then the design earthquakes are generally defined by the mean magnitude and mean distance. Time histories are then chosen that are consistent with the magnitudes and distances of these design or controlling, earthquakes[29].

The PSHA results are "de-aggregated" to determine the magnitudes and distances that contribute to the calculated exceedance frequencies (i.e., the hazard) for a given return period. These results are typically displayed as a histogram giving the percent contribution to the specified hazard of those earthquakes that are capable of causing ground motions equal to or greater than corresponding to this hazard as affected by the magnitude and distance [29].

Such histograms would be distinct for spectral accelerations of varying structural periods due to the difference in the way these spectral values scale with magnitude and distance [29]. The relative frequencies specified by these histograms are used to develop mean estimates of magnitude and distance to define a set of controlling or design earthquakes corresponding to specified structural periods and return periods. These design earthquakes are then used to select bedrock time histories for use in a dynamic site-response analysis or ground-failure evaluation.

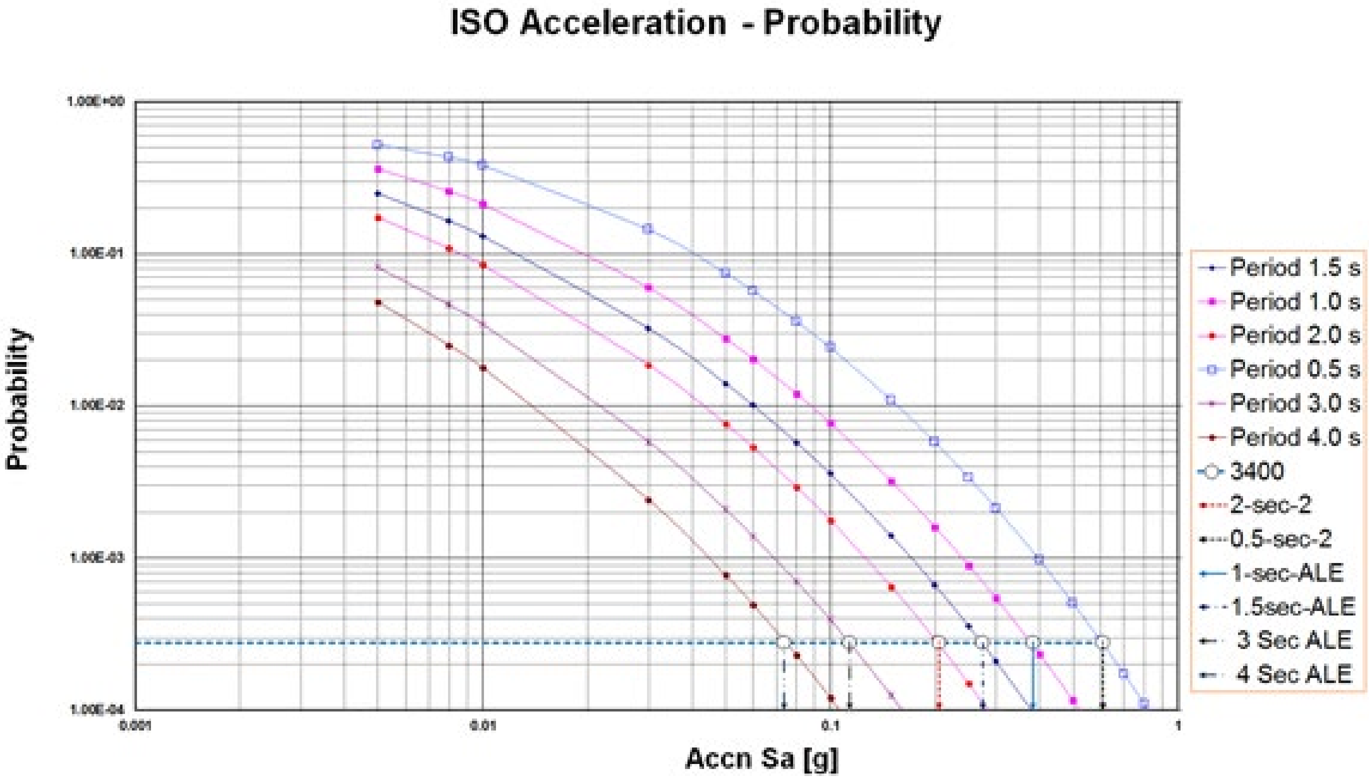

Figure 3: ISO Acceleration - Probability

4. Uniform Hazard Spectra

The design response spectrum for abnormal level earthquake and extreme level earthquake are derived using the uniform hazard response spectrum (UHS), which is explained in the next section. The dominant modal period of the structure to be designed, T_{dom}, is determined first. The site-specific mean uniform hazard spectral accelerations for T_{dom}, is plotted on a logarithmic scale (Figure2) This plot is used to determine the site-specific spectral acceleration at Pf, Sa, P_f (T_{dom}). The slope of the tangent at P_f termed aR, is defined as the ratio of the spectral accelerations corresponding to two probabilities that are on either side of Pf and which are one order of magnitude apart, P1 & P2, as seen in Figure 3.

The ISO procedures are as follows:

- For the given dominant period, T_{dom} , 2 seconds for the (or use 1.0 s if T_{dom} is not available) spool considered, the curve of exceedance probability Pe(Sa) as a function of response acceleration Sa is plotted in log-log scale as shown in Figure 3.
- For the selected exposure level (L1), the failure probability p_f is defined (i.e., 1/2500).
- At p_e = p_f, the ratio (a_R) of S_{a1}(with probability exceedance of p_1=E-4) to S_{a2}(with probability exceedance of p2=E-3) is determined such that p_2/p1 =10 and p1 < p_f < p2.
- A correction factor, Cc, is introduced per the value of a_R as per ISO (Table 4).
- At the dominant period, T_{dom}, the ALE response spectrum value $S_{A,ALE}$ = CcSa(with probability exceedance of p_f). The annual probability of exceedance for the ALE can be read from the seismic hazard curve or uniform seismic response spectra.
- At the spool's dominant period, T_{dom}, the ELE response spectrum value $S_{A,ELE}$ = $S_{A,ALE}$/C_r. The annual probability of exceedance for the ELE can be read from the seismic hazard curve or uniform seismic response spectra. C_r is the seismic reserve capacity.
- Based on the determined annual probability of exceedance for the ELE or ALE, the uniform hazard response spectra $S_{A,ELE(T)}$, and $S_{A,ALE(T)}$ are determined.

Table 4 Correction factor Cc (Table 3-6 of ISO 1990-2)

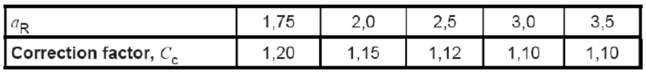

a_R	1,75	2,0	2,5	3,0	3,5
Correction factor, C_c	1,20	1,15	1,12	1,10	1,10

Table 3-6. Correction Factor, Cc [ISO 19901-2].

5. Static and Dynamics Soil properties

The ground response to seismic shaking depends on the stiffness of the soil column, as well as the nonlinear decay of stiffness and level of damping versus strain developed during the seismic event. In terms of site response, the main parameters to be defined are:

- Soil unit weight;
- Shear modulus at small strain Gmax, or equivalently the shear wave velocity Vs;
- Decay of shear stiffness with the strain;
- Soil damping properties.

The submerged unit weight is a key parameter for the effective stress site response analysis. The small strain shear modulus (Gmax) strongly influences the dynamic response of the soil column. The evaluation of Gmax was based on the results of in-situ and laboratory testing. The small strain shear modulus (Gmax) is related to the shear wave velocity (Vs) and soil density (ρ) as:

$$G_{max} = \rho V_s^2 \qquad (1)$$

Laboratory results are compared to modulus decay and damping curves proposed by Vucetic and Dobry [30] for zero plasticity index, Ishibashi, and Zhang [17] and the low, average, and high curves suggested by Seed et al. [28]. The Vucetic and Dobry [30] curve is seen to provide the best match to the laboratory data. It was asserted by many researchers that laboratory tests indicate damping ratios rapidly decreases if shear strains are higher than about 1%. This behavior is consistent with the findings of Matasovic and Vucetic [22 and 23]. These authors have shown that at large strains sand tends to exhibit a dilatative behavior, then the hysteresis loop is no longer elliptical and the tendency of the stress-strain curve (the so-called "S shaping") leads to a rapid drop of hysteretic damping. For each applied cyclic stress ratio (CSR), the corresponding number of cycles at failure was determined. There was some dispersion in test results, therefore, upper and lower bound estimate curves are proposed. Considering a characteristic earthquake magnitude of about 7.5 the predicted equivalent number of cycles at failure according to Seed et al. [27] (as cited in Kramer [19]) would be of the order of 15. The corresponding CSR at failure is around 0.16 for the proposed lower bound profile

6. Seismic time histories

Seismic hazard was evaluated using a formal

defines ground motion for a postulated stiff soil outcrop with shear wave velocity from 200 to 375 m/s. Mean uniform hazard spectra (UHS) on stiff soil were defined for ALE and ELE design levels corresponding to 240 and 3,500 year periods, respectively.

The PSHA hazard curves were used to develop stiff soil spectra for 3,400 years (ALE). Following ISO recommendations, the ELE stiff soil spectra were

computed dividing the ALE spectra ordinates by the seismic reserve capacity factor Cr, assumed to be 2.8. The equivalent return period for the ELE event is 240 years, which satisfies the ISO requirement of the minimum 200 year return period for this condition. Note that several approximations were required for the definition of return periods: the assessment was based on spectral period 2 s using simplified assumptions regarding the slope of the hazard curves.

Figure 4 shows UHS for stiff soil outcrop conditions. The data refer to the geometric mean of two components of horizontal ground motion computed for 5% damping. The corresponding spectral ordinates are listed in Table 5.

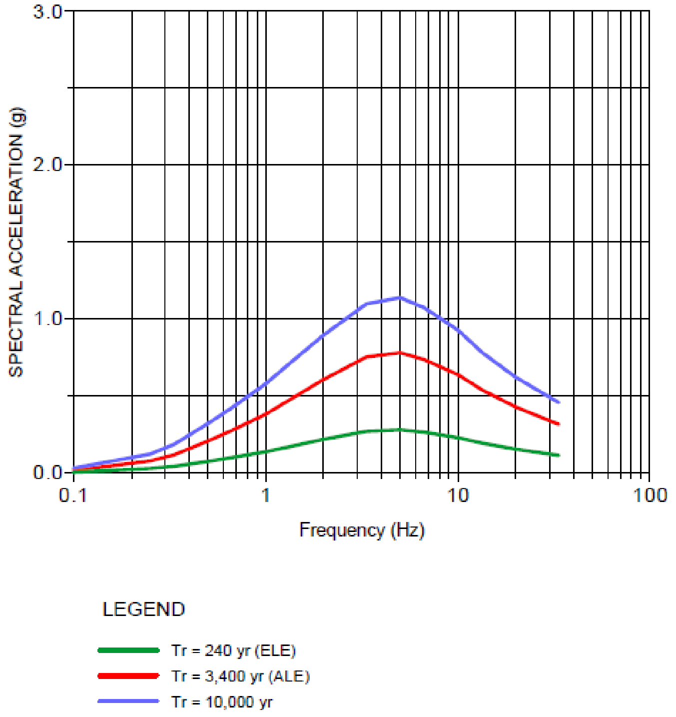

Figure 4: Stiff soil uniform spectra

A correction factor, Cc, is applied to a_R to account for the uncertainties that are not depicted in the seismic hazard curve. The values of Cc are found in Table 4

Table 5: 5% Damped Horizontal UHS, Stiff Soil Outcrop

FREQUENCY(Hz)	PERIOD(s)	SPECTRAL ACCELERATION (g)		
		ELE	ALE	10,000 yr
PGA (assumed 33Hz)	PGA	0.112	0.314	0.456
20	0.05	0.152	0.426	0.619
13.33	0.08	0.192	0.538	0.781
10	0.1	0.227	0.636	0.926
6.67	0.15	0.262	0.734	1.071
5	0.2	0.278	0.779	1.137
3.33	0.3	0.268	0.751	1.096
2	0.5	0.216	0.606	0.895
1.33	0.75	0.169	0.474	0.711
1	1	0.136	0.38	0.578
0.67	1.5	0.098	0.274	0.422
0.5	2	0.073	0.205	0.319
0.33	3	0.041	0.116	0.184
0.25	4	0.027	0.076	0.12
0.1	10	0.002	0.014	0.03

6.1. Design time histories

A set of 7 suitable earthquake strong-motion time histories is selected for the nonlinear site response analysis. These earthquake records were chosen to cover the range of magnitude and distance of the hazard de-aggregation. All of the time histories were recorded on stiff soil sites per the PSHA. The normalized selected time histories provide coverage of the UHS on stiff soil as shown in Figure 5. All of the time histories were recorded on stiff soil sites per the PSHA. Table 6 lists the time history components used in the analysis.

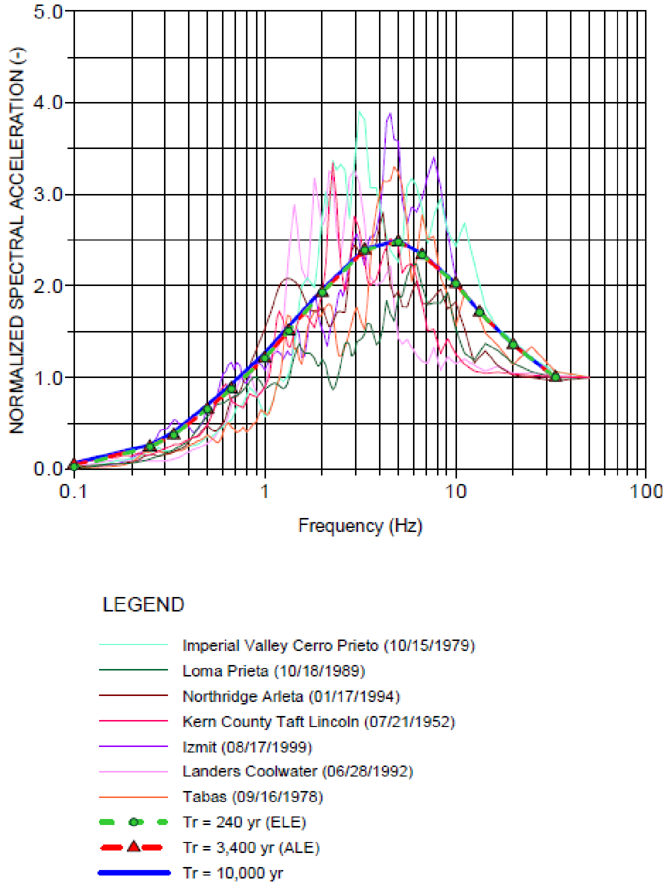

Figure 5: Normalised response spectra of time histories

6.2. Geotheictical model

The behavior of soil under cyclic loading is complex. In general soils exhibit, a nonlinear stress-strain response in that material stiffness decreases for increasing levels of strain. These effects are accentuated in seismic conditions as cyclic loading causes additional degradation of modulus and changes in pore-water pressures. Finally, the soil is inelastic for significant strain levels, meaning that it exhibits different stiffness in loading and unloading conditions.

Table 6: Earthquake time histories for analysis

EVENT	STATION	MAG	DIST (km)	COMP.	PGA (g)
Kern County (USA) 07/21/1952	Taft Lincoln School Tunne	7.4	43.5	Y	0.18
Loma Prieta (USA) 10/18/1989	Saratoga-Aloha Ave	6.9	27.6	X	0.51
Northridge (USA) 01/17/1994	Arleta-Nordhoff Ave. Fire Station	6.7	9.9	X	0.34
Tabas (Iran) 09/16/1978	Tabas	7.4	52.0	Y	1.10
Imperial Valley (USA) 10/15/1979	Cerro Prieto	6.5	26.7	X	0.17
Landers (USA) 06/28/1992	Desert Hot Spring	7.3	23.0	X	0.17
Izmit (Turkey) 08/17/1999	Goynuk-Delvet Hastanesi	7.6	73.0	X	0.14

This inelastic response leads to hysteretic damping, which is again dependent on the level of strain.

The main aspects of soil behavior under cyclic loading were modeled for the numerical analysis. The constitutive model's components include:

- stress-strain response for initial loading (backbone curve) represented by modified Hyperbolic model;
- unloading-reloading behavior and hysteretic damping captured using an extended Masing rule [21];
- modulus degradation in clays considering the number of load cycle and strain levels;
- pore pressure generation-modulus degradation model for sands correlated to energy dissipation.

Specific details of the model are not discussed in this paper.

6.3. Site-specific response

The probabilistic seismic hazard assessment determines the earthquake ground motion for a competent stiff soil outcrop. Stiff soil conditions may be encountered at significant depth. The presence of soft sediments in the shallow soil profile will significantly modify ground shaking, amplifying, and/or de-amplifying motions depending on the specific frequency. Site response was evaluated using a nonlinear analysis performed with the DEEPSOIL software (Hashash et al., [11]). As illustrated in Figure 6 the soil profile is represented as a series of infinite horizontal layers overlying an elastic bedrock. The individual soil layers are represented using a multi-degree of freedom lumped parameter model. Layer thicknesses were selected to ensure the model correctly represented soil behavior up to frequencies of at least 33 Hz. The nonlinear dynamic equation of motion is solved in the time domain using the Newmark β method.

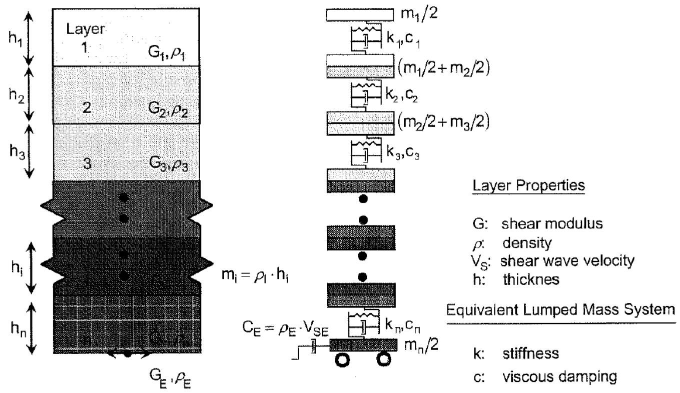

Figure 6: Lumped parameter model- From Hashash et al., [11]

Nonlinear soil behavior is represented using a pressure-dependent hyperbolic model (Konder and Zelasko [18], 1963; Matasovic and Vucetic [22 and 23]; Hashash and Park [12]. Energy losses are modeled with a combination of hysteretic damping utilizing a modified Masing [21] approach shown in Figure 7 (Darendeli [9]; Phillips and Hashash [25] and small strain Rayleigh viscous damping (Park and Hashash [24]).

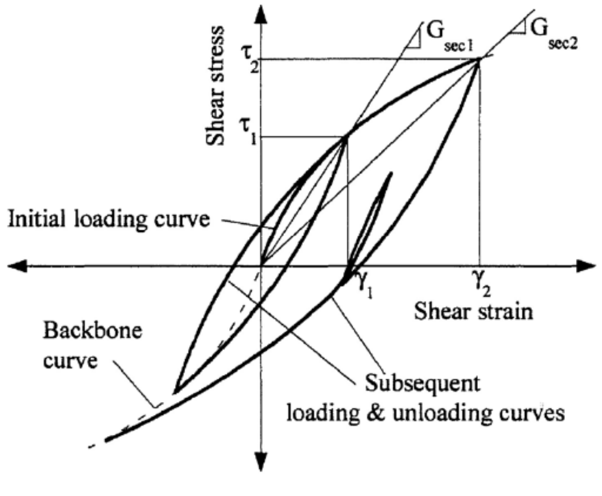

Figure 7: Hyperbolic model with extended Masing rule [21]- see Darandeli [9], and Phillips and Hashash [25]

The basic approach is to develop a numerical model of the soil column and subject it to an input competent outcrop ground motion. The input motion is assumed to consist of vertically propagating horizontal shear waves. The dynamic response of the soil column is evaluated to find the motion at the ground surface. The response spectrum of ground motion at the ground surface is computed. The frequency-dependent spectral amplification ratio (SAR) is then computed for the record as:

$$SAR(f) = \frac{S_a(f)^{surface}}{S_a(f)^{input}} \qquad (2)$$

SAR Spectral amplification ratio as a function of

$S_a(f)^{surface}$ Spectral acceleration at ground surface or mudline

$S_a(f)^{input}$ input equivalent outcrop ground motion

The 7 horizontal acceleration time-histories are propagated through the soil column, and SAR values are computed for each record. The average response of the soil column, considering the record to record variability, is represented by the mean of the SAR values from the individual records.

The stiff soil UHS is adjusted for the effects of site response using the mean SAR values. The response spectrum at the surface is computed as:

$$S_a(f)^{surface} = S_a(f)^{input} \times \overline{SAR(f)} \qquad (3)$$

$\overline{SAR(f)}$ mean spectral amplification ratio as a function of frequency f

Formally, this approach should be applied to adjust individual frequency-dependent hazard curves, and the resulting response spectrum interpolated for the desired return periods. An acceptable engineering approximation is to factor the stiff soil UHS directly to obtain the motion at the mudline.

As site response is nonlinear with the level of the earthquake ground shaking, the SAR values must be defined as a function of the intensity of the input motion. For this study, SAR values have been defined for the target return periods by scaling the input time histories to the desired stiff soil PGA.

The vertical spectral acceleration at a period T according to ISO 19901-2 [14] should be half of the corresponding horizontal spectral acceleration. No additional reductions for water depth effects are considered.

The ISO approach was compared to the results of recent research regarding vertical spectra for both onshore and offshore locations. Several teams of researchers have addressed the issue of the ratio of vertical to horizontal spectral acceleration (V/H) for onshore locations. Bozorgnia and Campbell [4] examined the V/H ratio based on predictions of vertical and horizontal spectral acceleration from their previously developed attenuation laws (Campbell and Bozorgnia [8]. Gülerce and Abrahamson [10] performed a similar evaluation but regressing directly the V/H ratios using the extensive NGA database of shallow crustal measurements. Bommer et al. [2] confirmed the Gülerce and Abrahamson's [10] results utilizing a different dataset of European and the Middle East events. The results of all three groups showed the ratio V/H to be less than one half for periods exceeding about 0.5 s. Higher ratios are expected onshore for shorter periods and events relatively near the site.

Boore and Smith [3] provide data applicable to offshore locations. They present the results of 20 years of monitoring of a network of submarine strong-motion stations. Field measurements show that the offshore time histories have very low vertical motions

In comparison with an average similar onshore site, especially in short periods. The Boore [3]data shows offshore V/H ratios of the order of 0.2 to 0.3 for short period motion (0.1 to 1.0 s). This is attributed primarily to the effects of the water column.

6.4. Mudline and in profile time histories

A set of seven 3-component earthquake time histories were produced. Data are provided for mudline and at depths of 15 and 30 m below seabed for ELE, ALE and 10,000 year return periods. Plots of the time histories. The data is not included in this paper.

The time histories were developed using the results of the non-linear site response analysis at the site. A set of seven stiff soil records are used for site response. These records are appropriately amplified using the DEEPSOIL nonlinear model to account for site conditions. The resulting mudline accelerograms were post-scaled to match the ELE and ALE year spectra over a period range considered appropriate for structural design. Horizontal components were matched in the range of 1.0 to 3.0 s, while vertical components were scaled to match from 0.5 to 0.75 s.

The methodology was as follows:

- Pre-scale horizontal components (x and y) of recorded (native) stiff soil time histories to target stiff soil PGA;
- Propagate pre-scaled stiff soil horizontal records through soil column using DEEPSOIL model to compute mudline response;
- Scale the horizontal components of motion at mudline to design spectrum over frequency range using FEMA 450 [20];
- Scale stiff soil vertical components directly to mudline vertical target design spectrum under the assumption that vertical motion is not significantly amplified;
- In-profile time histories were computed applying the scaling factors at mudline.

The procedure was repeated for the ELE and ALE ground motion.

6.5. Spectral Matching for Horizontal Components

The mudline time histories were scaled to match the design spectrum following FEMA 450 [20]) recommendations. The input data consist of sets of recorded earthquake ground motion (x, y, and z components). A group of seven 3-component records was selected and scaled such that the average response meets or exceeds the design spectrum over a range of periods near the fundamental period of the structure.

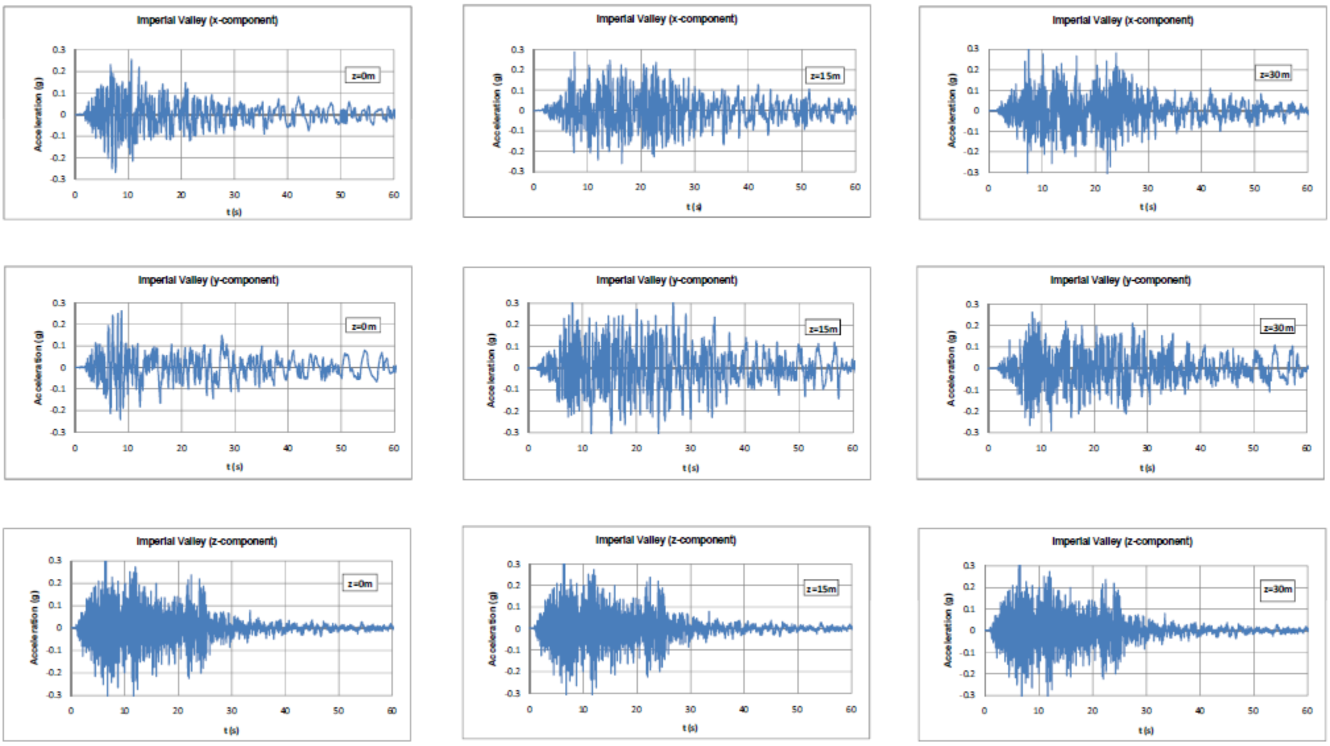

Figure 8: Imperial 10/15/79. Amplified acceleration time-histories- ALE

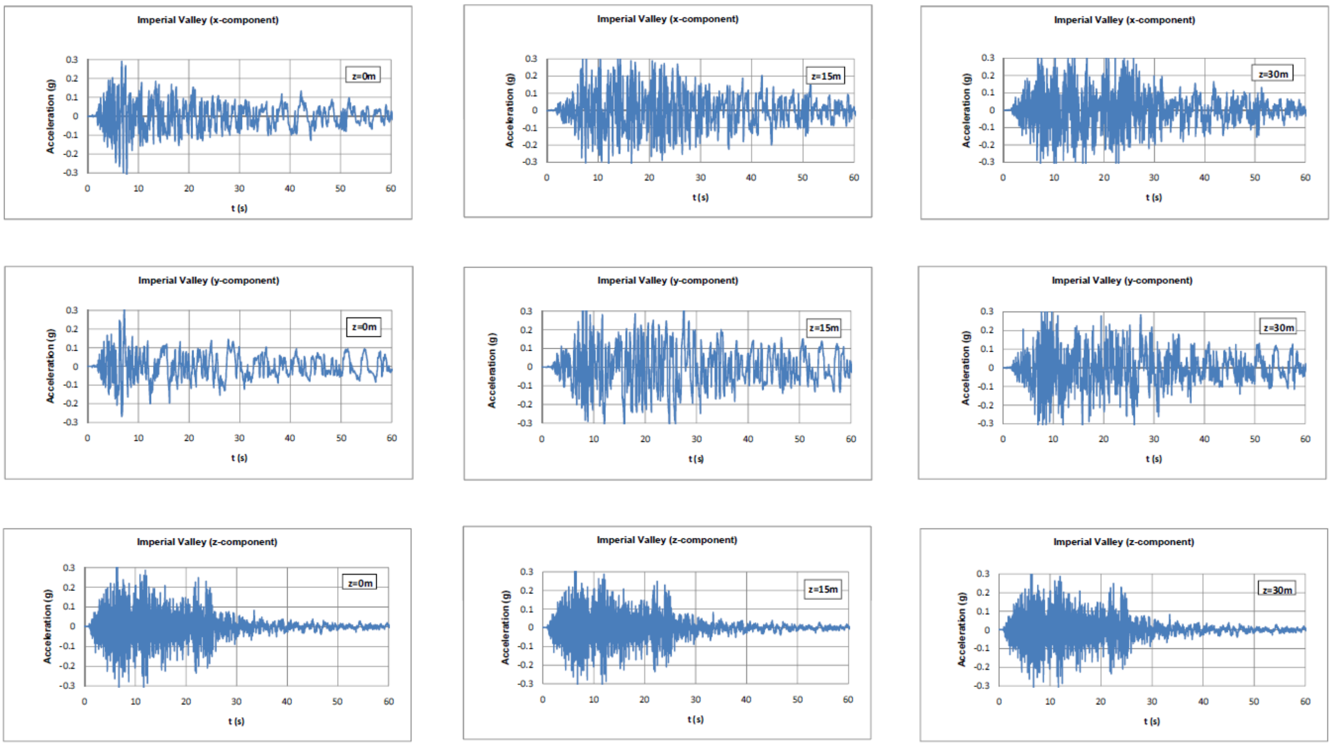

Figure 9: Imperial Valley, 10/15/1979 Amplified Acceleration Time History, 10,000yr Event

For 3D analysis, the horizontal components of each record are combined as a Square Root of Sum of Squares (SRSS) spectrum. The SRSS spectrum is constructed by taking the square root of the sum of the squares of the 5% damped response spectra, at each period (T) for the x and y components of ground motion.

Appropriate scaling factors are then selected for the individual time histories such that the average of the SRSS is not less than 1.3 times the corresponding ordinate of the design response spectrum. FEMA [20] requires that scaling criteria be satisfied for each period between 0.2 and 1.5 times the fundamental period of the structure. This criterion was relaxed somewhat, applying the period ranges discussed in Section 5.5.1. Note that the factor of 1.3 is required to account for the geometric difference between the design spectrum defined for a single direction and the SRSS which is a combination of two orthogonal components. The verification test can be summarized as follows:

$$\frac{\sum_1^n SF_i \cdot SRSS_i(T)}{n} \geq 1.3 Sa_{TD}(T) \qquad (4)$$

Where

SF =scaling factor

$SRSS(T)$ = square root of the sum of squares of x and y of mudline response spectra;

$Sa_{TD}(T)$ = design spectral acceleration

T = periods considered in the range between 0.2 and 1.5 times fundamental period of the structure;

n = number of time histories considered

Two examples are given in Figures 8 and 9. Figure 10 shows the fit of the “Horizontal” scaled time histories.

7. Concluding remarks

This paper uses the ISO 19902 [16] methodology for deriving the site-specific earthquake time-histories using a refined coupled pore pressure generation-site response analysis. The design spectra and time histories are derived using modeling of the site response in effective stress instead of total stress to take into account the effect of soil liquefaction. It was decided that liquefaction is likely to occur in the first ten meters of the profile (which is a sandy layer) for the ALE and 10,000 year return periods. For the ELE event liquefaction development is marginal. The design spectra are given in Table 5. A different approach may lead to spectra which are somewhat lower for the ELE event, and higher for the ALE and 10,000 year return periods. The reduction of spectral acceleration at longer return periods reflects the effects of liquefaction.

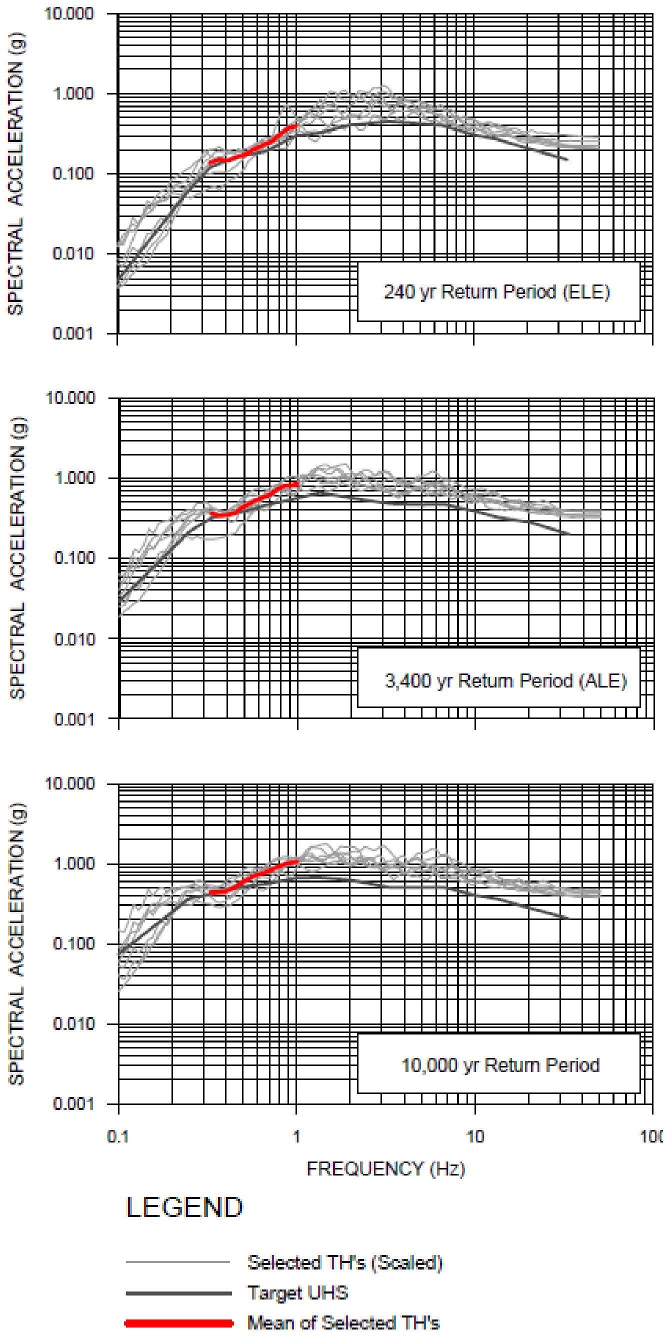

Figure 10: The “Horizontal” scaled time histories showing the fit of scaled time histories

A set of seven 3-component earthquake time histories were calculated for the manifold location. The time histories were obtained through effective stress site response analysis, and thus represent the soft soil conditions at the site in liquefaction conditions. Data are provided for mudline, 15 m, and 30 m penetration, These records have been scaled to match the design spectra in the range of fundamental frequency of the structure following the FEMA [20] procedure.

8. References

1. Banon, H, Cornell, A., Marshal, P.W., Nadim, F., and Younan. H., (2001), *ISO SEISMIC DESIGN GUIDELINES FOR OFFSHORE PLATFORMS,* OMAE2001/S&R-2114, 20th Offshore Mechanics and Arctic Engineering Conference – OMAE 2001, Rio de Janeiro, Brazil, 3rd – 8th June 2001
2. Bommer, J. J., S. Akkar, and O. Kale, (2011), *A Model for Vertical-to-Horizontal Response Spectral Ratios for Europe and the Middle East*, Bulletin of the Seismological Society of America, Vol. 101, No. 4, pp. 1783–1806.
3. Boore, D. M., and Smith, C.E., (1999), *Analysis of Earthquake Recording Obtained from the Seafloor Earthquake Measurement System (SEMS) Instruments Deployed off the coast of Southern California,* Bulletin of the Seismological Society of America, Vol. 89, No. 1, pp. 260–274.
4. Bozorgnia, Y. and Campbell, K.W., (2004), *The Vertical-to-Horizontal Response Spectral Ratio and Tentative Procedures for Developing Simplified V/H and Vertical Design Spectra*, Journal of Earthquake Engineering, Vol. 8, No. 2, pp. 175-207.
5. Cornell CA, Vanmarcke E.H., (1969), *The major influences on seismic risk* Proceedings of the 4th World Conference on Earthquake Engineering, Santiago, Chile.
6. Cornell CA., (1968), *Engineering seismic risk analysis,* Bulletin of the Seismological Society of America 58(5):1583–1606.
7. Cornell, CA, (1996), *Reliability-based earthquake resistant design; the future*, paper, No. 2166, 11th World Conference on Earthquake Engineering pp 1-11.
8. Campbell, K. W., and Y. Bozorgnia, (2003), *Updated near-source ground motion (attenuation) relations for the horizontal and vertical components of peak ground acceleration and acceleration response spectra,* Bulletin of the Seismological Society of America, Vol. 93, pp. 314-331.
9. Darendeli, M. B., (2001), *Development of a New Family of Normalized Modulus Reduction and Material Damping Curves*, Department of Civil Engineering, the University of Texas at Austin, Austin.
10. Gülerce, Z., and N. A. Abrahamson, (2011), *Site-Specific Design Spectra for Vertical Ground Motion*, Earthquake Spectra, Vol. 27, No. 4, pp. 1023–1047
11. Hashash, Y .M. A., D. R. Groholski, C. A. Phillips and D. Park, (2009), *DEEPSOIL V3.7beta, User Manual and Tutorial*, 88 pp.
12. Hashash, Y. M. A. and D. Park, (2001), *Non-linear One-Dimensional Seismic Ground Motion Propagation in the Mississippi Embayment*, Engineering Geology, Vol. 62, No. 1-3, pp. 185-206.
13. Idriss, I.M., Dobry R., and R.D. Singh, (1978), *Nonlinear Behaviour of Soft Clays During Cyclic Loading*, Journal of Geotechnical Engineering Div., ASCE, Vol. 104, No. 12, pp. 1427-1447.
14. International Standard ISO 19901-2, (2004), Petroleum and Natural Gas Industries – Specific Requirements for Offshore Structures – *Part 2: Seismic Design Procedures and Criteria, November*.
15. International Organization for Standardization: ISO 19901-4, (2002), Petroleum and Natural Gas Industries – Specific Requirements for Offshore Structures – Part 4: Geotechnical and Foundation Design Considerations.
16. International Organization for Standardization: "ISO 19902:2007(E) Petroleum and Natural Gas Industries – Fixed Steel Offshore Structures," 2007.
17. Ishibashi, I., and X. Zhang, (1993), *Unified Dynamic Shear Moduli and Damping Ratios of Sand and Clay,* Soils and Foundations, Vol. 33, No. 1, pp. 182-191.
18. Konder, R. L. and J. S. Zelasko, (1963), *A Hyperbolic Stress-Strain Formulation of Sands*, Proceedings of the 2nd Pan American Conference on Soil Mechanics and Foundation Engineering, Sao Paulo, Brazil, pp. 289-324.
19. Kramer, S. L., (1996), *Geotechnical Earthquake Engineering*, Prentice Hall, Inc., Upper Saddle River, NJ.
20. NEHRP (2005), *Recommended Provisions for Seismic Regulations for New Building Sand Other Structures (FEMA 450),* Prepared for Federal Emergency Management Agency, National Institute of Building Sciences, Washington, D.C. 4, pp. 1023–1047.
21. Masing G., (1926), *Eingenspannungen and verfertigung beim messing*, Second International Congress on Applied Mechanism, Zurich, Switzerland, pp. 332-335.
22. Matasovic, N. O. and Vucetic, M., (1993), *Cyclic Characterization of Liquefiable Sands,* Journal of Geotechnical and Geoenvironmental Engineering, ASCE, Vol. 119, No. 11, pp. 353-69.
23. Matasovic, N. O. and M. Vucetic, (1995), *Generalized Cyclic-Degradation-Pore-Pressure Generation Model for Clays*, Journal of Geotechnical Engineering, Vol. 121, No. 1, pp. 33-42.
24. Park, D., and Hashash, Y.M.A., (2004), *Soil Damping Formulation in Nonlinear Time*

Domain Site Response Analysis, Journal of Earthquake Engineering, Vol. 8, No. 2, pp. 249-274.

25. Phillips, C., and Hashash, Y.M.A., (2009), *Damping Formulation for Non-Linear 1D Site Response Analyses,* Soil Dynamics and Earthquake Engineering, Vol. 29, No. 7, pp 1143-1158.
26. Sadigh, K., Chang, C.-Y., Egan, J. A., Makdisi, F., and Youngs, R. R., (1997), *Attenuation relationships for shallow crustal earthquakes based on California strong motion data*, Seismol. Res. Lett. 68 1, 180–189.
27. Seed, H. B., Idriss, I.M., Makdisi, F., and Banerjee, N., (1975), *Representation of irregular stress time histories by equivalent uniform stress series in liquefaction analyses*, EERC 75-29, Earthquake Engineering Research Center, University of California; Berkeley.
28. Seed, H. B., Wong, R. T., Idriss, I. M., and K. Tokimatsu, (1986), *Moduli and Damping Factors for Dynamic Analyses of Cohesionless Soils,* Journal of Geotechnical Engineering, ASCE, Vol. 112, No. 11, pp. 1016-1032
29. Scawthorn, Ch, and (Editor), Wai-Fah Chen, W.F., (2002) *Earthquake Engineering Handbook* CRC Press; 1 edition.
30. Vucetic, M. and Dobry, R., (1991), “Effect of Soil Plasticity on Cyclic Response”, Journal of Geotechnical Engineering, ASCE, Vol. 117, No.1, pp. 89-107.
31. Wells, D.L., Coppersmith, K.J, (1994), *New Empirical relationship among magnitude, rupture length, rupture width, rupture area, and surface displacement,* Bulletin of the seismological society of America, Vol, 84, No. 4 pp 974-1002, 1994.
32. Yasseri, S, (2020), *Seismic Design of Subsea Jumper per ISO: Part I- Preliminaries,* IJCOE Vol.4/No. 1/Spring 2020 (31-43)
33. Yasseri, S. (2020), Seismic Design of Subsea Spool per ISO: Part III- Analysis & Design, IJCOE Vol.4/No. 3/Autumn 2020

Table of abbreviations

Abbreviation/ Acronym	Description
BSF	below seafloor
COG	Centre Of Gravity
CPT	Cone Penetration Test;
DLE	Ductility Level Earthquake
FE	Finite Element
FEMA	Federal Emergency Management Agency
FTA	Flowline Termination Assembly
G	Shear modulus
Gmax	Shear modulus at low strain
HP	High Pressure
NA	Not Applicable
NEHRP	National Earthquake Hazard Reduction Program
PEER	Pacific Earthquake Engineering Research Centre
PGA	Peak Ground Acceleration
PSHA	Probabilistic Seismic Hazard Assessment
RC	Resonant Column
Sa	Spectral Acceleration
SD	Slump Deposits
Su	Undrained shear strength
UHS	Uniform Hazard Spectra
Vs	Shear wave velocity

INTERNATIONAL JOURNAL OF
COASTAL & OFFSHORE ENGINEERING

IJCOE Vol.5/No. 2/Summer 2020 (15-22)

Numerical study of the effect of Base Isolated (neoprene) on the dynamic response of the installed module on the FPSO deck

Mahdi Saleh[1], Rouhollah AmirAbadi[2*], Mahdi Sharifi[3]

[1] *PhD Student, University of Qom; m.saleh@stu.qom.ac.ir*
[2] *Assistant Professor, University of Qom; r.amirabadi@qom.ac.ir*
[3] *Assistant Professor, University of Qom; m.sharifi@qom.ac.ir*

ARTICLE INFO

Article History:
Received: 02 Nov. 2020
Accepted: 19 Dec. 2020

Keywords:
Floating Platform
Dynamic Analysis
FPSO
Time History Analysis
Neoprene

ABSTRACT

Significant advantages of FPSO in the ability to transfer and extract from offshore wells have led to their widespread applications. Kind of different modules is installed on the top of these platforms, where one of the major engineering concerns is choosing the location of these modules on the FPSO platform deck in order to reduce the effects of environmental forces. Typically, these modules are analyzed and designed based on the maximum linear acceleration extracted from the ship's spectral analysis, using a quasi-static method. The main purpose of this research is the analytical study of these modules response under dynamic excitation due to the wave effect. This research has been done in two parts. First, the dynamic response of different parts of the ship's deck has been analyzed under the effect of wave force and proper location for these modules is recommended. For this purpose, first with modeling and analysis performed in MAXSURF software, the ship's dynamic responses at different points of the deck have been calculated. Then these modules have been analyzed against the deck response considering base isolation at the module bases in the second part. The obtained response has been applied to two modules as a case study in Sap2000 software. The result shows that base shear and displacement have a verity response in the function of base isolation stiffness. Due to the extension of the ship's deck and the serious differences in the acceleration spectrum at different locations of the deck, in order to select the optimal stiffness, the locations of the desired module must also be considered.

1. Introduction

In addition to the conventional uses of maritime transportations, vessels are also intended to use for extracting oil and gas from offshore wells. These floating platforms are similar to onshore oil refineries, with different equipment and modules located in different parts of the ship's deck. The design of these modules is one of the interest topics for researchers due to the type of operation loads and environmental effects. In general, naval vessels are commonly exposed to the forces of wind, waves, and currents. So, in addition to the usual loads that are applied, also in analyses and design, these modules shall tolerate the forces caused by environmental loads. Generally In ships and similar facilities, , due to the width of the deck and geometric shape of the hull, the modules installed in different locations of the deck and therefore these modules are faced with different dynamic responses from the ship movement under waves effect. The structural design and analysis of the installed modules on the deck of ships are mainly consider with using a maximum of linear acceleration resulting from the spectral analysis wave applied to the hull of the ship. In the quasi-static analysis, the normal practice of design is only considering the maximum acceleration to the structure, therefore, complete details of the structure response are not obtained. The main purpose of this research is analytical study of these modules response under dynamic excitation due to wave effect. This research has been done in two parts. First, the dynamic response of different parts of the ship's deck has been analyzed under the effect of wave force and proper location for these modules is recommended. Then these modules have been analyzed against the deck response considering base isolation at the module bases at the second part.

In this study, the dynamic response of a module on the deck of an FPSO platform is assumed to be based on that fact the ship is stationary as the worst case when the wave hits the hull. In this research, first, the dynamic response of different locations of the ship's deck under the effect of wave force is investigated and appropriate suggestions are presented. Then in the second part, the numerical study of dynamic response of the base isolated installed module (neoprene provided at its supports) on the designated location on the deck is studied.

2. Introducing the FPSO

Usually, tankers and containers ships have a flat deck which are not equipped with structures on top of the deck, but in FPSO platforms, depending on their operation purpose, there are various installed equipment, and structures on top of deck.

In summary, each FPSO has the following parts:

1. Space related to anchoring equipment
2. Topside Deck
3. Main Deck
4. Accommodation
5. Powerhouse
6. Storage Tankers
7. Cargo Unloading Area

Topside equipment are generally divided into two categories according to their performance. One part of equipment are hydrocarbons container and the other part is service equipment.

The main area of hydrocarbon includes:

- Flares
- Compression equipment
- Separation equipment

The main area related to service equipment includes:

- Industrial equipment
- Electrical and energy power equipment
- Structures and modules on the Topside

According to safety rules, it is better to positions of the hydrocarbon equipment area at the farther distance from the accommodation, and service equipment will be placed between this area and the accommodation. In general, on the deck of these platforms are different installed modules including power generators, HP / LP separators, gas purification, and compression modules which are located at the other side of the ship water injection, dewatering, accommodation and etc. are installed. In addition, the design should include a number of safety facilities such as lifeboats, temporary shelters, escape routes, and fire water pumps. The general view of the equipment locations is shown in Figure 1. In the hydrocarbon process area, separate modules are design. The supports of the modules are installed on short columns mounted on the deck of the ship. This method allows the modules to be fabricated on shore and installed on the deck of the ship as a complete modules.

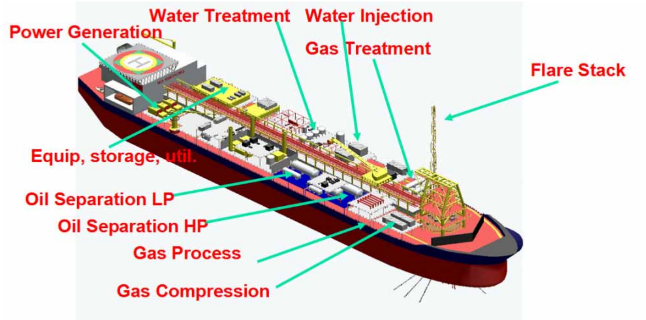

Figure 1 - Example of equipment installed on the main deck of the FPSO

The dimensions of different modules are estimated and selected according to various parameters, including the following:

- The size of the largest piece of equipment, for example separators
- Predicting the maximum load capacity of the crane in that area (in terms of weight and height)
- Predict the largest dimensions required for commuting areas such as the interior doors of the accommodation

Surface of the hydrocarbon container is coated to protect area against the penetration of these materials into the deck and corrosion.

The presence of different modules on the deck of this type of ship shape platform has caused sensitivity to the acceleration and the dynamic response of these modules to the forces. In this study, this response has been investigated in two different type of module support.

3. Literature review

Vessels and offshore structures are exposed to irregular waves at the sea conditions. Wave effect on these structures are studied in the science of random vibrations that convert each irregular wave into a set of several regular waves using the Fourier transform (figure 2). These calculations were discussed by Journey in detail at the field of marine structures [1].

Journey used these calculations to convert time domain into frequency domain. The Fourier transform is used to convert an irregular wave to a set of regular waves and finally to calculate the wave spectrum.

Kamphuis performed extensive statistical calculations in the field of sea waves and used the wave spectra obtained from Fourier transforms to derive the main wave parameters [2].

This issue was previously raised in 2007 by Holthuijsen et al. In the field of marine engineering [3].

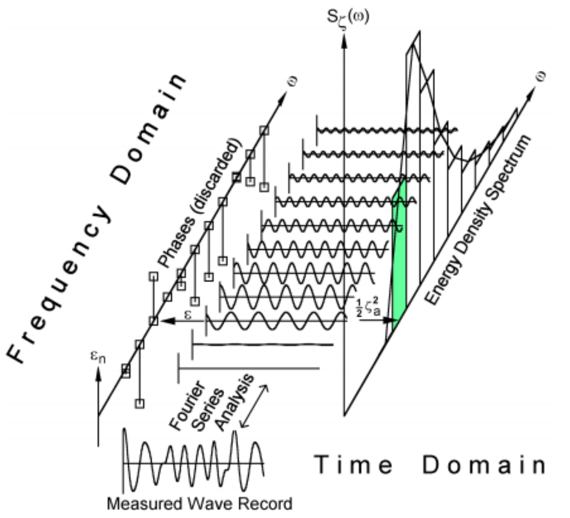

Figure 2 - Convert an irregular wave to a set of regular waves

Equation (1) is one of the most important equations in the field of random vibrations. This relationship was presented by Newland in 1993 and 2012 [4].

(1)

$$S_y(\omega) = |H(\omega)|^2 \, S_x(\omega)$$

In this equation $S_y(\omega)$ is response spectral density, $|H(\omega)|$ is system spectral density and $S_x(\omega)$ is excitation spectral density.

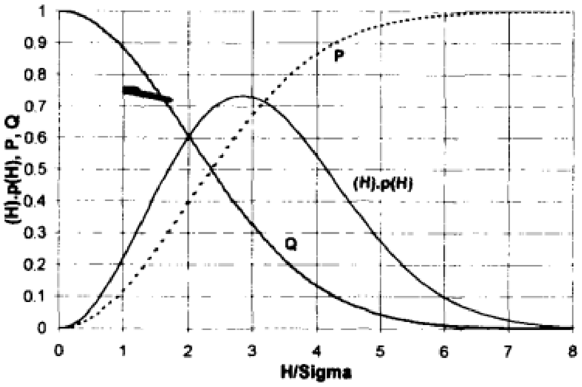

Figure 3 - Riley wave height distribution

It should be noted that in marine engineering field, the response amplitude operator (RAO) is used instead of the frequency response function. RAO of a degree of freedom is the response of that degree of freedom to the force of a wave with a unit height. Is that be shown as below formula:

$$S_y(\omega) = |RAO|^2 \, S_x(\omega) \qquad (2)$$

Up to this stage of studies, the convert from the time domain to the frequency domain was briefly discussed. Sometimes in calculations, it is necessary to convert frequency domain to time series function. In other words, using the inverse Fourier from the frequency domain to the time domain for time history analysis. This topic was thoroughly discussed in the field of random vibrations in 1999 [5] and then 2001 [6] by Frigaard.

One of the challenges in the field of oil and gas extraction is designed the economical equipment for extraction from shallow and deep water. Lapidaire and et al are the first researcher in these field in the theory of floating platforms in deep water. In 1996, they studied the ship-shaped floating platforms and the effect of waves on them base on their extensive experience in the field of design, installation in fixed platforms [7]. Han and colleagues (2002) examined a specific type of FPSO platform for the extraction and storage of liquefied natural gas. This type of platform is called FSRU. They stated that with the expansion of natural gas demand in many countries, the extraction of these resources from deep water is important and after extensive studies, FSRU as a suitable scientific and economical solution to this challenge [8]. Now, considering popularity of using and designing FPSO platforms was increasing, this issue was faced with the challenge of a lack of sufficient information and data. In this condition, Wang and et al show the lack of appropriate data available for the design of these platforms. In 2003, they focused on providing data from commercial tankers that could be used to design FPSO platforms [9]. As reported by Chakrabarti (2005), in Chapters 7 and 10 of the "Marine Structures Engineering Handbook", reviewed the design of offshore structures as well as the equipment on the deck of these rigs, and finally provided useful information in this area [10]. The issue of forces excreted the hull of the ship is still under debate, with Buchner and et al studied the effects of strong waves in deep water on floating structures (2007). They focused on the response of the structure to the incoming waves by numerical methods [11]. Molland, (2008) in Section 9 of the Marine Engineering Reference Book, discusses the design, construction, and operation of the ship [12]. Henriksen et al (2008). Carefully investigate the structures on the deck of the FPSO platforms under the loads caused by the deformation of the main hull beams, the pressure from the existing tankers, and the inertial force of the structures on the deck [13]. Luo and his colleagues then investigated the FPSO for use in deep water (2014). They reviewed deck structures, hulls, floating systems, anchoring systems, risers, and design concepts in the South China Sea [14]. The expansion of the use of FPSO has led to broader and more complex discussions tailored to the climatic conditions of each region. Watson and his team investigated the effect of the collision of ice cubes (2019) [15] And Davis and colleagues in 2019 discussed the issue of explosion risk analysis in design [16]. In this regard, the issue of comparing the stability of different types of floating platforms in 2019 was on the agenda of Rivera and his team [17]. Due to the importance of the impact of environmental forces in the design of marine structures, this issue has received much attention today. In this regard, Dezvareh intends to examine the effect of wind turbulence on the aero-hydrodynamic behaviour of offshore wind turbines with a monopile platform [18].

4. Method Statement

In these study, analytical Modeling has been done in several stages with using three commercial software. MAXSURF software version 8 is used for modeler and motions module. Then spectral outputs are converted to time history using SeismoArtif software version 2020 and finally, time history analysis is performed on the desired module using SAP software version 14.2. The details of each model are discussed separately below.

4.1. Modeling in MAXSURF

The ship with a length of 205 meters, a width of 37 meters, a depth of 26.55 meters, and a draft of 10.55 meters is considered in these studies. The basis of this modeling is the use of standard JONSWAP spectrum and waves with a height of 4m and 11m. Total of 6 points on the deck surface of this ship shape platform have been considered for selecting the best locations of module. The location of these points on the deck of the ship have shown in Figure 4.

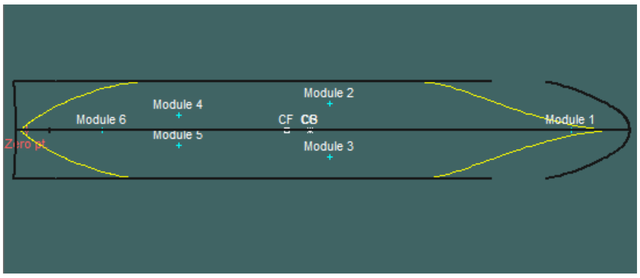

Figure 4 – Locations of the studied position

It is assumed that the ship is stationary at the moment of the waves hitting the hull. Also, the wave hitting angles are assumed to be 0 and 90 degrees. It should be noted that the presented results are related to a wave with a height of 4 meters. Initially, the RAO of the three degrees of freedom of the roll, pitch and heave at the center of gravity of the ship to due to waves with angles of 0 and 90 degrees is analyzed. Figure 5 shows the results of the ship's response to a wave with a zero-degree angle of impact.

As shown in Figure 5, according to the angle of impact of the wave on the ship, pitch and then heave degree of freedom (DOF) will have the greatest effect on the response of the ship and the response of the degree of freedom of the roll is near to zero. In the second step, the ship's response is studied under the effect of a wave with an angle of 90 degrees. As shown in Figure 6, the RAO of the roll DOF is far greater than the response values of the pitch and heave.

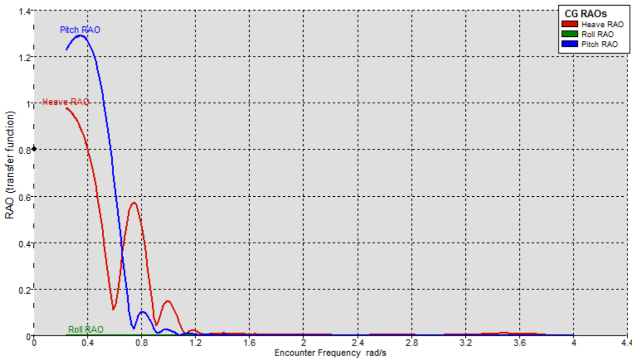

Figure 5 – RAO of the CG disp, wave impact angle: zero degree

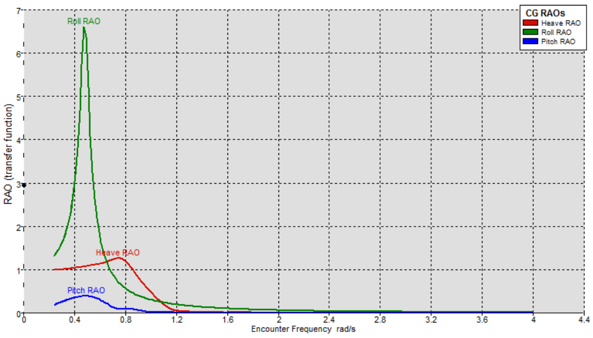

Figure 6 – RAO of the CG disp , wave impact angle: 90 degree

In the next step, the RAO is extract at the desired points on the deck of the ship. based on this study, it was found that in general, the response of the module in points 1and 6, 2 and 4, as well as 3 and 5 are similar to each other in pairs. Due to this similarity, the location 1 and 2 have been investigated. The point of 1 and 6 is located in the vessel centerline with zero distance in the transverse direction and far distance in longitudinal direction. So, it is anticipated to have maximum vertical displacement response in wave hitting in zero angles as obtained in results. Figure 7 clearly confirms this.

Wave is hitting in zero angles cause maximum vertical displacement in vessels and so the maximum displacement response of location 2 is much less than location 1 because of this point is closer than ship center of mass.

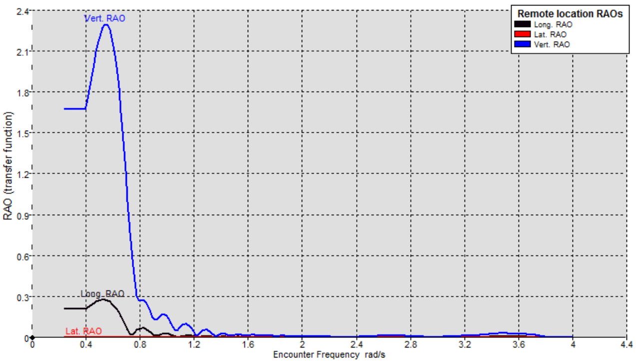

Figure 7 – RAO of the module 1 disp , wave impact angle: 0 degree

The response diagram of this position is in accordance with Figure 8.

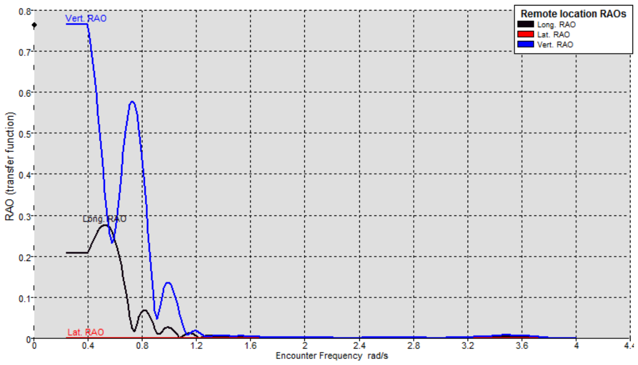

Figure 8 – RAO of the module 2 disp, wave impact angle: 0 degree

Then, the response of the module in location 1 due to the impact of the wave with an angle of 90 degrees is investigated. In this case, in addition to the response in the direction of vertical displacement, the response in the transverse direction is also significant according to Figure 9, but the values of longitudinal displacements are close to zero.

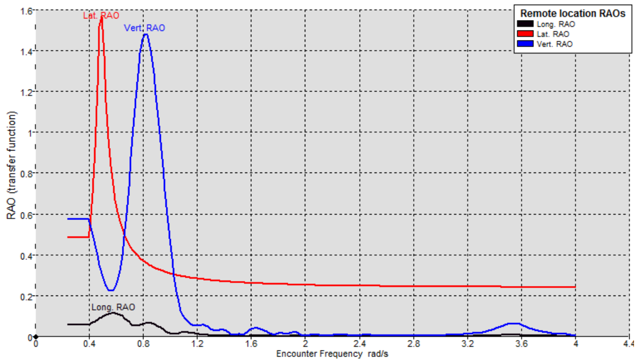

Figure 9 – RAO of the module 1 disp, wave impact angle: 90 degree

In position 2, due to the impact of this wave, the amplitude of the transverse displacement response is almost unchanged compared to position 1, but in vertical displacement, it shows a response nearly twice as large as position 1.

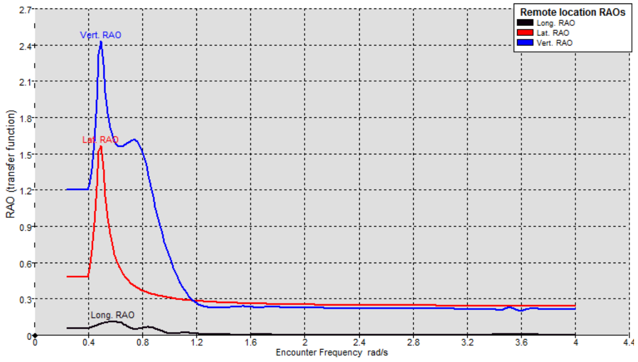

Figure 10 – RAO of the module 2 disp, wave impact angle: 90 degree

Because of the extreme impact of transverse displacement on the response spectrum, in this study location 2 has been selected for structural response study. The response acceleration spectrum in this location is presented in both X and Y directions according to Figures 11 and 12, respectively.

4.2. Generating Time Series

Response accelerations spectra result from MAXSURF software is presented in Figures 11 and 12. These responses are converted into time series function with using SeismoArtif software.

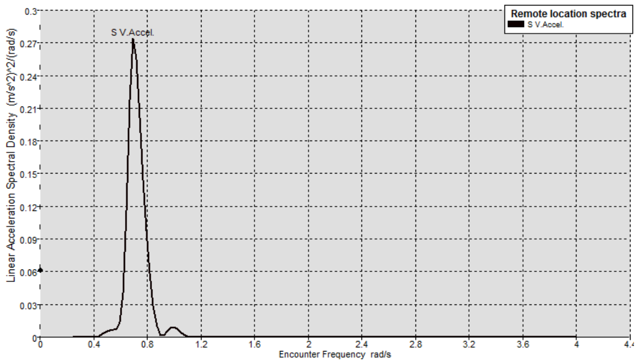

Figure 11 – The acceleration spectrum in position 2, X Direction (wave height 4 m)

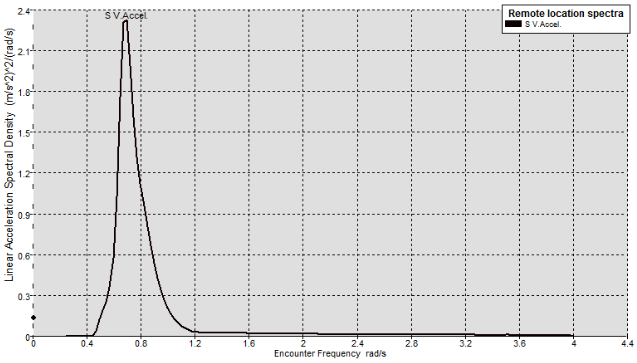

Figure 12 – The acceleration spectrum in position 2, Y Direction (wave height 4 m)

Time history records generated in both X and Y directions are shown in Figures 13 and 14, respectively.

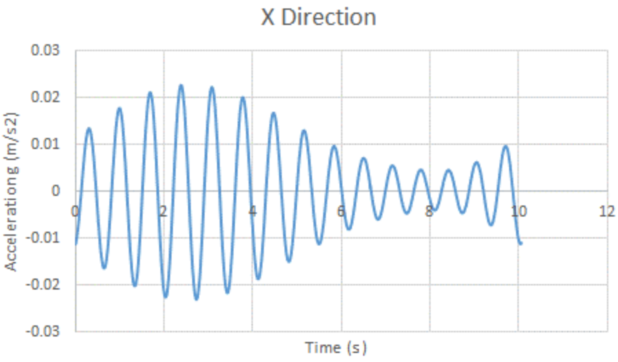

Figure 13 – Generated Time History – X Direction

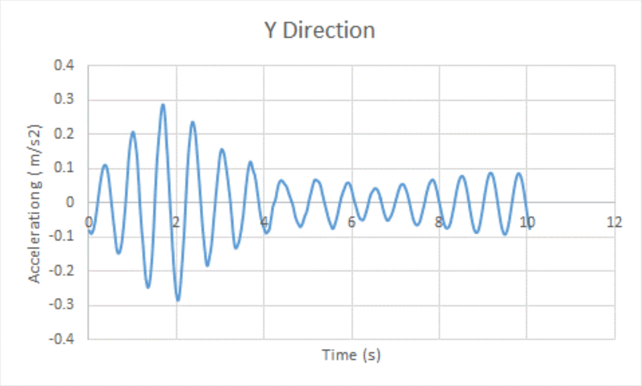

Figure 14 – Generated Time History – Y Direction

As seen in the figures that the response of the module in the Y direction is much more critical and nearly 10 times higher than in the X-direction. This can also be predicted from the ship response amplitude operator in Figures 8 and 10.

In the next step, the time history obtained on the installed modules is studied.

4.3. Modeling in SAP

The studied module that modeled in SAP software according to Figure 15 has 4 supports at a distance of 6 meters from each other and with an overall height of 7.55 meters.

This module is a sample of a module installed on a FPSO deck and is considered as a real module.

Figure 16 shows the general assembly and installed equipment's on selected module.

Two separate models of this module have been prepared in SAP software V.14.2, all modeling parameters in both models are the same except the support constraints.

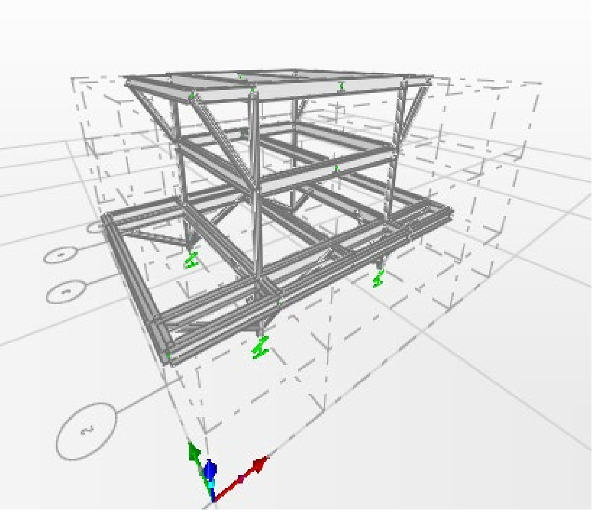

Figure 15 – Extruded view in SAP

In the first model, the fixed support is used according to Figure 17. In the second model, neoprene is used as support constraints according to Figure 18.

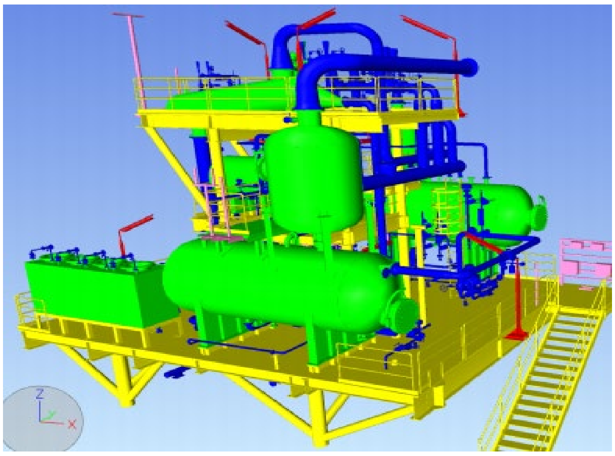

Figure 16 – Equipment installed on the module

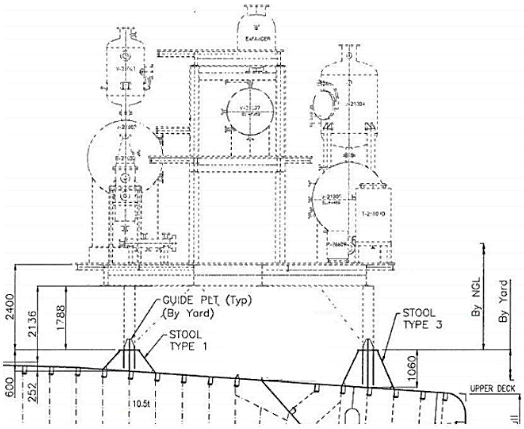

Figure 17– the connection of the fixed support to the ship deck

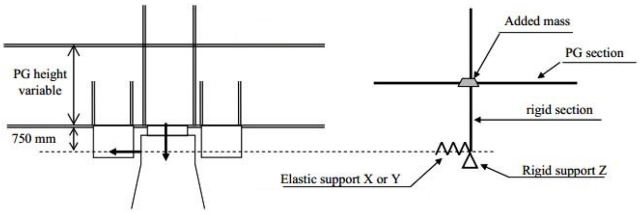

Figure 18– sample of the support connection with neoprene

5. Results and Discussion

In this modeling, different stiffness has been theoretically assumed for base isolations. Stiffnesses are designed to cover wide range intervals of the natural period of the structure. The natural period of the fixed module is about 0.4. The stiffness of base isolations is selected in such a way that include a module natural period between 0.4 to 4 seconds. In similar conditions, the module was analyzed due to the impact of 11-meter wave height on the ship, and for a more detailed study, this case done with more stiffness conditions so a natural period of module up to 5.7 seconds. Finally, the base shear, displacement, and moment created by the wave impaction are investigated. Figures 19, 20, and 21 show the outputs of the base shear, displacement, and moment created in the support member, respectively.

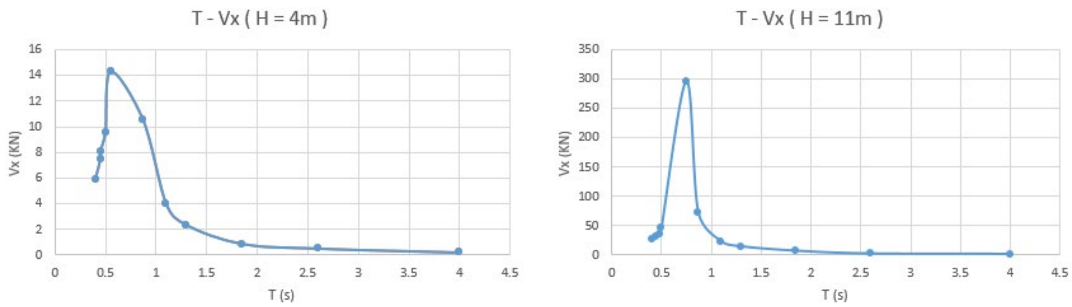

a) Base shear in X direction

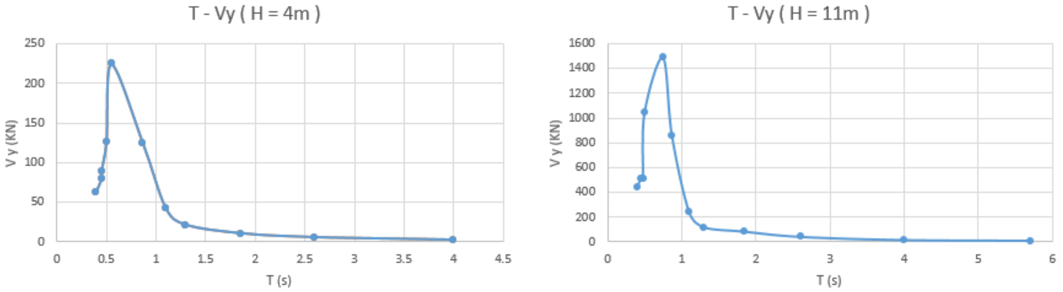

b) Base shear in Y direction

Figure 19 – Base shear on the module

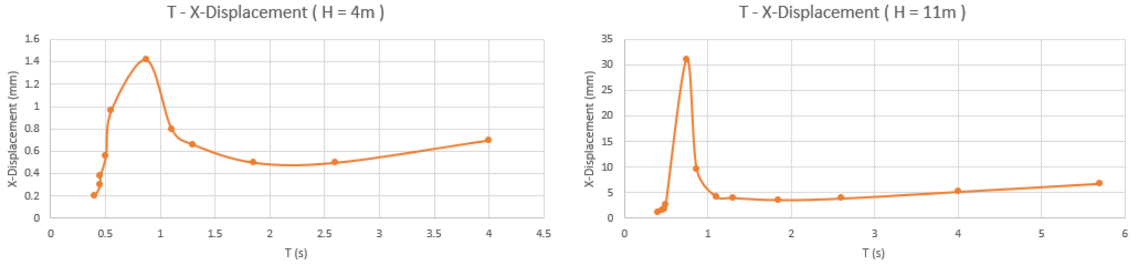

a) Displacement in X direction

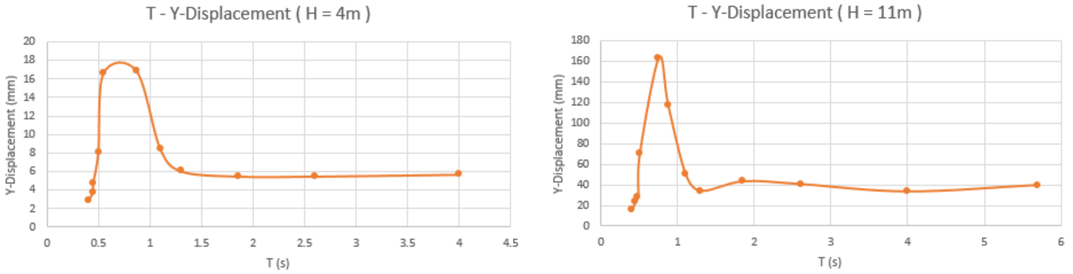

b) Displacement in Y direction

Figure 20 – Displacement on the module

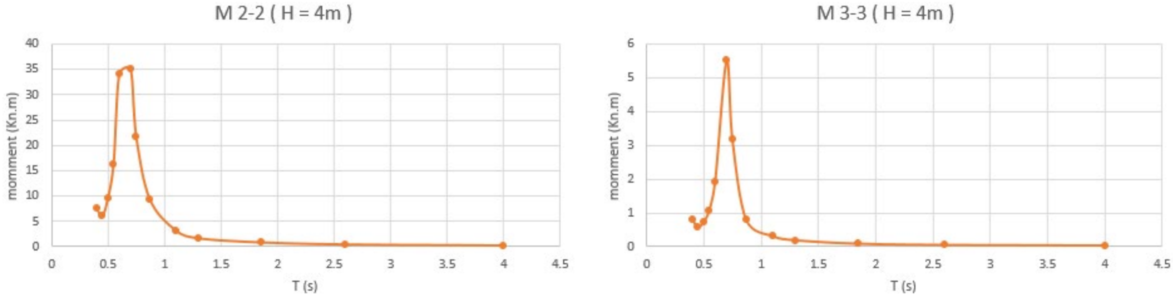

Figure 21 – the moment created in the support member

As shown in Figures 13 and 14, due to the narrow band of the acceleration response spectrum, the time history record created is very close to the harmonic condition. So, the excitation period is approximately 0.7 seconds. Clearly in all the results that when the natural period of the module approaches the excitation period, the module experiences the resonance phenomenon and shows maximum high responses. In this regard, one of the main principles of choosing the stiffness of neoprene is to pay attention to the excitation period to avoiding resonance. As can be seen in Figure 19, outside the resonance range, the base shear always decreases as the stiffness of the neoprene decreases.

According to Figure 20, it can be noted that the use of neoprene does not have a positive effect on improving the displacement of the module.

In Figure 21, reducing the stiffness of neoprene outside the resonance range always lead to reduce the moment created in the support elements.

5. Conclusions

In this study, Analytical investigation has been performed in two sections including determining the ship deck response against wave hitting and structural dynamic analysis of the install module on deck. With regard to obtaining the result and apply assumption following result can be inferred. The section one shows:

- Wave hitting in the most cases, cause a maximum response in the ship location that is located in the far distance from the ship center of mass.
- A formation result shows that it is better to install modules closer to the center of mass. This result also maybe considers for rescue helipad location.

Results in section two shows:

- Install modules excited with harmonic function due to wave hitting.
- With regard to harmonic excitation in selecting base isolation more attention shall be applied in such a way that module frequency shift from harmonic excitation frequency.
- Generally base isolation cause reducing base reaction (shear and moment) of installed modules.
- If install modules are sensitive to displacement more caution shall be applied in base isolation selection.
- With regard to variety of response of deck under wave hitting in difference location
- base isolation stiffness is important parameter in structural design and response resonance.

6. References

1- Journee, J. M., & Massie, W. (2001). *Introduction in offshore hydromechanics* (OT3600). TUDelft, Faculty of Marine Technology, Ship Hydromechanics Laboratory, Report No. 1267-K, Lecture Notes.

2- Kamphuis, J. W. (2010). *Introduction to coastal engineering and management* (Vol. 30). World Scientific.

3- Holthuijsen, L. H. (2010). *Waves in oceanic and coastal waters*. Cambridge university press.

4-Newland, D. E. (2012). *An introduction to random vibrations, spectral & wavelet analysis*. Courier Corporation.

5- Liu, Z. and P. Frigaard (1999). *Generation and Analysis of Random Waves*, Aalborg Universitet.

6-Liu, Z., & Frigaard, P. (2001). *Generation and analysis of random waves, cursus*. Aalborg University.

7-Lapidaire, P. J. M., & Leeuw, P. J. (1996, January). *The effect of ship motions on FPSO topsides design*. In Offshore Technology Conference. Offshore Technology Conference.

8- Han, H., Lee, J. H., & Kim, Y. S. (2002, January). *Design development of FSRU from LNG carrier and FPSO construction experiences*. In Offshore Technology Conference. Offshore Technology Conference.

9- Wang, G., & Spong, R. (2003, January). *Experience based data for FPSO's structural design*. In Offshore Technology Conference. Offshore Technology Conference.

10- Chakrabarti, S., Halkyard, J., & Capanoglu, C. (2005). *Historical development of offshore structures*. In Handbook of offshore engineering Elsevier.

11- Buchner, B., & Bunnik, T. (2007, January 1). *Extreme Wave Effects on Deepwater Floating Structures*. Offshore Technology Conference.

12-Molland, A.F. (2008), *Ship design, construction and operation.*

13- Henriksen, L.O., Wang, X., & Liu, D.J. (2008). *Structural Design and Analysis of FPSO Topside Module Supports.*

14- Su, Z., Luo, Y., Qi, X., & Xie, Y. (2014, March 25*). FPSOS for Deepwater Applications*. Offshore Technology Conference.

15- Sayed, M., Watson, D., Islam, S., & Wright, B. (2019, July 15). *The Influence of Floe Size and Ice Concentration on Ice Force Levels for an FPSO in Pack Ice*. International Society of Offshore and Polar Engineers.

16-Davis, S., Marsegan, C., & Botwinick, D. (2019, April). *Inherent Safety-How to Utilize Explosion Hazard Analyses as an Early Tool to Improve FPSO and FLNG Design*. In 2019 Spring Meeting and 15th Global Congress on Process Safety. AIChE

17- Rivera, L. A., Neves, M. A., Cruz, R. E., & Paulo de Tarso, T. E. (2019). *A study on unstable motions of a tension leg platform in close proximity to a large FPSO*. In Contemporary Ideas on Ship Stability (pp. 307-321). Springer, Cham.

18- Dezvareh, Reza. "*Evaluation of turbulence on the dynamics of monopile offshore wind turbine under the wave and wind excitations*." Journal of Applied and Computational Mechanics5, no. 4 (2019): 704-716.

INTERNATIONAL JOURNAL OF
COASTAL & OFFSHORE ENGINEERING

IJCOE Vol.5/No. 2/Summer 2020 (23-40)

Available online at: www. Ijcoe.org

Application of tuned liquid column damper for motion reduction of semisubmersible platforms

Hamidreza Feizian[1], **Mehdi Shafieefar**[2*], **Roozbeh Panahi**[3]

[1]PhD Student, Faculty of Civil and Environmental Engineering, Tarbiat Modares University; h.feizian@modares.ac.ir
[2]Professor, Faculty of Civil and Environmental Engineering, Tarbiat Modares University; shafiee @modares.ac.ir
[2]Assistant Professor, Faculty of Civil and Environmental Engineering, Tarbiat Modares University; rpanahi @modares.ac.ir

ARTICLE INFO

Article History:
Received: 27 May. 2020
Accepted: 21 Dec. 2020

Keywords:
Tuned liquid column damper;
Semisubmersible platform;
Low-frequency motion;
Irregular waves

ABSTRACT

Incorporation of a tuned liquid column damper (TLCD) into a semisubmersible drilling platform is numerically investigated in this paper. First, a governing equation for liquid fluctuation in the TLCD is derived for the planar motion of the TLCD in conjunction with the motion of the platform. Then, the real-time response of the platform under irregular waves is analyzed using radiation/diffraction theory in which TLCD loading is exerted on the platform at each time-step. This facilitates capture of the difference-frequency and sum frequency second order wave forces and the low-frequency motion of the platform. The results show that the effect of the rotational motion of the platform on the TLCD is significant and the TLCD has a reciprocal effect on this rotational motion of the platform. It is shown that the TLCD decreases the low-frequency motion of the platform and has no considerable effect on the wave-frequency motion. Also, the sensitivity of the platform motion to the main specifications of the TLCD is assessed by a parametric study.

1. Introduction

Offshore floating platforms are employed worldwide for various deep-water applications. It is essential to control the motion and vibration of such platforms in order to maintain safety and comfort of personals. Thus, researchers have implemented different approaches to reduce motion of floating platforms. Structural shape optimization has been investigated by Clauss and Birk [1], Adjami and Shafieefar [2], Lee and Lim [3], Muskulus and Schafhirt [4] and Hall et al. [5]. However, this approach is not applicable to the existing platforms because it remains in the conceptual design stage.

Mooring optimization is another effective approach for motion reduction of existing platforms. Shafieefar and Rezvani [6] optimized the mooring pattern, length and tension for a ship-shaped floating platform using a genetic algorithm (GA). A GA was also used by Mirzaei [7] to optimize the mooring pattern of a crane barge. Ren et al. [8] studied the effect of additional mooring chains on the motion of a floating wind turbine with a tension leg platform. Brommundt et al. [9] worked on floating wind turbines using a simplex algorithm to determine the optimum line configuration for a semisubmersible platform.

Passive methods such as a tuned mass damper (TMD) and tuned liquid column damper (TLCD) have been increasingly considered for offshore fixed and floating platforms [10]. The TLCD is the most attractive of these approaches because of its low cost, ease of handling, and limited maintenance requirements [11,12]. TLCDs have been used for many years for fixed structures on land, such as for buildings with short periods [13–17]. It should be noted that the hydrodynamics of moored floating structures with very long periods differ from the dynamics of fixed structures on land.

A TLCD is a U-shaped tube containing a liquid (commonly water) which has an orifice that usually is located in the middle of the tube. While the liquid oscillates in the tube, the orifice causes head loss, resulting in energy dissipation. The blocking ratio of the orifice, the natural frequency of the fluctuation of the liquid in the damper (natural frequency of the TLCD) and the mass of the TLCD are parameters that affect the efficiency of the damper. These parameters should be tuned properly in consideration of the dynamic specifications of the main structure [18].

Using a numerical method, Lee et al. [19] studied a typical tension leg platform (TLP) with a TLCD on its deck in order to decrease the wave-induced 2D motion of the platform. Their parametric analysis considered the pontoon diameter, pontoon draft, and the total mass of the platform, but overlooked changes in the TLCD parameters. They used the well-known equation of motion for liquid in a TLCD (governing equation) presented by Sakai et al. [20]. This equation is derived for a TLCD moving in a single horizontal direction, although floating platforms tend to experience vertical and rotational motions. They focused on surge motion and stated that the optimum natural frequency of the TLCD is equal to the surge natural frequency of the platform. However, floating platforms commonly experience low natural frequencies and a TLCD would have to be much wider than the platform in order to have the same frequency [21].

A TLP equipped with an underwater TLCD (UWTLCD) was studied experimentally by Lee and Juang [22]. The columns of the platform were used as the vertical parts of the TLCD and were connected by a small-diameter horizontal tube. Thus, the platform was equipped with a TLCD that did not occupy space on the deck. The effectiveness of the UWTLCD was investigated for the surge, heave and pitch motions in regular waves. The pontoon draft, tether pretension force and liquid length in the TLCD, which affects its mass and natural frequency, were considered in their parametric study.

Coudurier et al. [23] proposed a tuned liquid multi-column damper (TLMCD) to dissipate the energy of waves having various angles of incidence. They numerically applied the proposed damper to a barge-type floating wind turbine by focusing on rotational motion. The natural frequency of the damper was tuned to the same roll/pitch natural frequency of the barge platform. The optimized blocking ratio of the orifice was calculated for an arbitrary mass of the damper at a constant wave height.

In the present study, application of a TLCD for a large floating platform (GVA4000 semisubmersible) with long natural periods is investigated numerically and surge, heave and pitch motions of the platform are studied. Since the real-time response of the platform in irregular waves is calculated, the difference-frequency wave forces are included as well as the wave frequency forces. Thus, the low-frequency and wave-frequency motions of the platform are considered. Capturing the low-frequency motions of floating platforms is an important issue which is not considered in the previous studies. This would cause ignoring some important phenomena in platform motions. A more complete form of the governing equation of liquid fluctuation in the TLCD is derived in section 2, which takes into consideration the effects of transitional and rotational motion of the platform.

Since there is no experimental data available for application of a TLCD on a large semisubmersible such as the GVA4000, first, the case study platform is simulated without a damper. The Results are used in section 3 to verify the numerical modeling by comparing the simulation results with the available experimental data. Then, the platform-TLCD system is simulated and a parametric study is carried out to consider the performance of applying TLCD for reducing the platform motions. Results of the platform-TLCD system responses are discussed in section 4. The natural frequency, blocking ratio of the orifice and mass ratio of the TLCD are the study parameters. Section 5 presents the conclusions.

2. Governing equations of liquid fluctuation in TLCD and generated loads

There are two approaches for mathematical modeling of a structure with TLCD system. In the first approach, the whole system is considered as a single unit and the equation of motion for the structure and damper is derived simultaneously, as done by Holden et al. [24]. In the second method, motion of the main structure is calculated using an appropriate numerical model and the TLCD-induced forces are computed separately and applied to the structure [25,26]. The first method derives and solves the equation of motion of a coupled system for any type of structure. Because dynamics of various types of fixed and floating structures are complicated, it is better to solve the equation of liquid fluctuation inside the damper separately. The damper-induced forces can be calculated for exertion on the structure using the second method.

Hochrainer [27] introduced a method to derive the governing equation of liquid motion in a U-shaped TLCD (Fig. 1) for the transitional motion of the damper in the horizontal (*X*) and vertical (*Z*) directions as follows:

$$L_{eq}\ddot{w} + \frac{1}{2}\xi\dot{w}|\dot{w}| + 2gw = -B.\ddot{X} - \ddot{Z}(2w) \quad (2.1)$$

where, w, $\dot{w}$ and $\ddot{w}$ denote the magnitudes of liquid displacement, velocity and acceleration in the vertical parts of the tube, respectively, and $\ddot{X}$ and $\ddot{Z}$ are the magnitudes of horizontal and vertical acceleration of the damper. The positive direction for liquid motion is assumed to be from left to right in the horizontal tube (as the liquid surface moves down in the left vertical tube and moves up in the right one) . As shown in Fig. 1, B and A_h are the length and cross-section area of the horizontal tube, A_v is the cross-section area of the vertical tubes, H is the initial height of the liquid in the vertical tubes and L is the total length of the liquid in the tube ($L = 2H + B$).

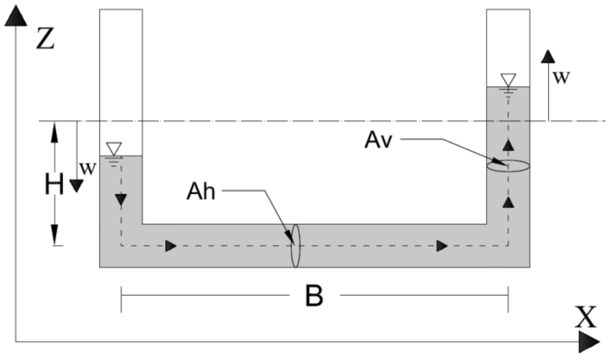

Fig. 1. U-Shaped TLCD with transitional motion.

Finally, L_{eq} is defined as:

$$L_{eq} = L - B\left(1 - \frac{A_v}{A_h}\right) \tag{2.2}$$

Parameter ξ is the head loss coefficient of the TLCD and is related to the blocking ratio of the orifice (ratio of the area enclosed by the orifice to the total area of the horizontal tube) calibrated from the experiment results. Wu et al. [18] calibrated this coefficient by conducting forced harmonic vibration tests for uniform sections of TLCDs of various dimensions and blocking ratios as summarized in Table 1.

They concluded that ξ is not a function of TLCD natural frequency, but is mainly related to the blocking ratio. They proposed a formula for calculating ξ as a function of blocking ratio [18] as:

$$\xi = (-0.6\psi + 2.1\psi^{0.1})^{1.6}(1-\psi)^{-2} \tag{2.3}$$

where ψ is the blocking ratio of the orifice inside the damper.

Table 1. Calibration tests results for head loss coefficient of TLCD [18]

Blocking ratio (ψ)	Natural frequency (Hz)			
	0.4923	0.4727	0.4595	0.4516
	Head loss coefficient: (ξ)			
20%	3.96	3.55	3.40	3.40
40%	6.10	5.80	5.70	5.55
60%	12.80	12.40	12.50	12.00
80%	54.50	54.00	59.00	56.00

The rotational motion of the TLCD is extensively studied by Xue et al. [28]; Suduo et al. [29] and Taflanidis et al. [30]. For a TLCD rotating around a fixed point, the governing equation of liquid fluctuation is [28]:

$$\begin{gathered} L_{eq}\ddot{w} + \frac{1}{2}\xi\dot{w}|\dot{w}| + 2gw = \\ -B\left(\ddot{\theta}\left((L-B)/2 + D\right) + g\theta\right) \end{gathered} \tag{2.4}$$

in which θ and $\ddot{\theta}$ denote the magnitudes of rotating angle and rotational acceleration, respectively, and D is the distance of the horizontal tube of the TLCD from the rotating center (Fig. 2).

The governing equation of liquid fluctuation in a TLCD is often derived for a moving system with a single degree of freedom. A semisubmersible platform may has large displacement at all degrees of freedom (DOF) [31]. Therefore, when using a TLCD on this type of structure, it is important to derive the governing equation such that the effects of all motions are taken into account. For the combined rotation and transition of the TLCD, the superposition principle cannot be used because of the nonlinear behavior of the liquid fluctuation inside the damper. Thus, the governing equation for a damper experiencing simultaneous transitional and rotational motions should be derived exclusively.

Coudurier et al. [23] presented TLCD equations for combined transition and rotation; however, their equations were derived in a complicated format which does not clearly represent the physical process and is very difficult to compare with well-known equations in the literature. The equations are also difficult to apply.

The formulation proposed in the current study is derived in a simple format that is analogous to the well-known form presented in the literature. When applying a TLCD to a floating structure, coordinate system *XOZ* is considered to be fixed on a water free surface as shown in Fig. 2. The floating body is defined using its center of mass (*G*) and 3 DOF (*X*, *Z* and *θ*) with a TLCD attached to the floating body. Assuming that the energy of the liquid remains constant during the motion of the TLCD, the Lagrange equation can be applied as follows [32]:

$$\frac{d}{dt}\left(\frac{\partial(T-U)}{\partial\dot{w}}\right) - \frac{\partial(T-U)}{\partial w} = Q \tag{2.5}$$

where *U* and *T* are the potential and kinetic energy of the liquid, respectively, and *Q* represents the magnitude of non-conservative force acting on the liquid in the following form [32]:

$$Q = -\frac{1}{2}\rho r A_v \xi|\dot{w}|\dot{w} \tag{2.6}$$

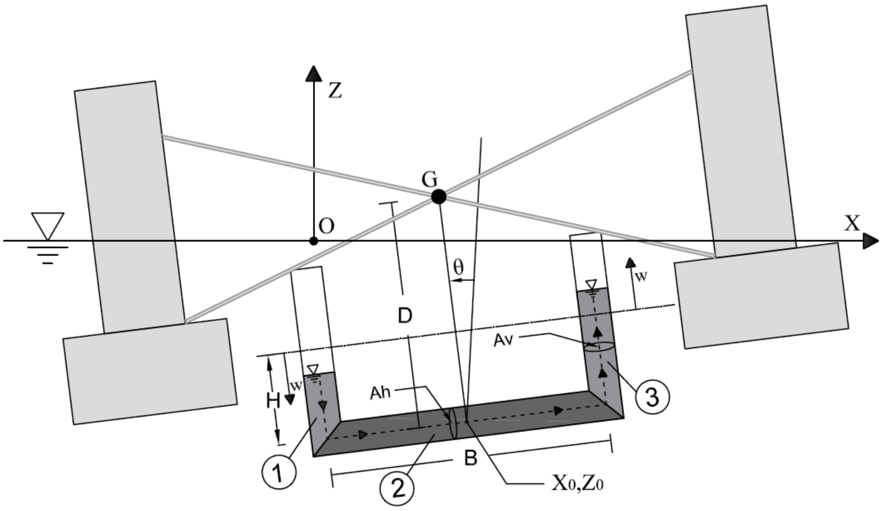

Fig. 2. U-Shaped TLCD attached to floating platform experiencing combined rotation and transition.

For relatively small rotation angles ($\theta < 10°$), $\cos(\theta)$ and $\sin(\theta)$ are estimated to be 1 and θ, respectively, $[\cos(\theta)\sim 1\ ,\ \sin(\theta)\sim\theta]$. In order to calculate the kinetic energy of the liquid ($T = 1/2.\mathrm{m}V^2$), the magnitudes of total velocities along the vertical and horizontal tubes can be written as follow for the three portions of the damper:

$$V_1 = \dot{w} + \frac{\dot{\theta}B}{2} + \dot{X}\theta - \dot{Z} \tag{2.7}$$

$$V_2 = r\dot{w} + \dot{\theta}D + \dot{X} + \dot{Z}\theta \tag{2.8}$$

$$V_3 = \dot{w} + \frac{\dot{\theta}B}{2} - \dot{X}\theta + \dot{Z} \tag{2.9}$$

in which *r* denotes the ratio of A_v to A_h ($r = A_v/A_h$) and $\dot{X}$ and $\dot{Z}$ denote the magnitudes of horizontal and vertical velocities of the structure. The average heights of the three portions of the TLCD, according to the potential energy of the liquid ($U = mgZ$), can be defined as:

$$Z_{ave,1} = Z_0 - \frac{B}{2}\theta + \frac{1}{2}(H - w) \tag{2.10}$$

$$Z_{ave,2} = Z_0 \tag{2.11}$$

$$Z_{ave,3} = Z_0 + \frac{B}{2}\theta + \frac{1}{2}(H + w) \tag{2.12}$$

By calculating the kinetic and potential energy of the damper liquid and substituting these values into Eq.(2.5), the governing equation of liquid motion in TLCD becomes:

$$L_{eq}\ddot{w} + \frac{1}{2}r\xi\dot{w}|\dot{w}| + 2gw \ = \\ [-B.\ddot{X}] + [-\ddot{Z}(2w)] + \left[-B\left(\ddot{\theta}\left(\frac{(L-B)}{2} + D\right) + g\theta\right)\right] + [-\ddot{Z}B\theta + 2w\ddot{X}\theta + 2w\dot{X}\dot{\theta} - B\dot{\theta}\dot{X}\theta] \tag{2.13}$$

X-term *Z-term* *θ-term* *Additional terms*

This equation describes liquid fluctuation in a TLCD as the result of the simultaneous motion at all 3 DOF. For purely transitional movement of the damper, all terms containing θ should be omitted from Eq.(2.13), which then becomes the Eq.(2.1) as previously derived for damper transition. Similarly, for purely rotational movement of the damper, all terms containing X and Z should be omitted from Eq.(2.13), which then becomes the Eq.(2.4). The equation derived here has a form that is similar to previously derived equations; thus, its validity can be demonstrated by comparing with equations that are verified in previous studies.

The right-hand side of Eq.(2.13) shows that the first three terms are the components of TLCD motion at 3 DOF. These three terms are related to pure structure motions in the *X* (surge), *Z* (heave) and *θ* (pitch) directions, respectively. These are denoted as the *X*-term, *Z*-term and *θ*-term, respectively. There are four additional terms on the right-hand side of Eq.(2.13) which are the results of simultaneous motion of the dampers at 3 DOF and are denoted as "additional terms". The magnitudes of these seven terms will determine the effects of structural motions on TLCD excitation and are denoted as "excitation terms". Section 4 compares the magnitude and effect of each term on damper efficiency for the specified conditions.

The natural frequency of the TLCD is an important characteristic of this damper and can be estimated as [12]:

$$f_{TLCD} = \frac{1}{2\pi}\sqrt{\frac{2g}{L_{eq}}} = \frac{1}{2\pi}\omega_{TLCD} \tag{2.14}$$

The main structural dimensions limit the total equivalent length of the liquid in the damper (L_{eq}) and prevent the setting of an arbitrary value for it. The tuning ratio equals $f_{TLCD}/f_{Structure}$ and an appropriate quantity for this ratio is 0.95 to 1.05 [12,19].

The loads generated by the TLCD can be calculated as [25, 26]:

$$F_X = -\rho A_h B\ddot{w} - \rho(A_h B + 2HA_v)\ddot{X} \tag{2.15}$$

$$F_Z = -\rho(2A_v w\ddot{w}) - \rho(A_h B + 2HA_v)\ddot{Z} \tag{2.16}$$

$$M_\theta = -\rho A_v B\left(\frac{(L-B)}{2} + D\right)\ddot{w} - \rho g A_v\left(\left((\mathrm{L}-\mathrm{B}) + B\frac{A_h}{A_v}\right)D\theta + Bw\right) - I_d\ddot{\theta} \tag{2.17}$$

where $\boldsymbol{F_X}$, $\boldsymbol{F_Z}$ and $\boldsymbol{M_\theta}$ are the magnitudes of forces exerted on the mass-center of the platform by the TLCD in the *X, Z* and *θ* directions, respectively, and $\boldsymbol{I_d}$ is the moment of inertia of the damper liquid about the mass center *G*. Other parameters have been defined previously. It is important to note that these equations have been updated for a non-uniform TLCD cross-section.

3. Numerical modeling

Characteristics of a GVA4000 drilling semisubmersible are used to model the effects of a TLCD on its response mitigation by considering available experimental data for hydrodynamic motion of the platform [33]. This semisubmersible platform has already been tested using a 1:81 scale model by Clauss et al. [33] to calculate its RAOs for the heave and pitch motions. The main dimensions and characteristics of the platform model are shown in Fig. 3 and Table 2.

Numerical modeling is carried out in two stages. The hydrodynamic specifications of the platform are determined at the frequency-domain stage. This is followed by the time-domain stage in which platform motions are determined under the influence of irregular waves. Then, the forces and moment induced by the TLCD are calculated and applied to the structure using Eqs. (2.15) to (2.17). The motions are determined by ANSYS-AQWA (17.0) at each time-step and the related TLCD loads are applied to the platform using a Fortran code in an external dynamic library link file. This Fortran code solves the governing equation of the TLCD (Eq.(2.13)) at each time-step using the Newmark-beta method [34] and then calculates the damper forces.

Accuracy of numerical modeling of the platform (without TLCD) is confirmed by comparing the results with available experimental data.

However, since there is no any experimental data available on application of a TLCD to a large semisubmersible, the validity of the new derived Eq.(2.13) is investigated by comparing it with Eq.(2.1) and Eq.(2.4) which are validated several times in the literature.

Table 2. Characteristics of GVA4000 model

Structure characteristics	Value
Mass center *X* (m)	0
Mass center *Y* (m)	0
Mass center *Z* (m)	0.85
Mass (kg)	25834154
K_{xx}, K_{yy}, K_{zz} (m)	30.4, 31.06, 37.54
Water depth (m)	121
Mooring line length (m)	400
Mooring line density (kg/m)	140
Mooring line stiffness *EA* (kN)	500000
Natural frequencies f_{surge}, f_{heave}, f_{pitch} (results of decay test models)	0.008, 0.046, 0.015

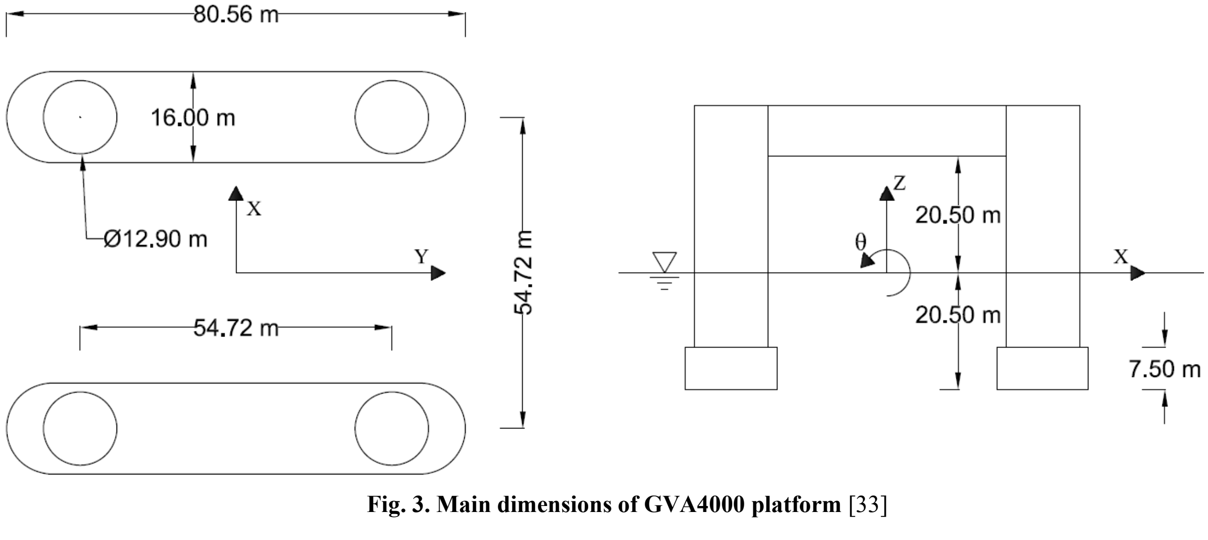

Fig. 3. Main dimensions of GVA4000 platform [33]

3.1. Frequency-domain analysis without TLCD

ANSYS-AQWA employs a combination of the Morison's equation for slender elements (Morison's elements) and the radiation/diffraction theory for large ones. It calculates the fluid velocity potential based on the following assumptions [35]:

- The body has zero or slight forward speed.
- The fluid is inviscid and incompressible and the fluid flow is irrotational.
- The incident regular wave train is of small amplitude compared to its length (small slope).
- The motions are first-order and must be of small amplitude.

The velocity potential is composed of the incident, diffracted and radiated waves of the floating structure and has the following form:

$$\varphi(\vec{X})e^{-i\omega t} = \left[(\varphi_I + \varphi_d) + \sum_{j=1}^{6} \varphi_{rj} x_j\right] e^{-i\omega t} \qquad (3.1)$$

where φ_I is the first-order incident wave potential at unit wave amplitude, φ_d is the corresponding diffracted wave potential, φ_{rj} is the radiation wave potential due to the j^{th} motion at unit amplitude and x_j is the motion amplitude of the j^{th} DOF excited by an incident regular wave at unit amplitude [35].

The radiation potential results in pressure fields and forces on the surface of the floating body. The component of the forces that is in phase with the body velocity acts as a damping term and the out-of phase component which is in phase with the body acceleration acts as an inertia term. This component is called the added mass term [36].

The Morison's equation also includes a force component due to body acceleration which contributes to the total added mass. The other force component in the Morison's equation is in phase with the body velocity. The latter one is called the drag force.

Using the aforementioned theory, ANSYS-AQWA (17.0) is applied to calculate the platform RAOs. Then, the calculated RAOs are compared with the experimental data given by Clauss et al. [33] as represented in Fig. 4 and Fig. 5. A qualitative comparison shows that the present numerical results match well with the experimental data. The frequency domain results show that the numerical model is capable of calculating the platform motion with acceptable precision. Section 4 discusses the application of the TLCD to the modeled semisubmersible platform.

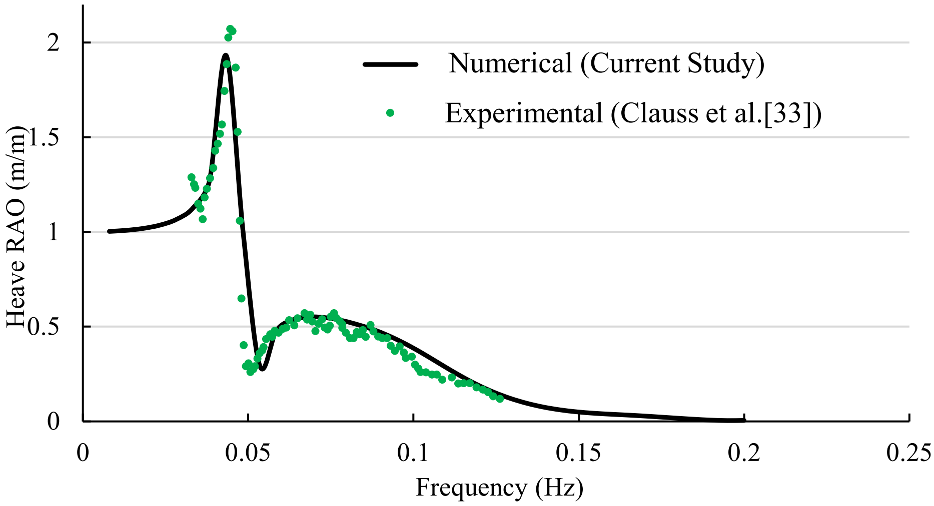

Fig. 4. Comparison of heave RAO for current study and Clauss et al. [33].

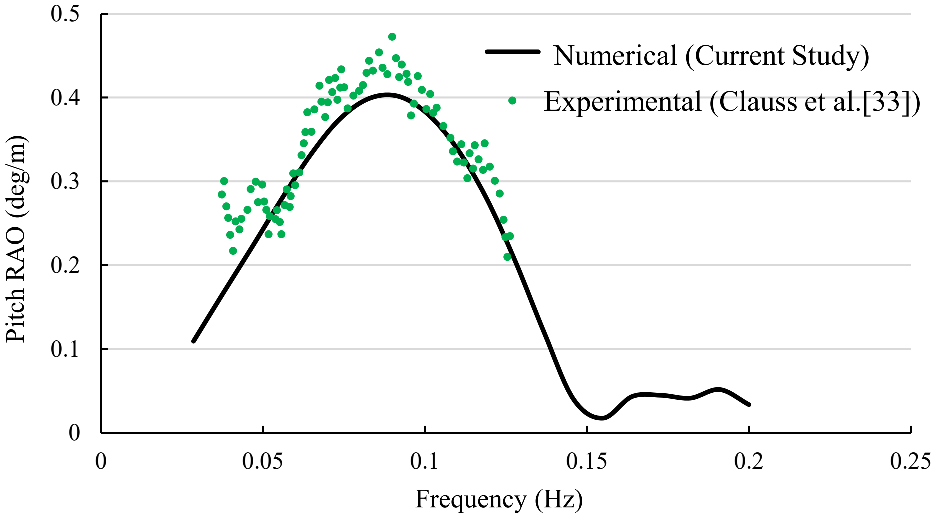

Fig. 5. Comparison of pitch RAO for current study and Clauss et al. [33]**.**

3.2. Time domain analysis with TLCD

ANSYS AQWA is capable to simulate the real-time motion of a floating body under irregular waves. Wave-frequency motions and low period oscillatory drift motions may be considered. The difference-frequency and sum frequency second order forces are calculated at each time step in the simulation, together with the first order wave frequency forces and instantaneous values of all other forces. This, can also provide calculating wave drift damping which is induced by nonlinear surface wave effects [37].

The configurations used to investigate the influence of the TLCD on response of the semisubmersible platform are summarized in Table 3. In each study condition, two TLCDs are mounted on the platform in which their vertical tubes are located inside the platform's columns (Fig. 9). The head loss coefficient, natural frequency and mass ratio ($M_{TLCD\ Fluid}/M_{Structure}$) are examined as the main variables that affect platform motion. Different values for parametric analysis are set for each variable while keeping the other two variables constant. The dimensions of the TLCD are determined by considering the GVA4000 hull dimensions. In all models, the damper width is 55 m and the total length of the liquid in the tube is 85 m with a density of 1000 kg/m^3.

Table 3. TLCD configurations in parametric analysis

Selected specification of TLCD for parametric study	A_v (m^2)	A_h (m^2)	f_n(Hz) [T (s)]	Mass ratio (%)	Head loss coefficient (ξ)
Head loss coefficient (ξ)	2×5.10 (D = 2.55)		0.077 [13.07]	3.44	3.50 5.50 12.50 55.00
Natural frequency (period)	2×5.10 (D_v = 2.55) 2×7.54 (D_v = 3.1) 2×10.17 (D = 3.6)	2×5.10 (D_h = 2.55) 2×3.46 (D_h = 2.1) 2×1.77 (D = 1.5)	0.077 [13.07] 0.058 [17.36] 0.038 [26.41]	3.44	55.00
TLCD /Structure mass ratio	2×0.126 (D = 0.4) 2×1.77 (D = 1.5) 2×3.46 (D = 2.1) 2×9.62 (D = 3.5) 2×12.56 (D = 4.0) 2×15.90 (D = 4.5) 2×19.62 (D = 5.0) 2×23.75 (D = 5.5) 2×28.26 (D = 6.0)		0.077 [13.07]	0.08 1.2 2.3 6.49 8.47 10.72 13.24 16.02 19.06	55.00

Similar to results of Wu et al. [18], the head loss coefficient of the damper is estimated to be 3.5 to 55 for blocking ratios of 20% to 80%. The largest structure-TLCD mass ratio is 19%, which is a large ratio for liquid dampers. An extremely small value of 0.08% is selected to investigate the extreme condition. The natural frequency of the TLCD is varied from 0.038 to 0.077Hz because of the restrictions related to the structural dimensions. It is not possible to tune the structure-TLCD frequency ratio to approach 1 as recommended in previous studies. The natural frequency of the platform is estimated by conducting decay test models. Because mooring lines stiffness would affect the natural frequency of the platform, using the timed domain modelling which is capable to capture the mooring lines dynamics is preferred. For the surge, heave and pitch motions, the natural frequencies of the platform are calculated to be 0.008, 0.046 and 0.015 Hz, respectively. The results of the decay tests are shown in Fig. 6 to Fig. 8.

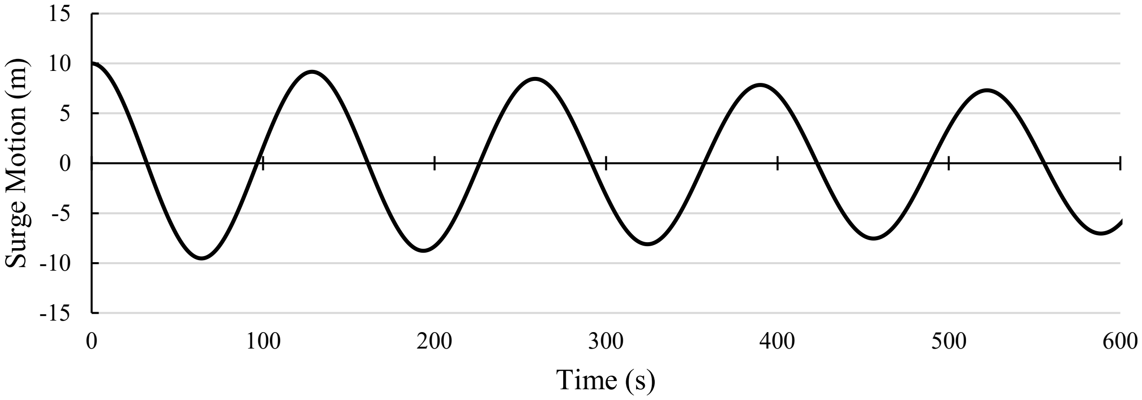

Fig. 6. Decay test model results for surge motion of GVA4000 platform (without TLCD)

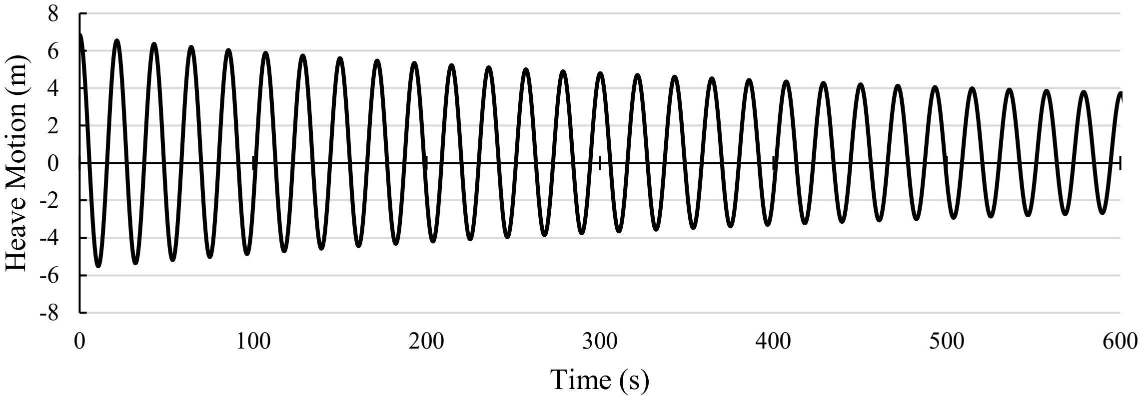

Fig. 7. Decay test model results for heave motion of GVA4000 platform (without TLCD)

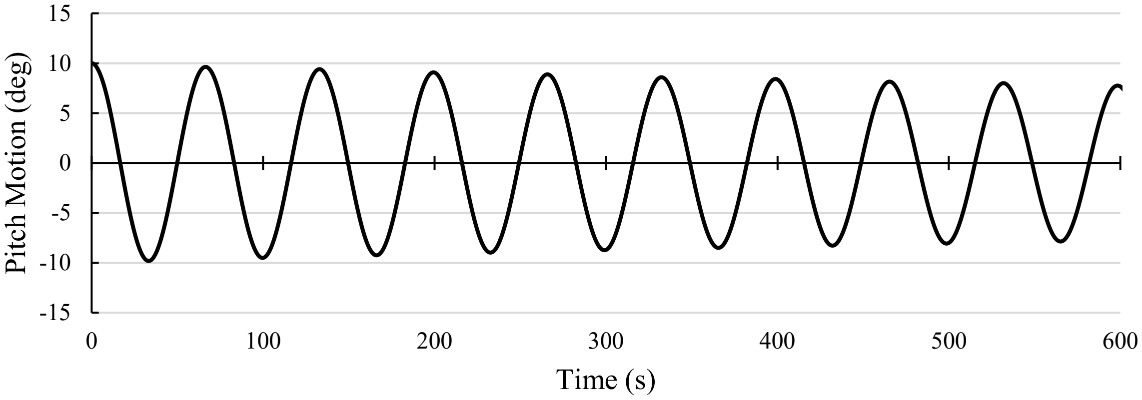

Fig. 8. Decay test model results for pitch motion of GVA4000 platform (without TLCD)

Time series of irregular waves with significant wave height of 5 m (H_s = 5 m) and peak frequency of 0.09 Hz (T_p = 11 s) is generated based on the JONSWAP spectrum. A schematic view of TLCD placement onto a GVA4000 semisubmersible is shown in Fig. 9. In this figure global directions of reference coordinate axes are defined. But it should be considered that the precise definition of reference coordinates is shown in Fig. 2. It is assumed that the waves are propagating in X direction. The selected sea state is related to the 1-

year return period wave characteristics in the Caspian sea which is applied as the operational condition as recommended by API [38]. The time series of the water surface elevation for the sea state is shown in Fig. 9

In time-domain analysis, ANSYS-AQWA facilitates the use of additional formulations through the dynamic link library (DLL). This feature is used to introduce the external loads exerted by the TLCD at each time-step using the external DLL built from the Fortran code. The code determines the platform position and velocity as inputs, calculates the TLCD forces and presented them to ANSYS-AQWA as external forces to be exerted on the platform. The positions and velocities of the platform are determined at each time-step by integrating the accelerations from all hydrodynamic and TLCD forces.

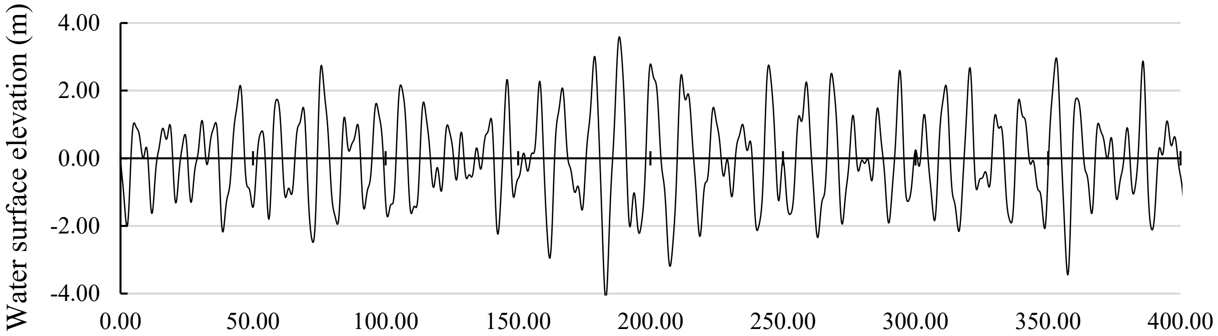

Fig. 9. Water surface elevation of the selected sea-state (Hs=5 m, Tp=11 s)

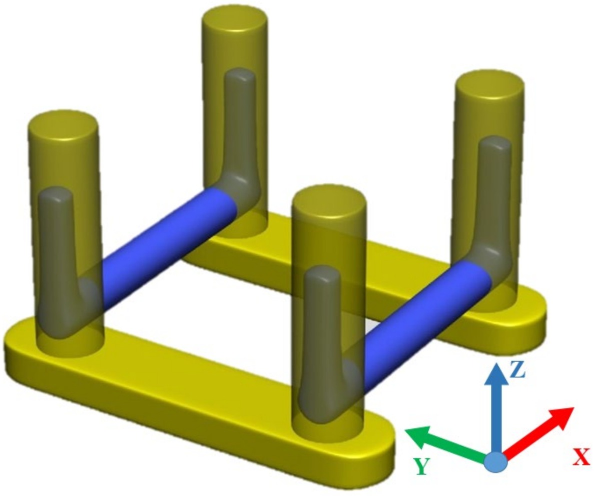

Fig. 10. Schematic view of TLCD on GVA4000 semisubmersible floating platform.

4. Results and discussion

Time-domain analysis of the floating platform response is carried out with and without the TLCD in different configurations as shown in Table 3. However, for better evaluation of the results, all response time histories are transformed into frequency domain by the fast Fourier transform[1] method. It is evident from the modeling results that the dynamic energy of the structure is concentrated at two frequency ranges for 3 DOF. Fig. 10 to Fig. 12 show a major peak near the natural frequency of the platform in each direction and a smaller peak close to the peak wave frequency. The major peak is the result of the difference-frequency forces of the irregular waves, which cause resonance in the natural frequency of the platform as described by Keddam [39]. This peak is about 100 times higher than that of the minor peaks for surge. But for heave and pitch motions the values of the two peaks are close together.

---

[1] FFT

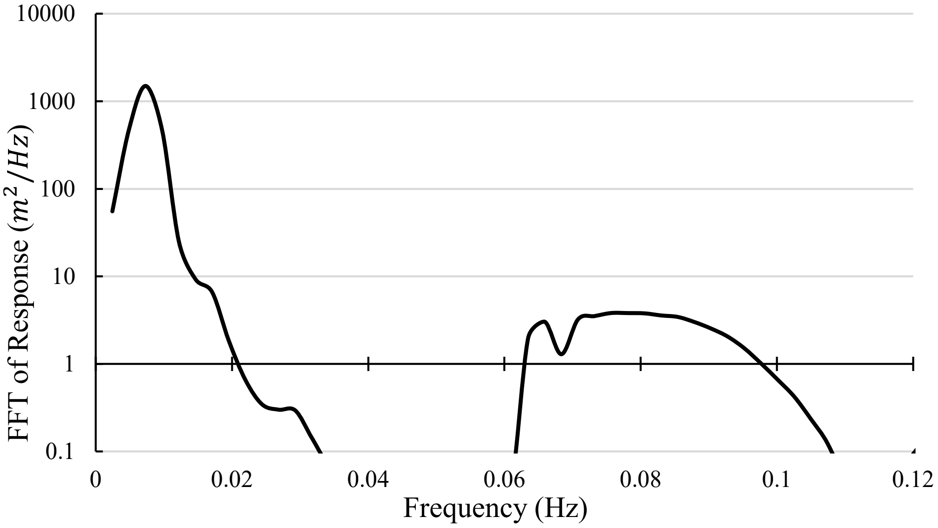

Fig. 11. Surge response without TLCD (logarithmic scale).

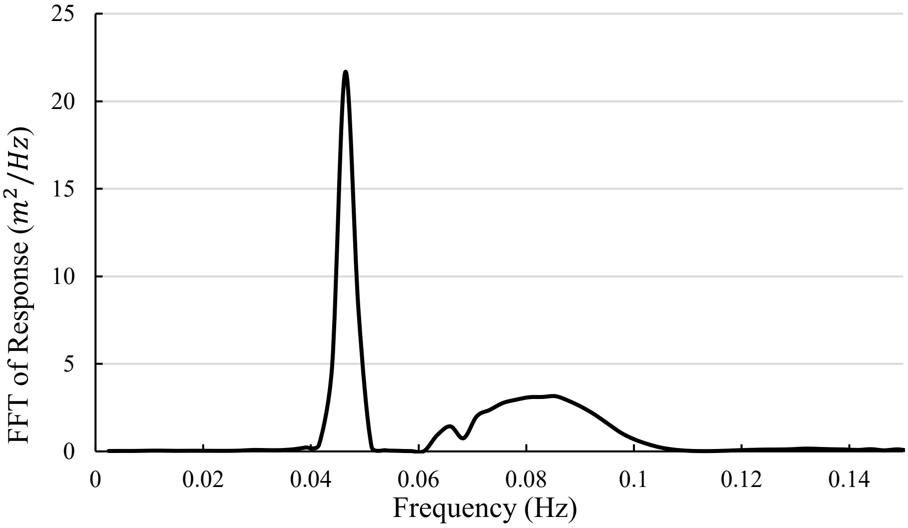

Fig. 12. Heave response without TLCD.

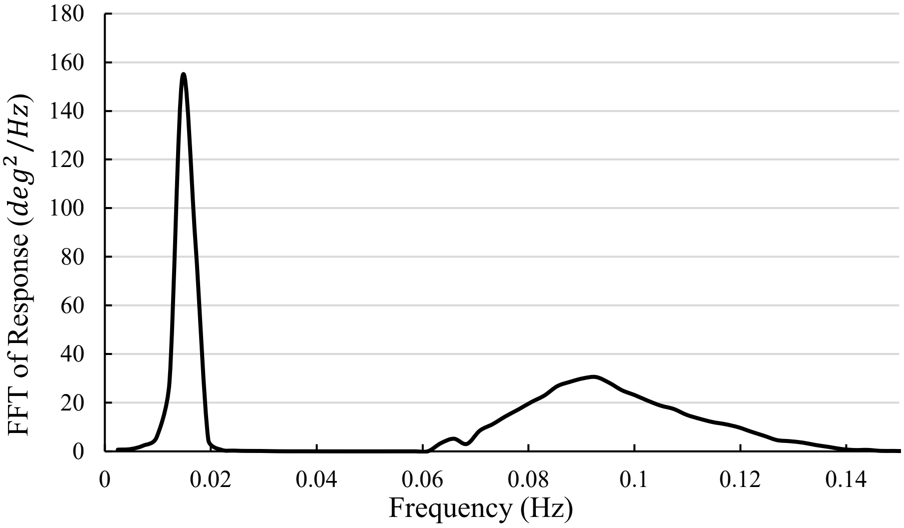

Fig. 13. Pitch response without TLCD

Comparing the fast Fourier transformed response of the structure with and without a TLCD, shows that there are no significant changes in the surge and heave motions. However, a considerable decrease can be seen for the pitch motion in the range of the natural frequency of the platform, but no decrease occurs at the wave frequency motion.

Liquid fluctuation in the TLCD and the resulting forces are dominated by platform motion, which excites the damper; thus, most of the damper forces are generated at low frequencies in accordance with the platform motion. By contrast, the wave force is accumulated at the wave frequencies where the damper force is negligible. This is why the effect of the TLCD on platform motion is significant only at low frequencies.

In order to explain the aforementioned phenomenon, wave induced forces and moments are compared with TLCD induced ones in Fig. 13 to Fig. 18 .The fast Fourier transformed forces and moments are displayed in these figures in wave-frequency and low-frequency ranges separately. It can be seen that in wave-frequency range, TLCD induced forces are negligible in comparison with wave induced ones. In low frequencies (near the natural frequency of the platform) TLCD induced moments are dominated in pitch motion. But in surge and heave motions, again wave induced forces are dominated.

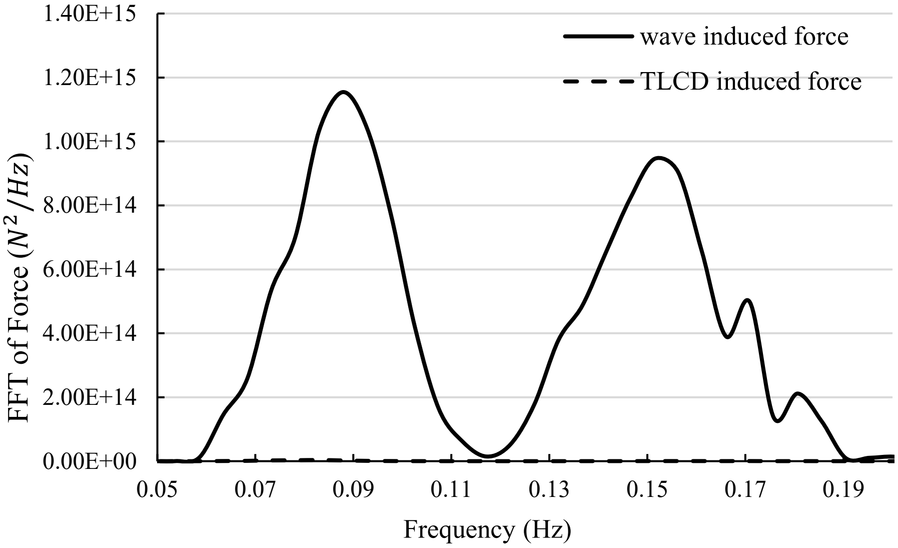

Fig. 14. Wave-frequency forces in surge direction

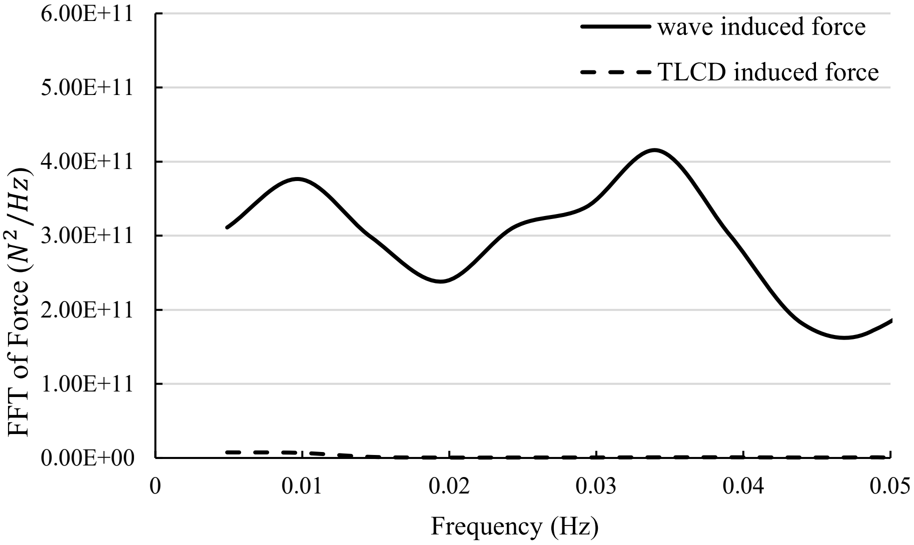

Fig. 15. Low-frequency forces in surge direction

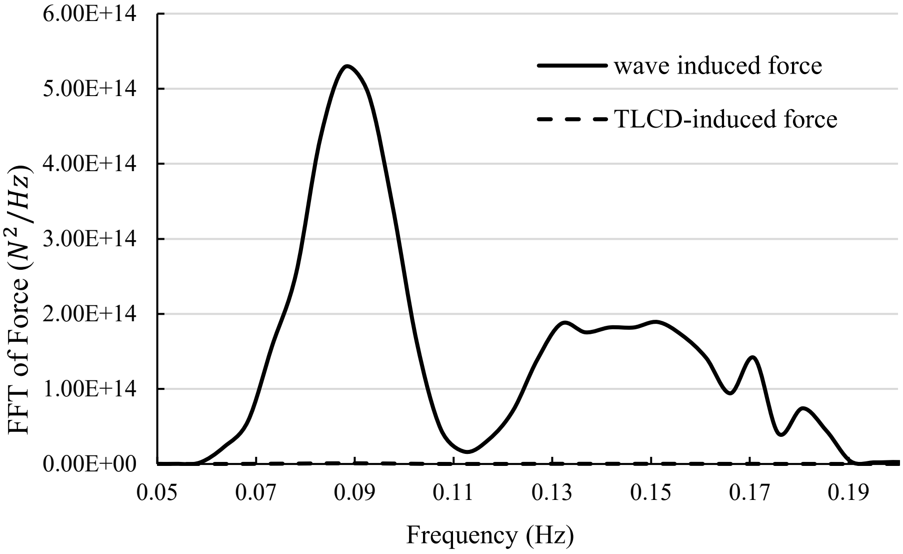

Fig. 16. Wave-frequency forces in heave direction

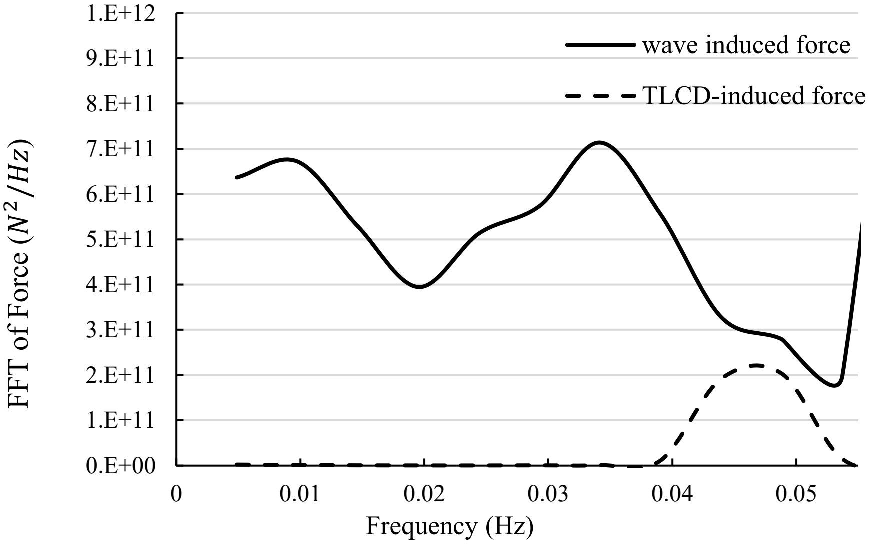

Fig. 17. Low-frequency forces in heave direction

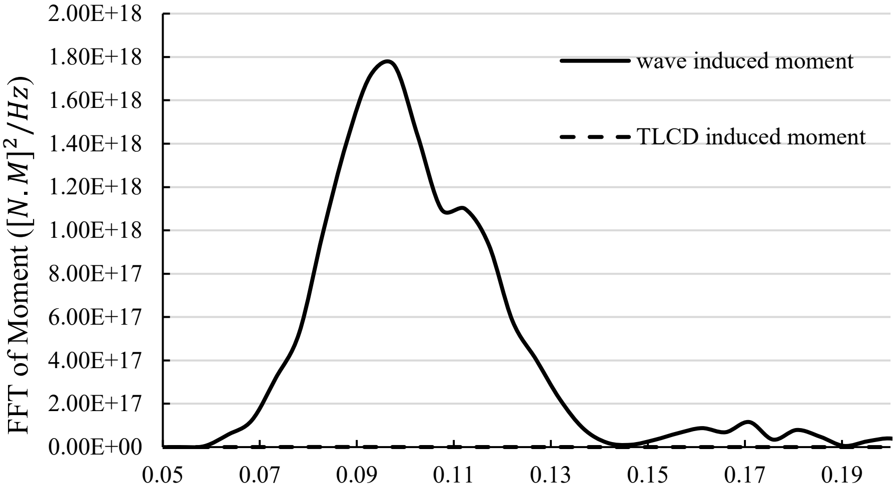

Fig. 18. Wave-frequency moment in pitch direction

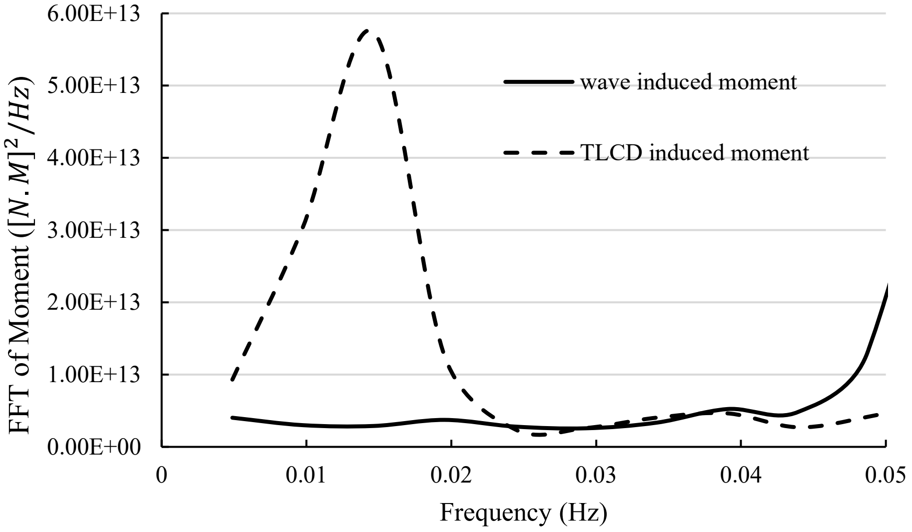

Fig. 19. Low-frequency moment in pitch direction

In the following sections, only results of pitch motion are presented, as no reduction is achieved in the surge and heave motions with a TLCD. For this reason, the pitch motion results are shown in the low frequency range, where the effect of the TLCD on platform motion is shown to be considerable.

4.1. Parametric analysis of platform response

4.1.1. Variation of head loss coefficient (ξ)

Table 3 lists four values for the head loss coefficient as they are related to the different blocking ratios of the TLCD orifice. These values are 3.5, 5.5, 12.5 and 55 for blocking ratios of 20%, 40%, 60% and 80%, respectively. The resultant FFT transformed responses are shown in Fig. 19. It can be seen that, for the case under study, the platform pitch motion is not affected by the damper when the blocking ratio does not exceed 40%. Beyond that, the damper efficiency increased as the blocking ratio of the damper orifice is increased up to 80%.

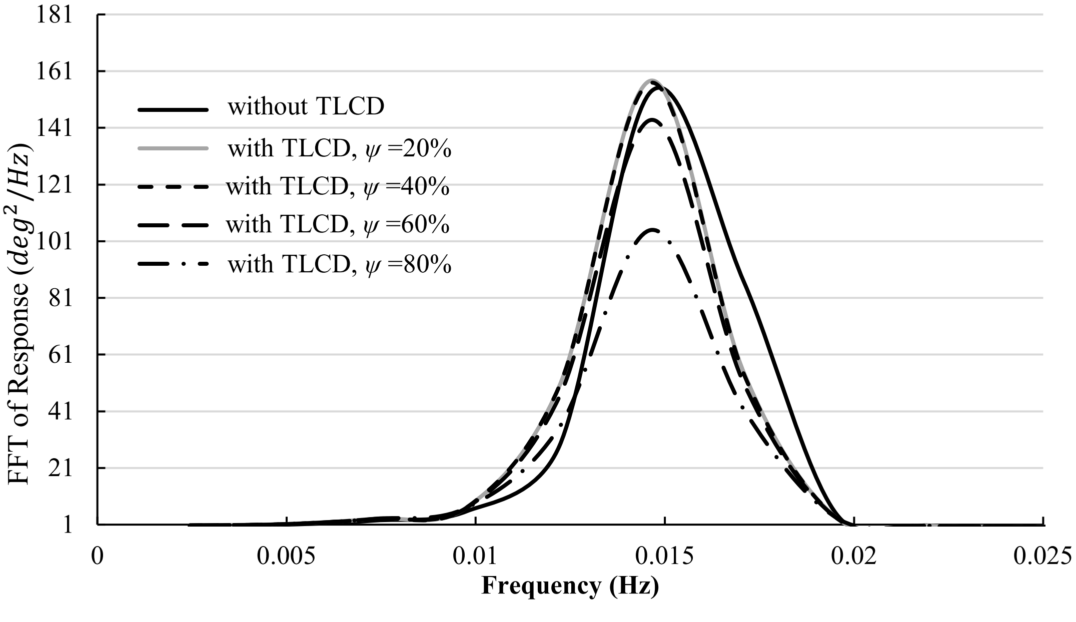

Fig. 20. Low-frequency pitch response vs. TLCD head loss coefficient.

4.1.2. Variation of natural frequency (f_{TLCD})

The TLCD frequency affects its efficiency and it is recommended to be equal to the natural frequency of the main structure [12,18,40]. However, it is not possible to tune the damper as recommended because of the dimensions of the floating platform and TLCD. At $A_v/A_h = 1$, the equivalent length of the liquid in the damper (L_{eq}) is limited to 85 m. This results in a frequency of 0.077 Hz (T = 13.07 sec) with a platform frequency of about 0.015 for pitch motion. An increase in A_v/A_h to 5.76 decreases the damper frequency to about 0.038 Hz, which is still about three times the platform frequency.

Fig. 20 shows the low-frequency response of a platform with a TLCD at different natural frequencies.

Although the frequency of the TLCD is far higher than that of the platform, it is apparent that damper efficiency is increased with decreasing the tuning ratio ($f_{TLCD}/f_{Structure}$) to 1.

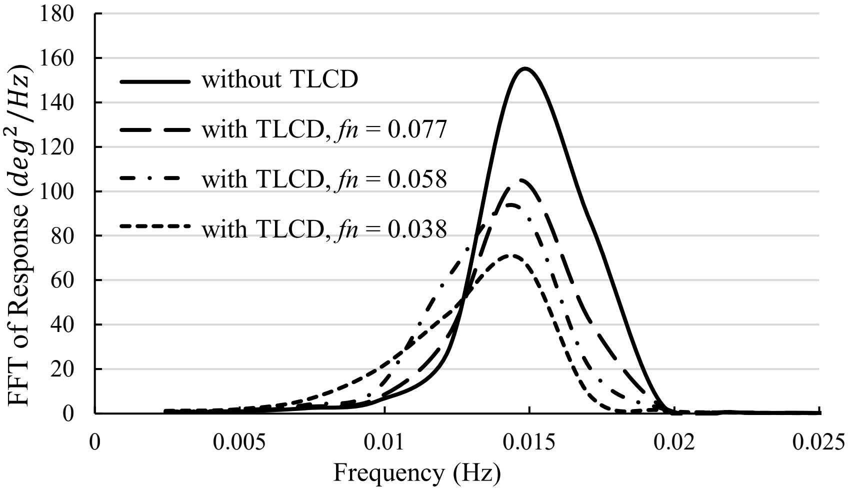

Fig. 21. Pitch low-frequency response vs. TLCD natural frequency.

4.1.3. Platform-TLCD mass ratio

Gao et al. [12] stated that, the mass ratio should be less than 2% for civil engineering applications. However, Wu et al. [18] have presented design guidelines for TLCDs with mass ratios of up to 5%. Chatterjee and Chakraborty [40] studied TLCD mass ratios of up to 14%. In the present research, the mass ratio is varied from 0.08% to 19%, as greater ratios are not practical. It is appropriate to use a small mass ratio to determine the maximum efficiency of a TLCD. Fig. 21. The Abbreviation *MR* is defined for the mass ratio in this figure. shows the effect of TLCD mass ratio on the platform response. The efficiency of damper is denoted as the “motion reduction factor” and is defined as the percentage of decrease in the significant double amplitude of the platform response. Fig. 22 shows the motion reduction factor versus the TLCD mass ratio. As seen, the TLCD efficiency is increased by increasing the mass ratio up to 10%. Beyond that, the damper efficiency is deteriorated. This means that the optimum mass ratio of the damper of the floating platform is about 10%.

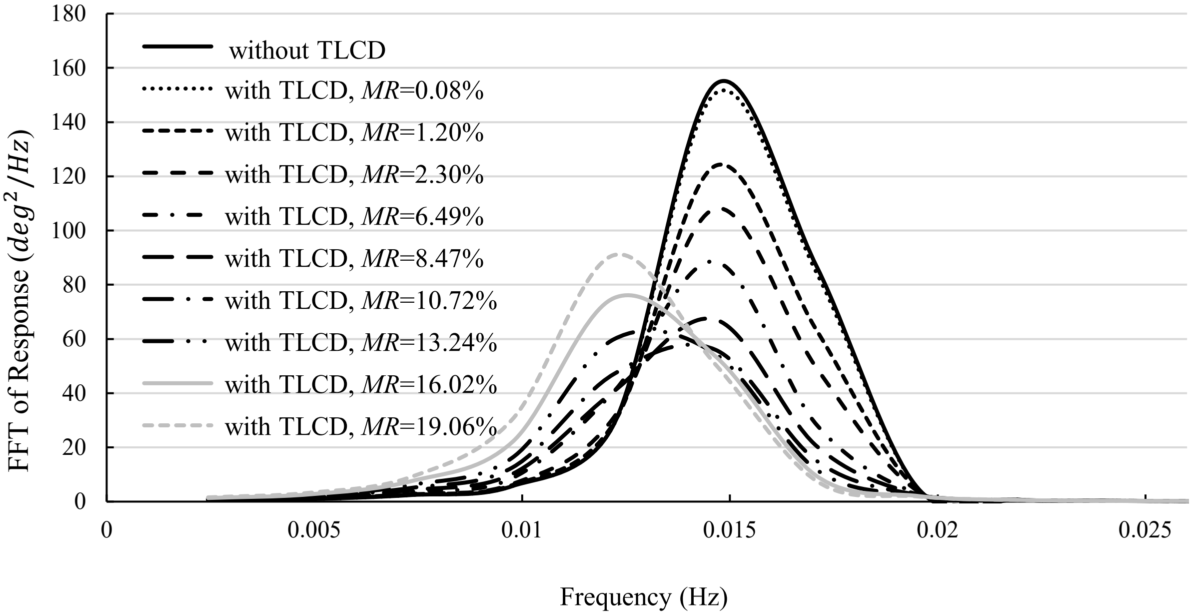

Fig. 22. Pitch low-frequency response vs. structure-TLCD mass ratio.

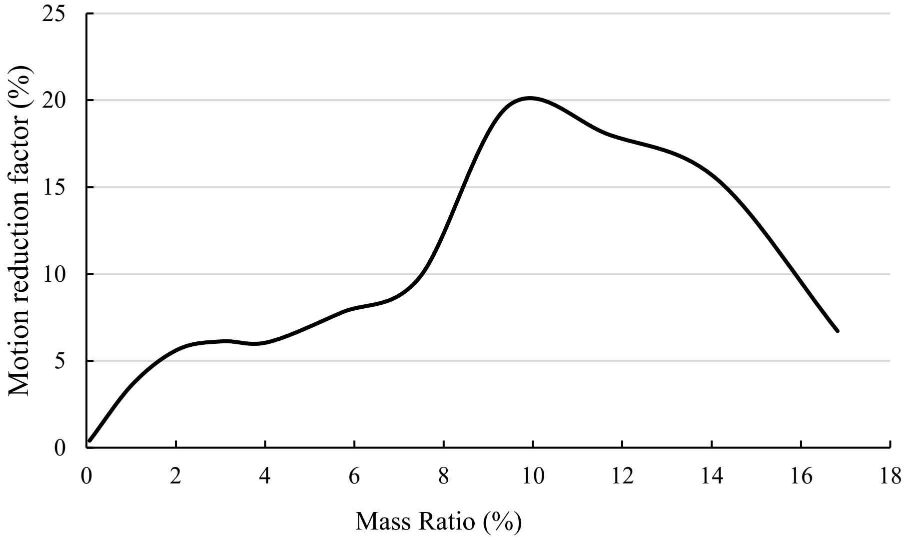

Fig. 23. Effect of TLCD mass ratio on motion reduction factor.

4.2. Effect of excitation term on TLCD function

As described in section 2, the terms on the right-hand side of Eq.(2.13) represent the effect of the motion of the structure-TLCD system on liquid fluctuation in the TLCD. The first three terms denote the pure horizontal, vertical and rotational motions. These variables are compared to determine the effect of platform motion at different DOF values on TLCD excitation. Values of additional terms are also compared to determine their effect on damper excitation.

In Eq.(2.13), the excitation terms are sensitive to the width of the TLCD (*B*), the length of the liquid in the tube (*L*) and the vertical distance of the rotating center from the horizontal tube (*D*). These parameters are kept constant in this parametric study. The excitation terms are compared at an optimum mass ratio of 10% and the results are depicted in Fig. 23. It can be seen that the *X*-term and *θ*-term for the surge and pitch motions of the platform have significant effects on TLCD excitation. The *Z*-term and additional terms show very small values when compared with those of the *X*-term and *θ*-term. It could be concluded that, the *Z*-term and additional terms have little influence on damper excitation for the GVA4000 in the defined wave condition.

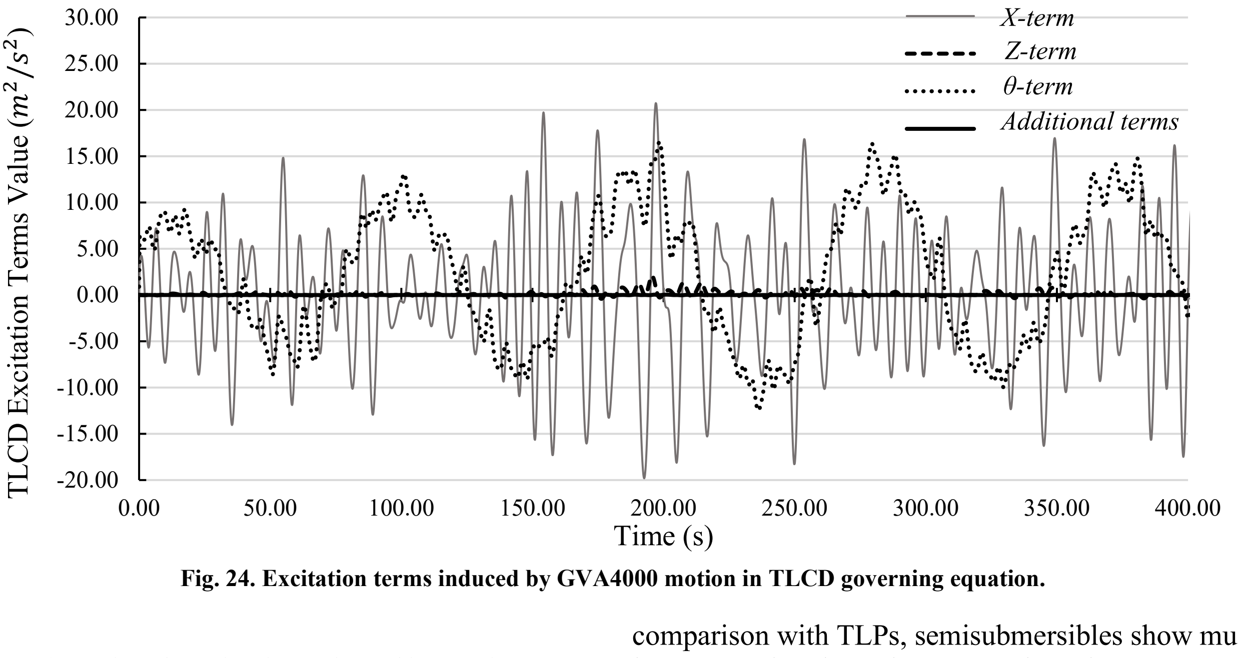

Fig. 24. Excitation terms induced by GVA4000 motion in TLCD governing equation.

The effect of rotational motion is neglected in previous studies, including those by Lee et al. [19], who studied the application of TLCDs to TLPs. It would be a suitable simplification method, because TLPs show high stiffness values in the heave and pitch directions, which lead to relatively slight motion [41]. In comparison with TLPs, semisubmersibles show much larger rotational motion [41]; thus, it may not be appropriate to ignore the effect of the rotational motion of a semisubmersible on TLCD excitation.

4.3. Effect of additional terms in governing equation of TLCD

Numerical modeling is performed again to determine the effect of the inclusion of the additional terms in the TLCD governing equation. Here, the additional terms are omitted from Eq.(2.13) and only the *X*-term, *Z*-term and θ-term are considered when calculating the motion of the liquid in the TLCD. The results are almost identical to those from the previous stage. No considerable effect is observed on the wave-frequency motion of the platform and the platform response in the surge and heave directions is not affected by the damper.

Because the results are very similar in the presence and absence of the additional terms, it is difficult to recognize the differences between the FFT transformed response diagrams.

Table 4 provides the computed motion reduction factors to allow better comparison of the results. It can be seen that the resultant reduction factors for both cases have negligible differences. This means that the inclusion of additional terms in the governing equation for TLCD has no effect on its efficiency.

Table 4. Effect of TLCD on platform motion with and without additional terms in governing equation

	TLCD characteristics			Motion reduction factor (%)	
Selected specification of TLCD for parametric study	T (s)	Mass ratio (%)	Head loss coefficient (ξ)	With additional terms	Without additional terms
Head loss Coefficient	13.07	3.44	3.50	0.5807	0.5912
			5.50	0.6731	0.6605
			12.50	2.0409	2.0052
			55.00	6.1200	6.1458
Natural frequency (period)	13.07	3.44	55.00	6.1247	6.1132
	17.36			6.5431	6.6217
	26.42			9.5438	9.5914
TLCD/structure mass ratio	13.07	0.08	55.00	0.4031	0.4218
		1.2		3.7033	3.6502
		2.3		5.6701	5.6600
		6.49		7.7883	7.7741
		8.47		9.8447	9.8211
		10.72		19.7032	19.7255
		13.24		18.0207	18.0410
		16.02		15.4323	15.4412
		19.06		6.7105	6.734

4.4. Effect of rotational motion of platform on TLCD function

The effect of the rotational motion of the platform on TLCD function is determined using a numerical model without the θ-term in Eq.(2.13). The responses then are compared with those in which the rotational motion of the platform is taken into account (with θ-term in Eq. (2.13)). The motion reduction factors are compared in Fig. 24 with and without the θ-term. As seen, a 40% amplification is obtained for a mass ratio of 0.9% which is not a reasonable result. Increasing the mass ratio to 2% results in decreasing the platform motion rapidly by 50%. It is evident that the results are unreliable when the effect of platform rotation on TLCD is ignored; thus, it is necessary to consider the effect of the rotational motion of the platform on TLCD excitation.

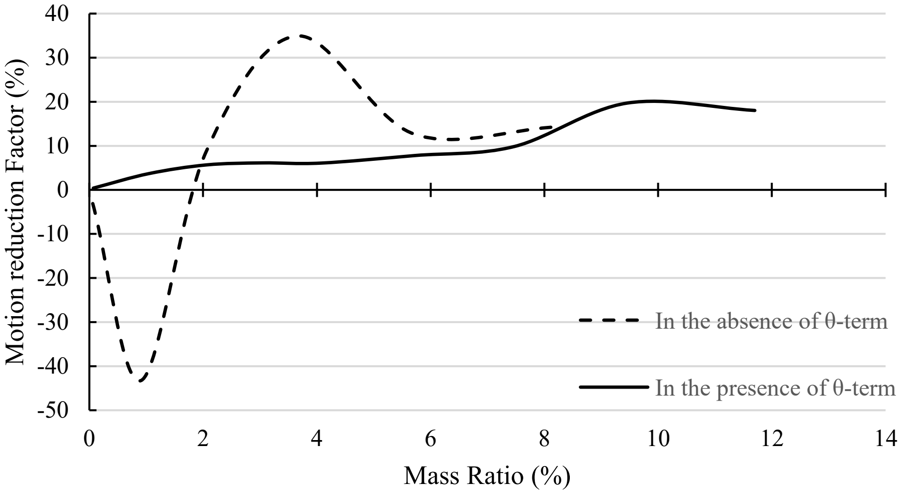

Fig. 25. TLCD mass ratio vs. motion reduction factor with and without *θ*-term.

5. Conclusions

A numerical study is carried out to investigate the effect of a tuned liquid column damper (TLCD) on the motion reduction of a semisubmersible platform. The simultaneous effect of the transitional and rotational motions of the platform on TLCD function are taken into account by deriving an appropriate formula. By time domain analysis method, linear and nonlinear wave forces as well as wave-frequency and low-frequency motions of the platform are examined in irregular waves.

It is shown that separate equations for pure transition and rotation could be applied to take into account the combined transitional and rotational effects of the liquid fluctuation in the TLCD. It is also found that the rotation of the platform affects TLCD function significantly.

This research also shows that only the low-frequency motion of a semisubmersible platform can be decreased with the use of a TLCD. A parametric study reveals that a value of 10% for the platform-damper mass ratio is optimal for the selected floating platform and increasing the blocking ratio of the damper orifice to 80% increases the efficiency of damper. It is also observed that, although the feasible frequency of the TLCD is far higher than the natural frequency of the semisubmersible, decreasing the damper frequency increases the efficiency.

6. References

1- G.F. Clauss, L. Birk, (1996), *Hydrodynamic shape optimization of large offshore structures*, Appl. Ocean Res., Vol.18, p.157–171.

2- M. Adjami, M. Shafieefar, (2008), *Hydrodynamic shape optimization of semi-submersibles using a genetic algorithm*, J. Mar. Sci. Technol., Vol.16, p.109–122.

3- J.Y. Lee, S.J. Lim, (2008), *Hull Form Optimization of a Tension-Leg Platform Based on Coupled Analysis*, Proc. Eighteenth Int. Offshore Polar Eng. Conf., Vol.8, p.100–107.

4- M. Muskulus, S. Schafhirt, (2014), *Design optimization of wind turbine support structures-A review*, J. Ocean Wind Energy, Vol.1, p.12–22.

5- M. Hall, B. Buckham, C. Crawford, (2014), *Hydrodynamics-based floating wind turbine support platform optimization: A basis function approach*, Renew. Energy, Vol.66, p.559–569.

6- M. Shafieefar, A. Rezvani, (2007), *Mooring optimization of floating platforms using a genetic algorithm*, Ocean Eng., Vol.34, p.1413–1421.

7- M. Mirzaei, (2014), *Mooring Pattern Optimization Using A Genetic Algorithm*, J. Teknol., Vol.2, p.189–193.

8- N. Ren, Y. Li, J. Ou, (2012), *The effect of additional mooring chains on the motion performance of a floating wind turbine with a tension leg platform*, Energies, Vol.5, p.1135–1149.

9- M. Brommundt, L. Krause, K. Merz, M. Muskulus, (2012), *Mooring system optimization for floating wind turbines using frequency domain analysis*, Energy Procedia, Vol.24, p.289–296.

10- R. Kandasamy, F. Cui, N. Townsend, C.C. Foo, J. Guo, A. Shenoi, Y. Xiong, (2016), *A review of vibration control methods for marine offshore structures*, Ocean Eng., Vol.127, p.279–297.

11- A. Di Matteo, A. Pirrotta, F. Lo Iacono, G. Navarra, (2012), *The Control Performance of TLCD and TMD : Experimental Investigation*, 5th Eur. Conf. Struct. Control, p.1–9.

12- H. Gao, K.C.S. Kwok, B. Samali, (1997), *Optimization of tuned liquid column dampers*, Eng. Struct., Vol.19, p.476–486.

13- A. Kareem, T. Kijewski, Y. Tamura, (2007), *Mitigation of Motion of Tall Buildings with*

Specific Examples of Recent Applications, Wind Struct., p.201–251.

14- B. Samali, K.C.S. Kwok, D. Tapner, Vibration control of structures by tuned liquid column dampers, in: Proc., IABSE, 14th Congr., 1992: pp. 461–466.

15- A. Ghosh, B. Basu, (2004), *Seismic vibration control of short period structures using the liquid column damper*, Eng. Struct., Vol.26, p.1905–1913.

16- T. Balendra, C.M. Wang, G. Rakesh, (1999), *Effectiveness of TLCD on various structural systems*, Eng. Struct., Vol.21, p.291–305.

17- C.C. Chang, (1999), *Mass dampers and their optimal designs for building vibration control*, Eng. Struct., Vol.21, p.454–463.

18- J.C. Wu, M.H. Shih, Y.Y. Lin, Y.C. Shen, (2005), *Design guidelines for tuned liquid column damper for structures responding to wind*, Eng. Struct., Vol.27, p.1893–1905.

19- H.H. Lee, S.H. Wong, R.S. Lee, (2006), *Response mitigation on the offshore floating platform system with tuned liquid column damper*, Ocean Eng., Vol.33, p.1118–1142.

20- F. Sakai, S. Takaeda, T. Tamaki, Tuned liquid column damper-new type device for suppression of building vibration, in: Int. Conf. High-Rise Build., 1989: pp. 926–31.

21- X. Zeng, Y. Yu, L. Zhang, Q. Liu, H. Wu, (2014), *A New Energy-Absorbing Device for Motion Suppression in Deep-Sea Floating Platforms*, Energies, Vol.8, p.111–132.

22- H.H. Lee, H.H. Juang, (2012), *Experimental study on the vibration mitigation of offshore tension leg platform system with UWTLCD*, Smart Struct. Syst., Vol.9, p.71–104.

23- C. Coudurier, O. Lepreux, N. Petit, (2018), *Modelling of a tuned liquid multi-column damper. Application to floating wind turbine for improved robustness against wave incidence*, Ocean Eng., Vol.165, p.277–292.

24- C. Holden, T. Perez, T.I. Fossen, (2011), *A Lagrangian approach to nonlinear modeling of anti-roll tanks*, Ocean Eng., Vol.38, p.341–359.

25- M. Shadman, A. Akbarpour, (2012), *OMAE2012-83330*, p.1–7.

26- M. Shahrabi, K. Bargi, (2019), *Enhancement the Fatigue Life of Floating Breakwater Mooring System Using Tuned Liquid Column Damper*, Lat. Am. J. Solids Struct., Vol.16,.

27- M.J. Hochrainer, (2005), *Tuned liquid column damper for structural control*, Acta Mech., Vol.175, p.57–76.

28- S.D. Xue, J.M. Ko, Y.L. Xu, (2000), *Tuned liquid column damper for suppressing pitching motion of structures*, Eng. Struct., Vol.22, p.1538–1551.

29- X. Suduo, J.M. Ko, Y.L. Xu, (2002), *Wind-induced vibration control of bridges using liquid column damper*, Vol.1, p.271–280.

30- A.A. Taflanidis, D.C. Angelides, G.C. Manos, (2005), *Optimal design and performance of liquid column mass dampers for rotational vibration control of structures under white noise excitation*, Eng. Struct., Vol.27, p.524–534.

31- H. Sabziyan, H. Ghassemi, F. Azarsina, S. Kazemi, (2014), *Effect of Mooring Lines Pattern in a Semi-submersible Platform at Surge and Sway Movements*, J. Ocean Res., Vol.2, p.17–22.

32- C.C. Chang, C.T. Hsu, (1998), *Control performance of liquid column vibration absorbers*, Eng. Struct., Vol.20, p.580–586.

33- G.F. Clauss, C.E. Schmittner, K. Stutz, (2002), *Time-domain investigation of a semisubmersible in rogue waves*, 21st Int. Conf. Offshore Mech. Arct. Eng.,.

34- N.M. Newmark, (1959), *A method of computation for structural dynamics*, J. Eng. Mech. Div., Vol.85, p.67–94.

35- M. López, F. Taveira-Pinto, P. Rosa-Santos, (2017), *Numerical modelling of the CECO wave energy converter*, Renew. Energy, Vol.113, p.202–210.

36- K.C. Subrata, S. Cliakrabarti, Handbook of offshore engineering, 2005.

37- ANSYS, Aqwa Theory Manual, 2013.

38- A.P.I. RP2A-WSD, Recommended practice for planning, designing and constructing fixed offshore platforms--working stress design--, 2014.

39- M. Keddam, (2002), *Offshore Hydromechanics*, Electrochim. Acta, Vol.47, p.1503–1504.

40- T. Chatterjee, S. Chakraborty, (2014), *Vibration mitigation of structures subjected to random wave forces by liquid column dampers*, Ocean Eng., Vol.87, p.151–161.

41- B. Li, K. Liu, G. Yan, J. Ou, (2011), *Hydrodynamic comparison of a semi-submersible, TLP, and Spar: Numerical study in the South China Sea environment*, J. Mar. Sci. Appl., Vol.10, p.306–314.

INTERNATIONAL JOURNAL OF
COASTAL & OFFSHORE ENGINEERING

IJCOE Vol.5/No. 2/Summer 2020 (41-49)

Available online at: www. Ijcoe.org

Predicting the sediment rate of Nakhilo Port using artificial intelligence

Mahdi Shafaghat[1], **Reza Dezvareh**[2*]

[1] *MSc student, Noshirvani University of Technology, Babol, iran; Mahdishafaghat1373@gmail.com*
[2*] *Assistant Professor, Faculty of Civil Engineering, Noshirvani University of Technology, Babol, iran; rdezvareh@nit.ac.ir*

ARTICLE INFO

Article History:
Received: 21 Oct. 2020
Accepted: 23 Dec. 2020

Keywords:
artificial intelligence
Long shore Sediment Transport
Support Vector Regression
Neural Network
Classification

ABSTRACT

In order to predict changes in coastal profile, it is necessary to investigate the sediment transport rate along the coast. Sediment transport is important in the areas of sedimentology, geomorphology, civil engineering and environmental engineering. The study of sediment transport is often performed to determine the location of erosion or deposition, the amount, timing and distance of its occurrence. Forecasting future coastline changes are as a result of the marine structural development. It provides the conditions for appropriate engineering decision-making. It also makes the grounds for sustainable use of the coast. When spot and local forecasts are necessary, models based on time series like support vector regression and Artificial Neural Network as new solutions are taken into consideration. These methods are one of the ways of machine learning. This study was investigated the importance of the offshore sediment transport rate in this research for the desired beach on the west coast of Hormozgan province. The littoral drift (LITDRIFT) model is used to get this type of transfer rate. To estimate evaluation of the longshore sediment transport rate by support vector machine (SVM); it will be needed two categories of data; one for data training and the other to check the machine for testing. The results of estimation of sediment transport rate using support vector regression and artificial neural network method showed the superiority of support vector regression over the neural network in both training and experimental groups of data.

1. Introduction

In coastal engineering, cross shore and longshore sediment transport rate must be calculated to determine shoreline changes. Sediment transport in the Sedimentology, Geomorphology, and Civil Engineering and Environmental Engineering fields are important. The study of sediment transport is often performed to determine the location of sediment deposition (erosion) or sedimentation, amount, time and distance of its event [1]. The instability of beaches and significant shoreline displacement, the erosion of beaches by waves, flows and storms have caused significant damages to offshore installations and structures. The filling the ponds of the ports from the sediments in a short time and similar matters, are among significant problems and difficulties of many countries and regions with maritime boundaries. Therefore, the sediment transfer is one of the most important processes associated with the above dilemmas that is being investigated [2]. Due to the vast shoreline borders in Iran and the existence of various coastal structures, determining the sediment transport rate on these coasts is of great importance. [3]. There is a state of sliding or skipping of the particles that so-called Bed Load transfer and the other which the particles move is in a suspended state that is called Suspended Load transfer, therefore the issue of sediment transport divided into two types: Bed Load and Suspended Load. For each particle of the precipitates, the current must reach the top of the critical incision. To move a particle of non-stick sediment; The fluid velocity must exceed the critical section velocity, when the particle size is very small or when the flow is very slow, the sediment particles are protected by slimy layers and thus there will be no movement. Following the increase in the flow, as the section velocity increases, the effect of this layer becomes lower, the coarsest grain begins to roll and bed load creates [4]. Mohandes et al. used the SVM to predict wind speed and compare its results with the multilayer perceptron (MLP) neural networks. They showed that SVM had better performance than MLP in their studies [5]. Bhattacharya and Solomatine conducted another study on the soil classification using three SVM, ANN and decision tree. in this study, the same results were obtained for all three models [6]. Singh et al. was used to estimate the separation efficiency due to sluice installation in the channels. They also made a comparison to ANN and SVM in their studies. Both of these methods worked in the same way. They also refer to less computational SVM than ANN [7]. The offshore sediment transport can be the result of the sand return to the swells and sinking's of the bay and along the coast. At the other times, there is a widespread displacement of sediment perpendicular to the shore, which will cause sand to move along the beach. Here the focus is on investigating and efficiency of models for predicting sediment transport along the coast [8]. Sediment transport is an evolving science that relies on complex processes. So this research seeks to improve and predict sediment transport rates in coastal areas using soft computing methods [9]. As can be seen, the rate of longshore sediment transport rate has not been predicted by SVM. On the other hand, since the support vector machine has different parameters, the innovation of this research and its distinguishing feature is that it has obtained the optimal values of these parameters for this field. It was estimated of sediment transport rate using support vector regression (SVR) and artificial neural network (ANN). Finally, the results showed a more accurate evaluation of SVR than ANN.

2. Soft Computing

2.1. Support Vector Machine (SVM)

Machine Learning is a scientific discipline that develops and regulates algorithms that according to them, computers can learn. These algorithms allow computers to evolve behavior using experimental data. The history of using machine learning methods in its modern form goes back to World War II (the 1950s) and the invention of modern computers. Machine learning methods, such as genetic algorithms and neural networks, emulated the body structure of alive creature and the human mind. An important breakthrough in machine learning approaches was the introduction of the SVM by Vapnik and his colleagues in the 90s. The support vector machine method has been developed based on the Vapnik statistical learning theory [10]. In SVM to improve model generalizability, Structural Risk Minimization Principles (SRM) is used. However, in other methods, Experimental Risk Minimization principles (ERM) are used. SRM principles have been shown to perform better than ERM [11]. The support vector machine generally is used in two-group or multi-group classification issues and regression. Another criterion in machine learning approaches is based on the type of data available for model development. Generally speaking, based on the kind of data that is used in machine learning the issues are categorized into several sections which are: Supervised Learning, Reinforcement Learning, Unsupervised Learning, Semi-supervised Learning.

2.2. SVM in Data Regression

In the support vector machine in solving the regression problem, the goal is to find a linear function such as $f(x) = (w.x) + b$ which can estimate output values based on input values. In SVM, the Vapnik losses function is used to solve the regression problem. In this losses function, a minimum error of ε is ignorable from the actual value. We define the losses function as follows:

$$L_{\varepsilon}(y) = |y - f(x)|_{\varepsilon} = \begin{cases} 0 & if \quad |y-f(x)| \leq \varepsilon \\ |y - f(x)| & \quad otherwise \end{cases} \tag{1}$$

Figure 1 shows the losses function well.

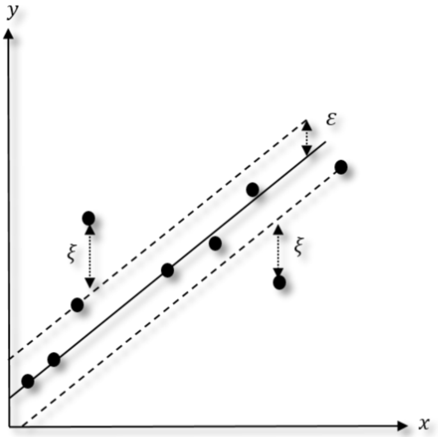

Figure 1. The Losses Function Error

Thus, if the predicted value within the strip is 2ε thick, the losses or harm is zero, but if not, the amount of losses is equal to the difference between the values predicted in ε.

In the learning machine approach to limit model errors, we use structural risk minimization principles. yet, other approaches such as artificial neural networks are on the basis of the principles of Experimental Risk Minimization. It was written the Experimental Risk function in terms of the non-sensible losses function to error ε as follows:

$$R_{emp}(w, b) = \frac{1}{l} \sum_{i=1}^{n} |y - f(x)|_{\varepsilon} \tag{2}$$

The Experimental Risk function is made up of test samples and if the training dataset is too large; (in other words, the larger the number of training samples) the experimental risk converges to the real risk. But if not, even obtaining a small amount of the experimental risk won't be a guarantee for being small model errors on the samples that it has not yet experienced, (in other words, there is no guarantee of good generalization to the experimental data). In the artificial neural networks to overcome the problem of inappropriate generalization, good architecture should be designed for the network. During the model training, the designed network minimizes the number of errors on training data. The designed network may work well on the test data and even bring the experimental risk to zero, but on the test data, it does not perform well. So, it was selected the appropriate structure which, besides to decrease errors on training data, has good generalization capability [12]. In the support vector machine method to overcome the above problem, minimizing risk is done by minimizing structural risk. In structural risk besides to experimental risk, another operation is defined as the VC dimension. Using the principles of structural risk minimization, it is possible to maximize generalization while minimizing experimental risk. (To maximize generalizability, the VC dimension should also be controlled.) Thus, irrespective of the mathematical basis, the principles of structural risk minimization have been shown, the best function to perform the regression operation on the support vector machine method is to decrease the following function:

Minimize

$$\Phi(w,\xi^*,\xi)=\frac{\|w\|^2}{2}+C\left(\sum\xi_i^*+\sum\xi\right) \tag{3}$$

Subject to

$$\begin{aligned} &y_i-[(w.x_i)+b]\le\varepsilon+\xi_i\\ &[(w.x_i)+b]-y_i\le\varepsilon+\xi_i^*\\ &\qquad\xi_i,\xi_i^*\ge 0\end{aligned} \tag{4}$$

In this relation, the variables of slack are ξ^*,ξ. (Figure 2).

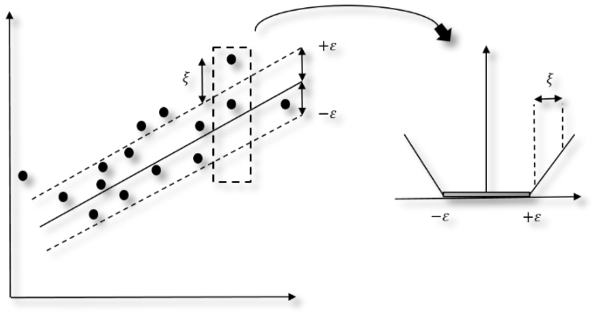

Figure 2. slack Variables

Before presenting the solution to the above optimization problem, it is recalled that, generally the basic foundations of regression in a support vector machine consist of the following three parts [13]:

- The support vector machine estimates a regression function by applying a linear function class.
- The support vector machine performs regression operations with the function that deviation from the actual value in it is less than ε.
- The support vector machine by minimizing structural risk offers the best response.

To solve the optimization problem, the previous relationship is used as its equal in the form of Lagrange function:

$$L(\alpha^*,\alpha)=-\varepsilon\sum_{i=1}^{n}(\alpha_i^*+\alpha_i)+\sum_{i=1}^{n}y_i(\alpha_i^*-\alpha_i)-\frac{1}{2}\sum_{i=1}^{n}\sum_{j=1}^{n}(\alpha_i^*-\alpha_i)(\alpha_j^*-\alpha_j)\,(x_i,x_j) \tag{5}$$

Where in this relation, the Lagrange coefficients areα^*,α

By maximizing the above function under the following amounts:

$$\alpha\begin{cases}\sum\alpha_i^*=\sum\alpha_i\\ 0\le\alpha_i^*\le C\\ 0\le\alpha_i\le C\end{cases}\qquad for\quad i=1,2,\dots,n \tag{6}$$

The α,α^* coefficients are calculated. Samples that do not have the corresponding lagrange coefficients are known as support vectors. These data than the measured value have a prediction error greater than $(\pm\varepsilon)$, therefore they do not fall into the regression model of intra-band support vectors $(\pm\varepsilon)$, thus the value of ε controls the number of support vectors [14].

Once the langrage coefficients are determined, the final answer will be calculated as follows:

$$w_0=\sum(\alpha_i^*-\alpha_i)x_i \tag{7}$$

$$\mathrm{f(x)}=\sum(\alpha_i^*-\alpha_i)(x_i-x)+b_0 \tag{8}$$

In the above relations, ε and C parameters defined by the user. If the uncertainties in the existing data (which may be due to reasons such as unavoidable measured errors and sample shortages occur within ranges of input variables) are great, the larger the value ε leads to a solution that is more independent of these uncertainties. But, very large values of ε leads to a situation where no correct prediction is possible because this will change the state of the support vectors and will affect the results. Although selecting large amounts of ε reduces the number of support vectors, and this reduction is desirable in support vectors (that is the thickness of out-of-band data is reduced to 2ε) but achieving this goal by widening the bandwidth to ε is wrong. If the value of ε is low, a large number of support vectors will be selected which will increase the number of being trained dangerous (That is, although the machine performs well on training samples, it has poor generalizability) [15 and 16]. According to the final answer of relationf(x), it is evident that data with zero Lagrange coefficients have no effect on the final response and only support vectors are used to obtain the regression function. We call his feature sparseness. Since support vectors have a relation with to this feature, it turns out that value ε also controls this feature of the support vector machine [17].

In the regression model, Kernel functions are also used to develop the nonlinear model. Yet various kernel functions have been introduced but it is very difficult to get kernel functions in general. It's mentioned two examples of important kernel functions used in engineering applications are:

- Polynomial Kernel function

$$K(x_i, x) = ((x, x_i) + 1)^d \tag{9}$$

In this relation, d is the degree of a polynomial and its value is defined by the user [18].

- Radial Basis Function (RBF)

$$K(x, x_i) = \exp\left(\frac{-|x-x_i|^2}{2\sigma^2}\right) \tag{10}$$

In this relation, σ is the width factor of Kernel function and is defined by the user [11].
In that case the answer through a process will be as follows:

$$f(x) = w_0.x + b_0 \tag{11}$$
$$w_0.x = \sum(\alpha_i^* - \alpha_i)K(x_i, x) \tag{12}$$
$$b_0 - \frac{1}{2}\sum(\alpha_i^* - \alpha_i)[K(x_r, x_i) + K(x_s, x_i)] \tag{13}$$

As it is evident, selecting the appropriate values for the parameters to be determined by the user forms a very important part of the design of the support vector machine model. The most common way to determine the model design parameters and the parameters of the kernel functions is to use the trial and error process.

2.3. Comparison of SVR and Neural Network

Artificial neural networks (ANNs) are one of the most common and well-known methods of machine learning. Given the widespread and successful use of this method in various engineering issues, a brief comparison between the two methods is presented in this section to better understand the capabilities of the support vector regression method. Given the general principles outlined in the different parts of this chapter, the differences between the two approaches can be illustrated in two important areas. First, because the SRM principles perform better than the ERM, so it is expected that the support vector regression that applies the SRM principles performs better than the artificial neural network that uses the ERM principles. Besides, because the SVR method deals with a convex optimization problem, achieving an overall minimum is guaranteed and there is no risk of stopping the model in the local minimum trap (unlike what exists in artificial neural networks) [19 and 20].

3. Model Used to Investigate Sediment Transport Rate

The accuracy (validity) of the LITDRIFT model available in the MIKE21 software which developed and marketed by DHI has been demonstrated by applying to numerous engineering and research projects and based on actual results as well as comparisons with analytical problems. It is a one-dimensional model and consists of two major parts: the hydrodynamic model and the sediment transport model [21]. The hydrodynamic model can calculate wave's refraction, depth reduction, waves breaking, radiation stress, wave setup, and coastal parallel currents velocity and the sediment transport model also calculates the sediment transport rate by taking into account the simultaneous effect of wave and current. Based on this model, and the theory, the presented relations are about how the current is layered to consider the effect of the simultaneous turbulence of wave and current [22]. In this theory, the depth is divided into two areas near the bed and outside the bed. The software calculates the characteristics of the waves at the breaking point, taking into account the phenomenon of refraction and shallow and wave transfer to shore. Since the depth at which the breaking occurs varies for each wave component, the software determines the depth of the breaking area for the different components of the waves. Then, by applying the appropriate formulas, the sediment transport for each wave and its resulting current is calculated. Finally, by adding sediments from different components of waves to each other, the transverse distribution of sediment transport from sea to coast is determined. It should be noted that the scope of application of the model used in sandy beaches, which is the major factor of waves sediment transport, has been defined. The one-dimensional LITDRIFT model is not used in the areas where the sediments are fine-grained and the equations governing the sand sediment transport is not true, or in areas where sediment transport agent is tidal currents, and due to the geographical location of this part of the beach, there are no significant waves. Because of the fine-grained of the sedimentary materials and is low the rate of collapse velocity of the aggregates and their permanent suspension, there was no major sediment deposition in these areas. so, no significant morphological changes can be identified [18,19].

3.1. The Area of Observation

In this study, longshore sediment transport rate investigates for one of shore of Hormozgan province. Also, it was showed position of the selected shore beach in the overview of Fig 3, as well as the position of the shore beach with details such as the selected buoy in Fig 4.
The details of the shore beach and the location of the buoy are presented in Table 1.

Table1. Details of the shore beach and the location of the buoy

Port	Shore beach	Station location	Measuring range
Nakhilo	W3	E53.375 N26.875	1999 to 2009

According to the historical data of the Ports and Maritime Organization recorded by the mentioned buoys can point out the wave height (Hs), wave angle (α), wave period (T), and particle size (∅).

The statistical characteristics of the recorded data and the investigated littoral sediment transport rate for the shore beach in question are presented in table 2.

The main objective of the present study is to estimate the longshore sediment transport rate, based on data from the Ports and Maritime Organization, using support vector regression. Thus, two categories of data are needed, one related to data training and the other for machine evaluation for testing. The basis of the support vector regression is the use of historical data collected from the studied system conditions. The more scope and variety of the collected data, the more adaptability and comprehensiveness can create. It will be presented the data in Table 2&3 as training and experimental data for using in the support vector machine.

Figure 3. Location of Nakhilo Port

Figure 4. Nakhilo Port

Table 2. Statistical Characteristics of Buoy

Variable	Educational dataset (29654 samples)			
	Minimum	maximum	average	standard deviation
Wave height (meter)	0.014	1.08	0.279	0.156
Wave angle (degree)	185.2	359.8	282.3	19.3
Wave period (second)	1.85	8.7	4.3	1.12
Particle size (m meters)	0.1	0.1	0.1	-
Sediment transport rate (Cubic meters per day)	0.012	5001.7	435.1	862.2

Table 3. Statistical Characteristics of Buoy

Variable	Experimental dataset (3295 samples)			
	Minimum	maximum	average	standard deviation
Wave height (meter)	0.021	0.855	0.277	0.156
Wave angle (degree)	186.8	357.2	282.18	19.14
Wave period (second)	1.85	7.85	4.29	1.11
Particle size (m meters)	0.1	0.1	0.1	-
Sediment transport rate (Cubic meters per day)	0.05	4998.25	432.57	873.29

4. Conclusion and Discussion

Data were collected from the LITDRIFT model as well as support vector regression. In this section, first, the outputs of the LITDRIFT model and then the results are presented to estimate the littoral sediment transport rate.

4.1. Sedimentary Studies

The position of the desired shore beach has examined and the wave climate introduced and finally, by implementing and calibrating the one-dimensional sediment transport model, an estimate of sediment transport rate values was obtained. The computational values applicable along the selected shore beach will be applicable in areas where the coastal line and conditions have a good similarity with specifications of the model calibration location.

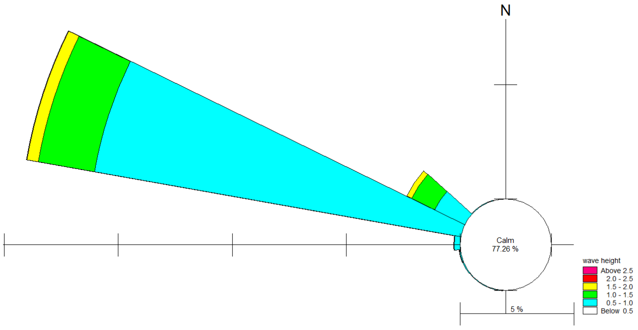

Figure 5. A ten-meter-deep flower wave of shore beach

4.2. Wave Climatic of West Shore Beach

In order to investigate the wave conditions in the studied shore beach, a flower wave with a depth of 10 m was extracted in the upper area of Nakhilo port as shown in Figure 5. Examination of the rose wave of shore beach shows that in the studied range about 77% of the days, the wave height is less than 0.5 m (calm conditions). The Geographic direction of most waves is from the northwest.

4.3. Model Calibration

Based on the software guide suggested for calculating bed roughness, the following relation can be used:

$$Roughness = 2.5 \, . \, d_{50}$$

d_{50} is particle diameter representing the 50% cumulative percentile value (50% of the particles in the sediment sample are finer than the d50 grain size). But, according to this reference, the above value is not constant and definite and this parameter is one of the most important parameters of the model calibration. Based on the available morphological evidence, one-dimensional mathematical model calibration is considered.

To account for variable grain size and the diameter of sediment particles as one of the effective parameters in calculating the sediment transport rate, in this paper, field data obtained by sediment traps are used.

4.4. LITDRIFT Model Outputs

By implementing the LITDRIFT model, the sediment transport rate in the study area is calculated. The result is shown in Figure 6 as a directional distribution of sediment.

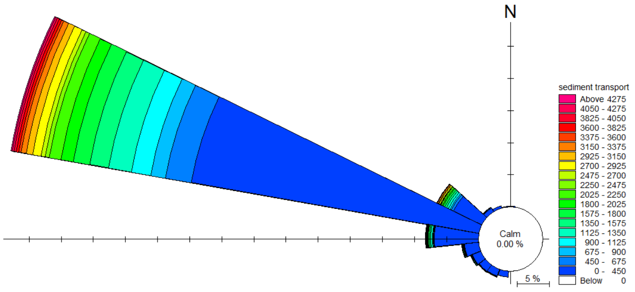

Figure 6. Directional distribution of sediment (cubic meters per year) in the shore beach

5. Support Vector Regression Results

Support vector regression is used to predict and estimate the longshore sediment transport rate. According to the performance of kernel functions and the description provided in the "SVM in data regression" section; The RBF kernel function is used to predict the sediment transfer rate by this machine and the optimal coefficients obtained by trial and error are equal to C = 9 and σ = 0.28.

To compare and confirm the results obtained by the support vector regression, the values of this machine were compared with the actual sediment transport rate extracted from the Ports and Maritime Organization. Also, ANN is used to compare the support vector regression with another soft computation.

MATLAB software has been used to model coastal sediment transport rates using a multilayer perceptron neural network model. And it was comparing the results of this model with SVR and actual observations. First, the neural network scatter diagram in two training and experiment modes is shown in Figure 7.

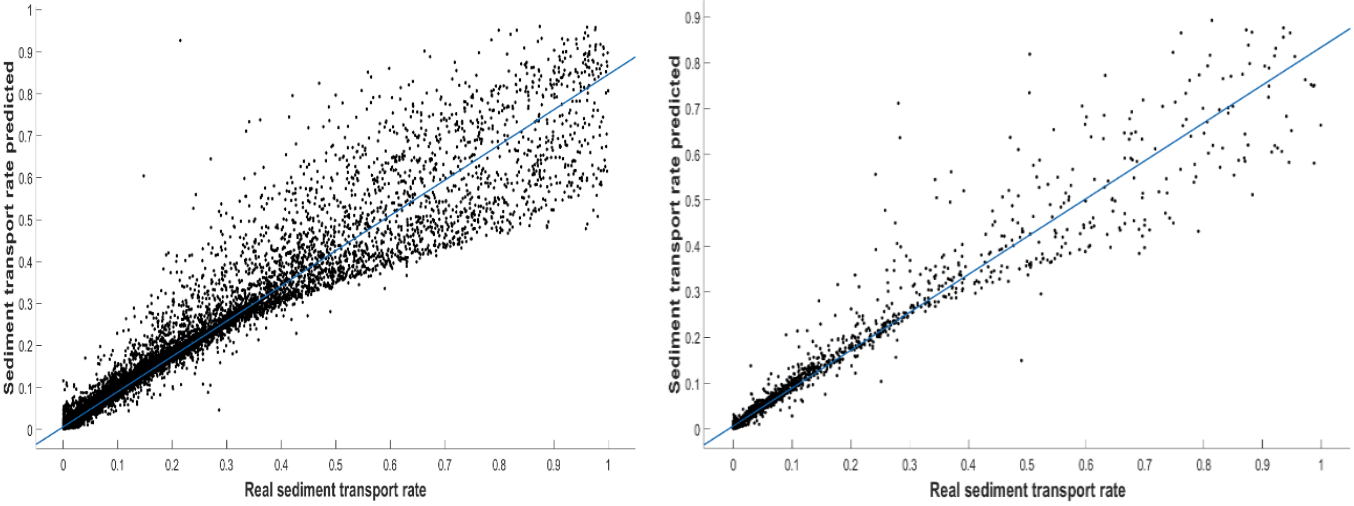

Figure 7. Scatter diagram of real sediment transport rate relative to the values predicted by ANN in training and experiment mode

The scatter diagram of the support vector regression is presented in two training and experiment modes in Figure 8.

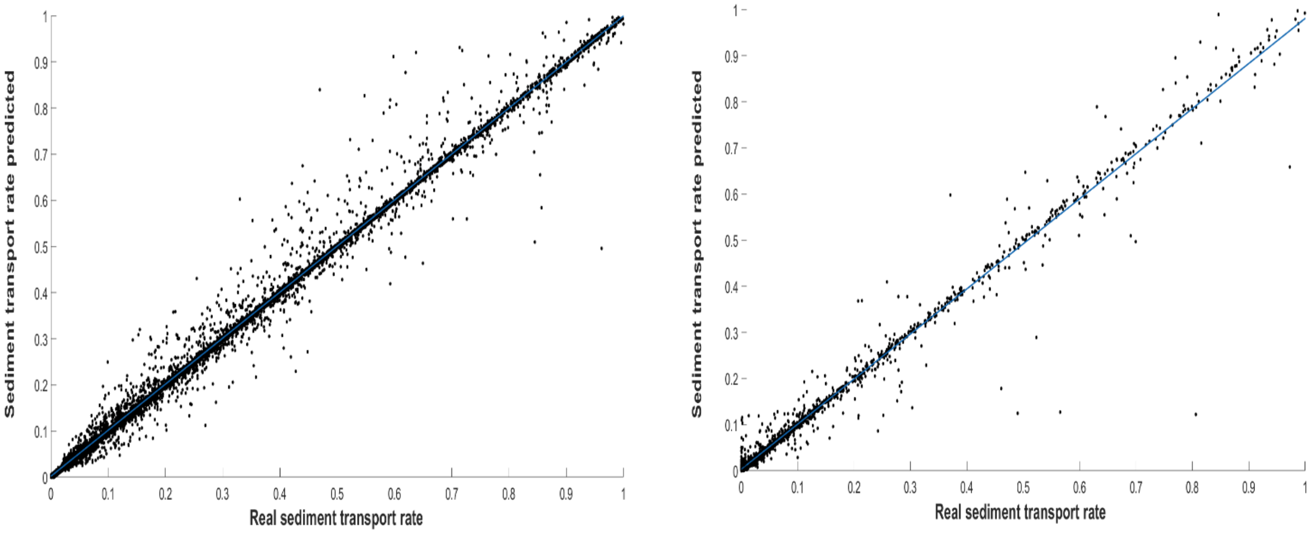

Figure 8. Scatter diagram of the actual sediment transport rate relative to the values predicted by SVR in training and experiment mode

The results of Figures 7 and 8 show the proper fit of the support vector regression than the neural network in predicting the sediment transport rate. Statistical estimations have also been used to investigate more accurately. Detection coefficient (R^2) and root mean square error (RMSE) was used to evaluate the accuracy of littoral sediment transport rate estimation through SVR and ANN. Statistical estimates are presented in Tables 4 and 5 for the two training and experiment modes.

Table 4. Statistical estimation of predicted sediment transport rate in training mode

Statistical estimation Method	R^2	RMSE
SVR	0.99	0.012
ANN	0.94	0.034

Table 5. Statistical estimation of predicted sediment transport rate in experiment mode

Statistical estimation Method	R^2	RMSE
SVR	0.98	0.024
ANN	0.94	0.035

It can clear that in training mode, the detection coefficient of the support vector regression method is more accurate than the neural network in estimating longshore sediment transport rate and also has the least root mean square error.

In the experimental mode, the coefficient $\boldsymbol{R^2}$ and RMSE for both SVR and ANN methods show high accuracy of the support vector regression using RBF kernel over artificial neural network.

The Figures 9 and 10 show predictions made by two soft computing methods (SVR and ANN) by comparing the actual values of the longshore sediment transport rate in a bar graph.

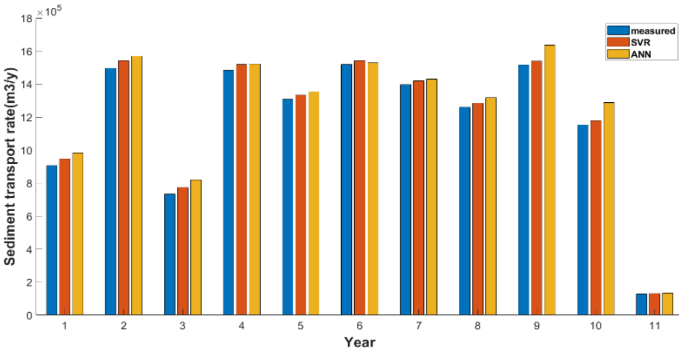

Figure 9. Comparison of 11-year littoral sediment transport rate for training data

In Fig 9, it will be examined the littoral sediment transport rate for 11 years in the training mode. It was compared the results of training from SVR and ANN models with the measured values. The results show a good performance of SVR with RBF kernel function than the ANN ratio. It is evident that the values predicted by the SVR are closer to the actual values. Also the ANN method has predicted higher values over most years than the actual values.

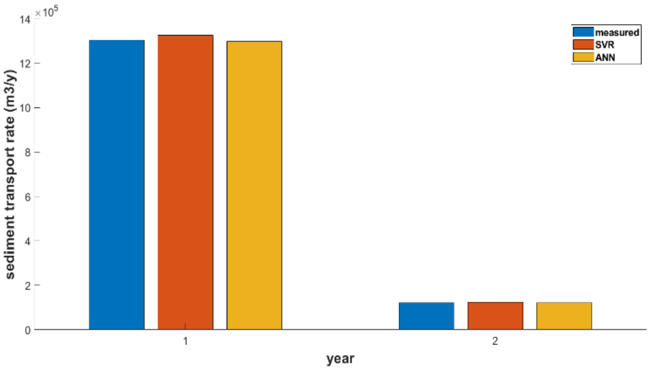

Figure 10. Comparison of 2-year littoral sediment transport rate for the experimental data

It is obvious in Fig 10 that in the experimental mode, as in training mode, the values predicted by the support vector regression are close to the actual values. Also, the values predicted by the ANN show higher values than the real values.

6. Conclusion

This study was divided sediment studies (Sedimentology) into training and experimental groups. It was aimed at identifying sedimentary behavior of one of the shore beaches of Hormozgan province, sediment-prone areas and areas subject to erosion and data. By using vector support regression and kernel RBF function and artificial neural network, this paper was predicted the parallel littoral sediment transport rate. The results of the classification showed better performance of RBF kernel in the support vector regression than the neural network in predicting coastal parallel sediment transport rate. The accuracy of the RBF kernel in training and testing mode was 99% and 98%, respectively, which was about 4% more accurate than the neural network results.

To predict coastal profile changes, it is necessary to investigate the rate of littoral sediment transport along the parallel direction of the coast. The sediment transport rate along the parallel the direction of coast is effective in estimating the rate of sedimentation, descaling, and deformation of the coastal profile. For sediment management in coastal areas, the sediment transport process as well as the morphological changes, the design of protective structures against descaling (erosion) as well as analysis of sedimentation status at the craters of breakwaters and ports are of great importance. Understanding sediment behavior and predicting future shoreline changes can help coastal engineering and management decisions.

As mentioned earlier, the present study led to the presentation of a method based on soft calculations in estimating sediment transport rates, which can be used in real projects from two perspectives: First, the use of soft computing methods to estimate phenomena such as sediment transport, which on the one hand has many uncertainties and on the other hand has little data, can lead to better estimates of the actual projects. Secondly, support vector machine method has a higher response rate than conventional methods of soft computing such as neural network, which will reduce the cost and time of analysis of the coastal engineering projects.

7. Acknowledgment

The author acknowledges the funding support of Babol Noshirvani University of Technology through Grant program No. BNUT/394097/99.

8. References

1- Leeder, M. R. (2009). *Sedimentology and sedimentary basins:* from turbulence to tectonics. John Wiley & Sons.

2- Dezvareh, R. (2019). *Providing a new approach for estimation of wave set-up in Iran coasts*. Research in marine sciences, 4(1), 438-448.

3- Van Rijn, L. C. (1993). *Principles of sediment transport in rivers, estuaries and coastal seas* (Vol. 1006, pp. 11-3). Amsterdam: Aqua publications.

4- Mangor, K. (2004). *Shoreline management guidelines.*

5- Mohandes, M. A., Halawani, T. O., Rehman, S., & Hussain, A. A. (2004). Support vector machines for wind speed prediction. Renewable energy, 29(6), 939-947.

6- Bhattacharya, B., & Solomatine, D. P. (2006). *Machine learning in soil classification*. Neural networks, 19(2), 186-195.

7- Singh, K. K., Pal, M., Ojha, C. S. P., & Singh, V. P. (2008). *Estimation of removal efficiency for settling basins using neural networks and support vector machines*. Journal of Hydrologic Engineering, 13(3), 146-155.

8- Akbarinasab, M., & Paeen Afrakoti, I. (2019). *Application of Soft Computing in Forecasting wave height (Case study: Anzali)*. International Journal of Coastal and Offshore Engineering, 3(1), 31-40.

9- Dezvareh, R. (2019). *Application of Soft Computing in the Design and Optimization of Tuned Liquid Column–Gas Damper for Use in Offshore Wind Turbines.* International Journal of Coastal and Offshore Engineering, 2(4), 47-57.

10- Vapnik, V. (1995). *The nature of statistical learning theory*. New York: Springer-Verlag.

11- Vapnik, V. N. (1999). *Statistical Learning Theory*. John Wiley & Sons, Inc

Kraus, N. C., & Dean, J. L. (1987). *Longshore sediment transport rate distributions measured by trap*. In Coastal sediments (pp. 881-896). ASCE.

12- Kumar, V. S., Anand, N. M., Chandramohan, P., & Naik, G. N. (2003). *Longshore sediment transport rate—measurement and estimation, central west coast of India*. Coastal Engineering, 48(2), 95-109.

13- Dezvareh, R., Bargi, K., & Moradi, Y. (2012). *Assessment of Wave Diffraction behind the Breakwater Using Mild Slope and Boussinesq Theories*. International Journal of Computer Applications in Engineering Sciences, 2(2).

14- Samui, P. (2008). *Support vector machine applied to settlement of shallow foundations on cohesionless soils*. Computers and Geotechnics, 35(3), 419-427.

15- Samui, P., Sitharam, T. G., & Kurup, P. U. (2008). *OCR prediction using support vector machine based on piezocone data*. Journal of Geotechnical and GeoEnvironmental engineering, 134(6), 894-898.

16- Dezvareh, R. (2020). *Upgrading the Seismic Capacity of Pile-Supported Wharfs Using Semi-Active Liquid Column Gas Damper*. Journal of Applied and Computational Mechanics, 6(1), 112-124.

17- Das, S. K., Samui, P., Sabat, A. K., & Sitharam, T. G. (2010). *Prediction of swelling pressure of soil using artificial intelligence techniques*. Environmental Earth Sciences, 61(2), 393-403.

18- Cristianini, N., & Shawe-Taylor, J. (2000). *An introduction to support vector machines and other kernel-based learning methods*. Cambridge university press.

19- Dezvareh, R. (2019). *Evaluation of turbulence on the dynamics of monopile offshore wind turbine under the wave and wind excitations*. Journal of Applied and Computational Mechanics, *5*(4), 704-716.

20- Hashemi, M. R., Ghadampour, Z., & Neill, S. P. (2010). *Using an artificial neural network to model seasonal changes in beach profiles.* Ocean Engineering, 37(14-15), 1345-1356.

21- Singh, A. K., Deo, M. C., & Sanil Kumar, V. (2007, September). *Neural network–genetic programming for sediment transport*. In Proceedings of the Institution of Civil Engineers-Maritime Engineering (Vol. 160, No. 3, pp. 113-119). Thomas Telford Ltd.

INTERNATIONAL JOURNAL OF
COASTAL & OFFSHORE ENGINEERING

IJCOE Vol.5/No. 2/Summer 2020 (51-64)

Available online at: www. Ijcoe.org

Shoreline change analysis along the coast of Bandar Abbas city, Iran using remote sensing images

Danial Ghaderi[1], **Maryam Rahbani***[2]

[1] *Ph.D. Candidate, Faculty of Marine Science and Technology, University of Hormozgan, Bandar Abbas 79131, Iran*
[2*] *Associate Professor, Faculty of Marine Science and Technology, University of Hormozgan, Bandar Abbas 79131, Iran*

ARTICLE INFO

Article History:
Received: 06 Nov. 2020
Accepted: 23 Dec. 2020

Keywords:
Bandar Abbas
Rate of Shoreline Change
Satellite Images
Remote sensing
Landsat
Sentinel

ABSTRACT

Coastal cities are among the most important and sensitive regions in the world. They are constantly affected by marine and coastal processes such as waves, currents, and other geological-physical parameters such as sedimentation and deposition. These factors constantly change the shoreline. Thus, evaluation and management at coastal area are very important. In this study, the rate of shoreline changes in the coastal area of Bandar Abbas, south of Iran, was investigated using remote sensing technique and DSAS tools. Landsat 8, 7 and, 5 satellite and Sentinel-2A satellite images were used to detect the rate of changes. Images from the years 1990 to 2020 were selected with 5-year time-interval. Using the NSM, SCE, EPR, and LRR statistical indexes of the DSAS tool, erosion and accretion rates were calculated in about 50 km of shoreline length. According to the EPR index Nakhl e Nakhoda jetty and Shoor River estuary show the maximum and minimum rate of changes, with amount of +31.07 m/yr and +4.83 m/yr, respectively. The average rate of changes was calculated as +12.34 m/yr. We recognized this part of the shoreline as the most sensitive area and suggested that any further development in this area should be undertaken obsessively. Shoreline of urban area of Bandar Abbas generally shows positive rate of change less than +5 m/yr, with the average rate of +2.35 m/yr, which suggests development in this area is in slow pace. In general, only 4% of the shoreline of is detected with high accretion (20.5 to 31.5 m/year) and about 53% is recognized as low accretion (0.5 to 10.5 m/year).

1. Introduction

Coastal cities are among the most important and sensitive regions in the world. They are constantly affected by marine and coastal processes such as wave, wind, longshore current, and tide [1], [2]. Besides, geological-physical factors also affect shorelines, which includes but not limited to activities such as constricting sea walls and breakwaters, artificial advancements and retreatments. These activities can alter geological-physical factors, which leads to massive erosion and/or accretion in the shoreline [3]. Since coastal areas always play significant role in humans' residency and activity, city developments are continually toward coastal areas, while it guaranties easy ocean transportation, accessibility to edible products especially seafoods [4]. Globally, about 45 to 60% of the world's population are residents in coastal areas [5]. Therefore, evaluation and management at coastal area are of vital importance, in order to recognize and take care of these vulnerable areas.

The coast of Bandar Abbas, located in the south of Iran and north of the Strait of Hormuz, is the largest port city in Iran, which includes commercial and passenger port. Bandar Abbas is among cities under major development, so it is of importance to study the coastal processes and the side effects of such development on the shorelines. In the present study, using the remote sensing technique, the shoreline changes of Bandar Abbas have been studied. Based on literatures by previous researchers, who applied remote sensing technique, the shoreline from 1990, 1995, 2000, 2005, 2010, 2015, and 2020 was extracted using Landsat and Sentinel satellite images. Blodget et al. used Landsat multispectral scanner (MSS) image data to examine Rosetta Promontory shoreline changes in the Nile Delta, Egypt. They stated that Landsat TM data of 30 m and SPOT data of 10 m resolution are useful for monitoring rapidly changes in shorelines [6]. Shoreline extraction using satellite images were applied by Do et al., [7] as a low-cost alternative in compare with the traditional methods. Using satellite-derived shorelines (Landsat), they estimated the rate of change in shorelines and in the volumes of coastal sediments in the North-Holland coast. They reckoned that using Landsat images is a suitable method to monitor shoreline change and coastal volume change over the decades in the North-Holland coast. Mitri et al. investigated mapping shoreline changes in Lebanese shoreline using Landsat 8 and Sentinel-2A satellite imagery. They concluded that the combination of Landsat-Sentinel-2 imagery can generate reliable data records for continuous monitoring of shoreline changes [8]. Novellino et al. used satellite imagery to investigate the shoreline changes associated with volcanic activity in 2018–2019 at Anak Krakatau, Indonesia [9]. They analyzed and validated shoreline changes through the adaptation of an existing methodology based on Sentinel-2 multispectral imagery which has been developed on Google Earth Engine. Using satellite imagery of Landsat 5, 7, and Sentinel 2A Muskananfola et al. examined shoreline changes in the Sayung coast over a 24-year period from 1994 to 2018 [4]. They used Digital Shoreline Analysis System (DSAS) to calculate and statistically analyze erosion and accretion rates of the coastline. Tamassoki et al. studied the shoreline changes in Bandar Abbas using Landsat TM-5 sensor data from 1984, 1998, and 2009 using the Max Likelihood Classification method [10]. They calculated the extent of the shoreline advancement (in hectares) and the shoreline length (in km) for each time interval and compared them. Their results showed that whenever coastline advancement occurs, the changes in shoreline length is ignorable. Ghaderi and Rahbani estimated the amount of shoreline change in the Beris Port - east of Chabahar, Iran, using remote sensing technique and DSAS tools. They used Landsat 8 and 5 satellite images to detect shoreline change, due to the port's construction date, satellite imagery of 1988, 1990, 2014, and 2019 [11].

2. Methods

2.1. Study area

Bandar Abbas, a coastal city in Hormozgan Province, is located in south of Iran, near the Strait of Hormuz in shoreline of Persian Gulf. Bandar Abbas occupies a land area of approximately 100 km^2, between latitudes 27°8' N and 27°15' N and longitudes 56°13' and 56°22' [12], [13]. According to the latest census, the population of Bandar Abbas is 680,366 [14]. Since the Shorelines of this city has been subjected to vast development in recent decades, it has been chosen for monitoring in this study (Figure 1). The shoreline of this city is about 50 km long. This coastal area holds subareas with industrial, economic, municipal, and tourism activities. Bandar Abbas the largest port city in Iran is an important center of economic and commercial activities [12], thus its sustainable management is of great importance [15], [16].

The shoreline under study includes the urban area and the economic zone. For instance, Shahid Haqqani Port, which is located in the city center of Bandar Abbas, is Iran’s biggest maritime passenger port with a capacity of transporting up to 14,000,000 passengers annually [17]. Also, Shahid Rajaee Port Complex, Iran's largest commercial port, is situated in the west of this city, 20 km far from the center, at the head of Hormuz Strait, and on the north side of Qeshm Island. [18], [19]. Another important commercial port is the port of Shahid Bahonar, which is located in 27° 08 N 56° 12’ E, in the north of Qeshm Island at the entrance of the Persian Gulf [17]. Other marine structures in this shoreline include Nakhl e Nakhoda jetty (east of the study area), Poshte shahr fishing port (west of Shahid Haqqani port) and marine structures related to the Thermal Power Plant of Bandar Abbas and the Special Industrial Zone Company of the Persian Gulf Mining and Processing Industry (between Shahid Bahonar port and Shahid Rajaee Port). In addition to marine structures, there are water inlets in this shoreline, which include; Shoor River estuary east side of Nakhl e Nakhoda jetty, with the peak discharge flood of about 43.39 m/s, Khore Shilat east side of Shahid Haqqani port, with peak discharge flood of approximately 19.92 m/s, Gorsouzan estuary east side of Shahid Haqqani port close to a small marine structure called Nimdayere, with peak discharge flood of approximately 43.39 m/s, and Khor Soro east side of Shahid Bahonar port, with the peak discharge flood of approximately 46.1 m/s [20].

The annual precipitation of Bandar Abbas is 210.6mm and the relative humidity is 56.6%. The average of the highest and lowest annual temperatures are 32.1 and 21.8 ° C respectively. The geological structure of the area is predominantly quaternary sediments that include Sadich (conglomerate) and Minab (fine silt and sand) formations [20]. Coastal areas of Bandar Abbas in the southwest, south and southeast districts, located in a low-lying area with elevations of less than 5 m. Due to the geographical location of Bandar Abbas, the shoreline of this city can be affected by factors such as tidal activity, wave set-up, wind set-up, and storm surges along the Persian Gulf and Oman Sea [12]. The tidal range is between 0.1 and 3.88 m, and the mean water temperature is 29 ± 1 °C [21].

The maximum and minimum wind speeds in Bandar Abbas are reported as 4.3 m/s and 0.1 m/s, respectively [22]. The predominant wind direction in Bandar Abbas is southerly, with probability of 31%. Southerly winds are prevailed during a year. However, at the beginning of the autumn, the frequency of occurrence of these winds decreases, and westerly winds become dominant. In winter, the wind blows most frequently from the west. On the north coast of the Persian Gulf, as on Bandar Abbas south coast, the dominant phenomenon is sea and land breeze. The lowest average wind speed in Bandar Abbas is 1.8 m/s. The location of islands such as Qeshm, Lark, and Hormoz near Bandar Abbas prevents both the formation of strong winds and the development of the sea and land breeze. According to Bordbar et al., [23] wind speed between 0.5 and 2.1 m/s is the most obvious meteorological feature of Bandar Abbas with probability of about 50%.

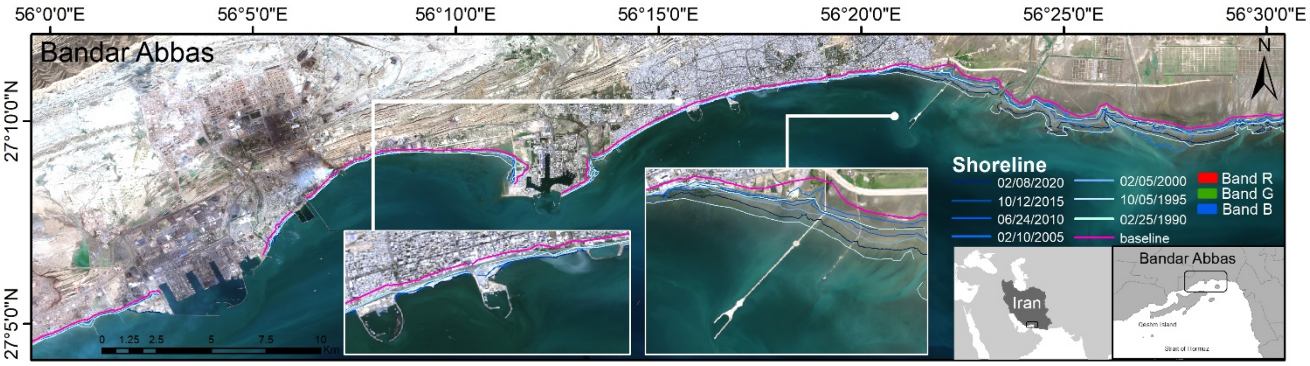

Figure 1 The geographical location of Bandar Abbas, satellite image (RGB) with some of the structures built on the shoreline.

2.2. Data collection and image processing

To monitor shoreline change, satellite images from Landsat 5, Landsat 7, Landsat 8, and Sentinel 2-A were used. Data collection of satellite imagery includes every five years images from 1990 to 2020. Detailed information of satellite images is summarized in Table 1. Two major limitations exist for choosing satellite imagery, namely cloud coverage conditions and water level. Taking into account these two limitations, proper date and time for satellite images were selected which are recorded in Table 1. High Water Level (HWL) is used as the most common shoreline indicator [24]. The average water level in all products is 1.1 m (Table 1). According to Table 1 the maximum HWL in the study area is up to 1.3 m. Considering the water level limitation, we confirm that all seven products are suitable.

Determining shorelines with remote sensing technique consists of two stages of preprocessing and postprocessing. In the preprocessing phase, several corrections must be made according to different satellite products. Satellite products of Landsat 5, 7, and 8 were georeferenced to UTM/WGS84 projection. Radiometric and atmospheric correction includes subtraction of the atmospheric contribution, reduction of illumination, viewing angles, and terrain effects, and sensor calibration [11], [25], [26]. These steps are performed using tools in ENVI 5.3 software [7], [26], [27]. Landsat imagery (Table 1) were acquired from the Earth Explorer database of the U.S. Geological Survey [28]. Table 2 shows the information of Landsat 5, 7, and 8 Bands. The resolution of TM, ETM+ and OLI sensors is 30m [7]. In addition to Landsat imagery, Sentinel-2A Level-1C data for 2020 are used. Sentinel-2A satellite has an MSI sensor that measures the Earth's reflected radiance in 13 spectral bands from visible to VNIR and SWIR, with a spatial resolution of 10, 20 and 60 m [29]. The mission of Sentinel-2A is to get optimized images for studying on vegetation, urban planning, terrestrial ecosystems and inland waters [30]. Images used in this study are collected from the Copernicus Open Access Hub of the ESA and the dataset consists of Sentinel-2A product level-1C imagery [31]. Software SNAP version 7.0 is used for image processing [32]. Level-1C is produced by radiometric and geometric corrections, including ortho-rectification and spatial registration on a global reference system with sub-pixel accuracy. This product, which is composed of 100 km × 100 km, tiles in the UTM/WGS84 projection and provides the Top-Of-Atmosphere (TOA) reflectance [33].

Sentinel-2 level-1C imagery should be corrected according to the bottom of the atmospheric layer (BOA). Several algorithms for atmospheric correction of Sentinel-2 products are available and can be used depending on the type of study area. ACOLITE is a processor for coastal and inland waters developed by the MUMM of the North Sea in Belgium [34]. Sen2Cor processor is designed for vegetation and land but provides good results in eutrophic waters [30], [35]. C2RCC processor is used along with the coastal atmospheres to parameterize radiative transfer models for the atmosphere over the water body [36]. iCOR processor is a generic scene and sensor atmospheric correction algorithm for land and water targets [37] and Polymer processor is an atmospheric correction algorithm for processing oceanic waters with and without the presence of sunglint [34]. According to a study of Pereira-Sandoval et al, [34], the C2RCC algorithm provides acceptable result. Besides, in SNAP version 7.0, this process is available for sentinel-2 products.

Table 1: Data images information employed in this study

Year	Satellite	Date	Local Time	Water Level (m)	High Tide/Time	Low Tide/ Time	Moon Phase
1990	Landsat _5	02/25/1990	9:36	1.2	1.6 / 23:14	-1.6 / 17:08	New Moon
1995	Landsat _5	10/05/1995	9:16	1	1.2 / 08:20	-1.2 / 01:51	90% Waxing
2000	Landsat _5	02/05/2000	9:49	1.1	1.3 / 23:29	-1.6 / 17:17	New Moon
2005	Landsat _7	02/10/2005	10:05	1.1	1.5 / 11:34	-2.0 / 18:12	5% Waxing
2010	Landsat _5	06/24/2010	10:06	1	1.1 / 22:00	-1.6 / 04:06	97% Waxing
2015	Landsat _8	10/12/2015	10:15	1.2	1.3 / 22:41	-1.4 / 16:41	0% Waxing
2020	Sentinel-2A	02/08/2020	10:20	1.2	1.4 / 22:52	-1.8 / 16:29	99% Waxing

According to previous studies [37, 38], it is necessary to conduct radiometric calibration and to apply atmospheric correction before extracting the shoreline position. Satellite images of Landsat 5, 7, 8, and Sentinel-2A are prepared using Envi v5.3 and SNAP v7.0. These images then converted to two-class segmentation, which means to determine the shoreline position, the water and land should be identified and recognized from each other. Several methods are available for shoreline detection using satellite imagery, which includes the Normalized Difference Vegetation Index (NDVI) [40], the Normalized Difference Water Index (NDWI) [41], the Modified Normalized Difference Water Index (MNDWI) [42], and the Automated Water Extraction Index (AWEI) [43]. The NDWI index has been used (Equation 1) in this study to determine the maximum difference between water and land.

$$NDWI = \frac{B_{GREEN} - B_{NIR}}{B_{GREEN} + B_{NIR}} \tag{1}$$

where, B_{Green} is the green band (Landsat TM/ETM+ band 2, and Landsat OLI and Sentinel-2A band 3), and B_{NIR} is the near infrared band (Landsat TM/ ETM+ band 4, Landsat OLI band 5 and Sentinel-2A MSI band 8). The central wavelength of band 2 of TM, ETM+, OLI and MSI sensors is 0.560 µm. The central wavelengths of band 4 of TM and ETM+ sensors are 0.830 µm and 0.835 µm, respectively. The central wavelength of band 5 of the OLI sensor is 0.865 µm and band 8 of the MSI sensor is 0.842 µm (Table 2). The NDWI index operates in such a way that maximize the reflectance of water using green wave lengths, minimize the low reflectance of NIR by water features and take advantage of the high reflectance of NIR by vegetation and soil features. As a result, water features gain positive and enhanced values, while vegetation and soil features usually gain zero or negative values [7], [41]. According to Figure 2, the positive values obtained from the NDWI index represent the water features and the negative values include the non- water features.

Table 2: information of Bands

Satellite	Sensor	Band used	Central wavelength (µm)	Pixel Resolution (m)
LANDSAT_5	TM	B2, B4	0.560, 0.830	30
LANDSAT_5	TM	B2, B4	0.560, 0.830	30
LANDSAT_5	TM	B2, B4	0.560, 0.830	30
LANDSAT_7	ETM+	B2, B4	0.560, 0.835	30
LANDSAT_5	TM	B2, B4	0.560, 0.830	30
LANDSAT_8	OLI	B3, B5	0.560, 0.865	30
Sentinel-2A	MSI	B3, B8	0.560, 0.842	10

2.3. Shoreline extraction and analysis

After applying the NDWI index, the distinction between water and land features is distinguishable, because the NDWI values have a bimodal distribution due to the distinct spectral characteristics of the two features types. The histogram of NDWI for 2020 is shown in Figure 2. When the water and land are distinguished the next step is clustering. The shoreline extraction from the bimodal distribution image was performed using an unsupervised classification approach by K-Means. K-means is one of the widely used clustering methods for analyzing features in images [44] and is the most popular clustering algorithm [45], [46]. This algorithm is one of the basic clustering techniques which is used in many data mining applications [47]. K-means, aiming to minimize cluster performance index, square-error and error criterion, are foundations of this algorithm. To seek the optimizing outcome, this algorithm searches for a K division to satisfy a certain criterion. K-means algorithm is a cluster algorithm and has advantages of briefness, efficiency, and celerity [48]. This method is an error minimization algorithm where the function to minimize is the sum of squared error (2):

$$e^2(K) = \sum_{k=1}^{K} \sum_{i \in C_k} (x_i - c_k)^2 \tag{2}$$

In equation 2 c_k is the centroid of cluster and c_k and K are known numbers in clusters. Two factors have made the K-means popular; the first is that it has linear time complexity and the second is that its implementation is easy [46].

The k-means method with 30 iteration and random seed of 31,415 by 2 clusters is employed, using SNAP (these values are considered as default in K-means algorithm in SNAP and are also suggested by previous literatures [49]). Figure 2 shows the clustering result with the k-means method. The resulting image consists of two clusters: water (1) and land (0). Afterwards, using ArcMap, the raster image from the clustering is converted to polygons and lines. Figure 3 shows the shoreline extraction steps as an instance. Finally, the shorelines are extracted for all mentioned years (1990, 1995, 2000, 2005, 2010, 2015 and 2020).

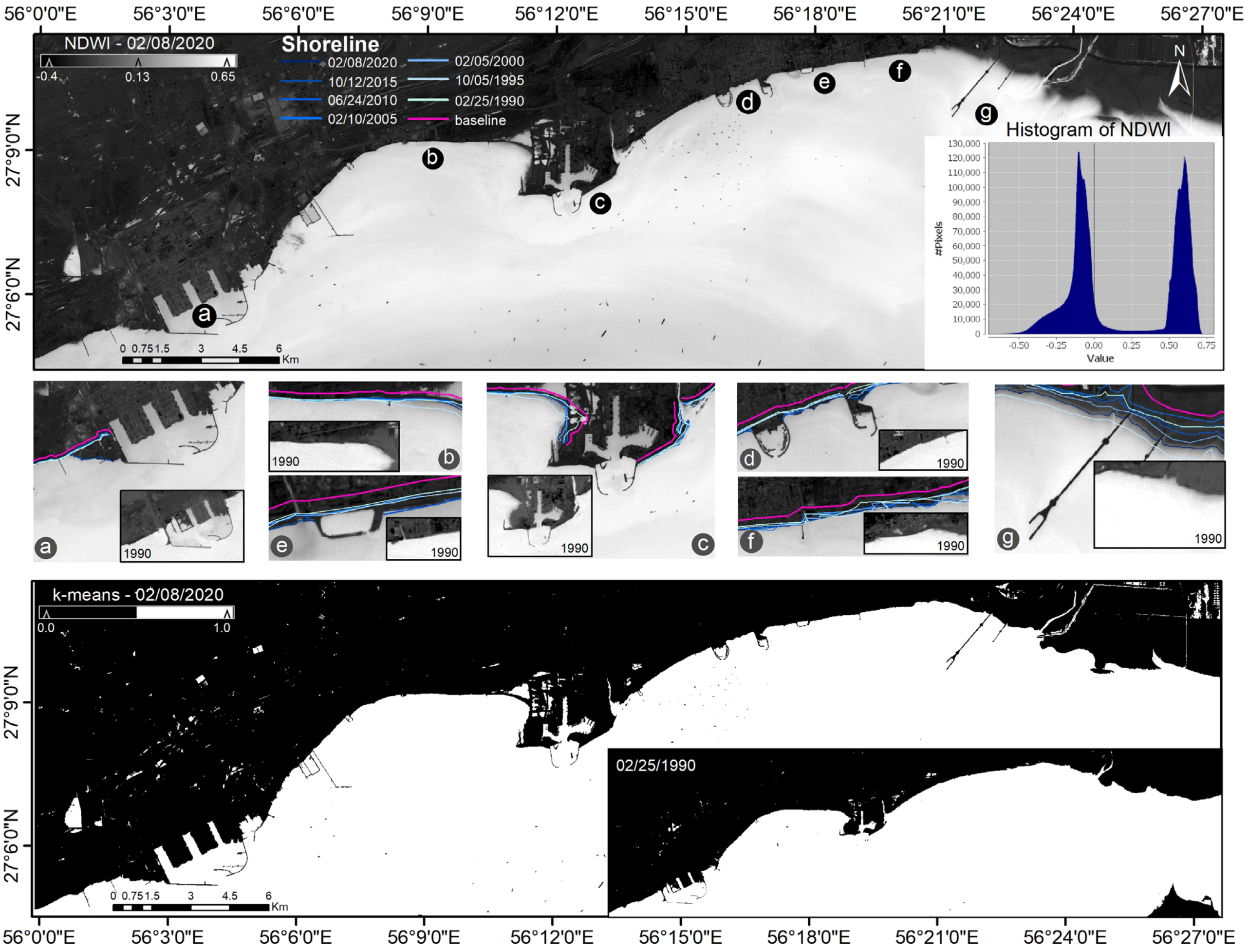

Figure 2: Image obtained by applying the NDWI index: positive values are for water features and negative values are for land. Boxes "a" to "g" show the shoreline changes from 1990 to 2020: a) The shoreline of Shahid Rajaee Port Complex, b) The shoreline of the western region of Shahid Bahonar port, c) Shahid Bahonar port, d) Shahid Haqqani ports and Poshte Shahr fishing port, e) A small marine structure, called a Nimdayere and Gorsouzan estuary, f) Khore Shilat, g) Nakhl e Nakhoda jetty, and the Shoor River estuary (to the east). The histogram of NDWI for 2020 shows a two-peak distribution that represents two feature types.

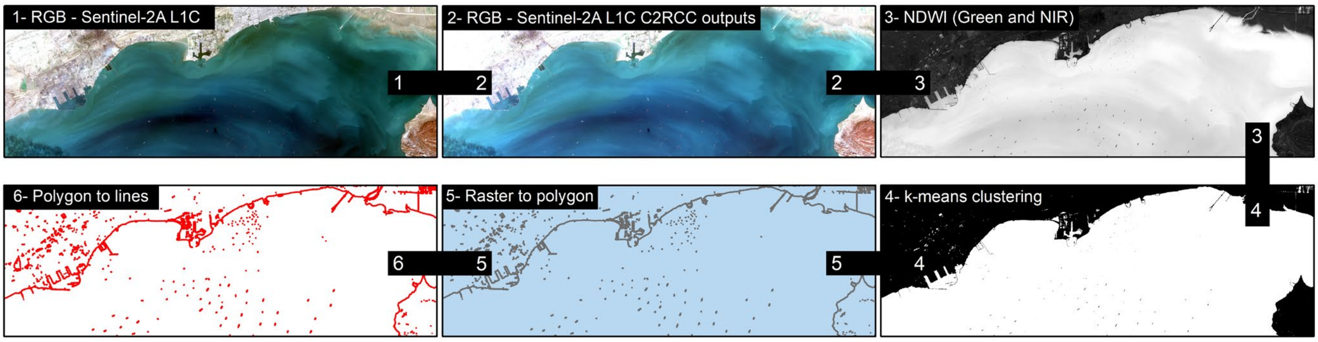

Figure 3: Shoreline extraction steps: 1) Images received from the Sentinel-2A L1C satellite (as an example) in three visible RGB bands, 2) Atmospheric correction is applied using C2RCC algorithm, 3) NDWI index is applied using Green and NIR bands, 4) Clustering is applied by k-means method, 5) Converted binary image (0,1) to polygon, 6) Converted polygons to line

The Digital Shoreline Analysis System (DSAS) [50] has been used to examine historical shoreline changes. The DSAS v5.0 extension is based on ArcGIS, developed by the United States Geological Survey (USGS) to statistically calculate the rate of changes in shorelines. This tool has been used in several studies [4], [11], [50–54]. After shorelines preparation, it is necessary to create a baseline. For this purpose, the baseline is created using the buffer tool. Then transects are created with 10 m distance, so total number of transects became to 4361. With DSAS, distances between baseline and shorelines at each transect is calculated. Also, the rate of shoreline change calculated with the methods available in DSAS [55]. Net Shoreline Movement (NSM) and Shoreline Change Envelope (SCE) methods have been used to calculate the distances between baseline and shorelines at each transect. Linear Regression Rate (LRR) and End Point Rate (EPR) methods have been used to calculate the rate of shoreline change. NSM is the distance between the oldest and the youngest shorelines for each transect in meter (Equation 3). The SCE value represents the greatest distance among all the shorelines that intersect a given transect (Equation 4). The EPR is calculated dividing the distance of shoreline movement by the elapsed time between the oldest and the most recent shoreline (Equation 5) [50].

$$NSM = S_o - S_y \tag{3}$$

Distance (in meter) between oldest (S_o) and youngest (S_y) shoreline.

$$SCE = greatest\ distance\ (m)\ between\ all\ the\ shorelines \tag{4}$$

$$EPR = \frac{NSM}{Time\ between\ oldest\ and\ most\ recent\ shoreline} \tag{5}$$

Figure 4 shows all four methods used by the DSAS tool. As an example, transect ID 3187 (green transect in Figure 4) has been selected; the distance between the oldest (1990) and the youngest (2020) shorelines is 49.78 m, while the greatest distance between all the shorelines (2000 and 2020) is 50.52 m. Also, the EPR value for transectID 3187 is 1.655 m/yr but the shoreline change rate based on the LRR method is 1.39 m/yr. The LRR is actually the slope of the line according to the y = ax –b equation [50].

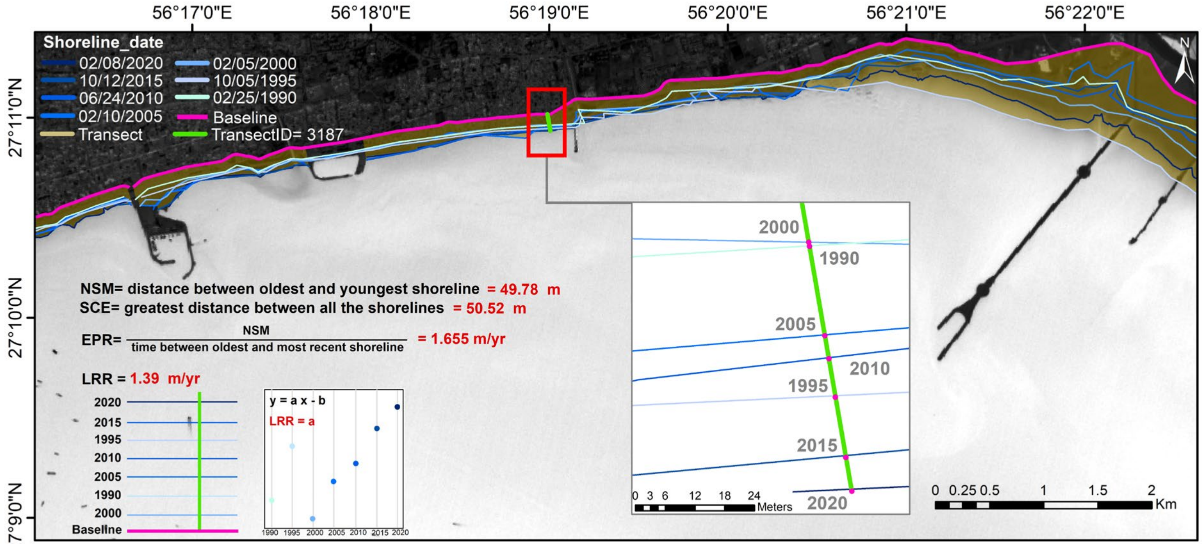

Figure 4: Schematic of the calculation of indexes; NSM, SCE, EPR and LRR in transects 3187

3. Results

3.1. Shoreline changes: 1990 -2020

According to Figure 2 major changes during these 30 years (from 1990 to 2020) can be described by comparing the two shorelines. During these years, a number of marine structures such as harbors, jetties and ports have been built, although some structures are more than 30 years old, such as Shahid Rajaee Port Complex and Shahid Bahonar port. Thus, it is expected that newly built structures as well as old structures have significant effects on shoreline changes. Following are a brief review of the shoreline changes during these 30 years presented in plots (a) to (g) in Figure 2.

a) According to Fig. 2a west side of Shahid Rajaee Port Complex is undergone major change which is due to the development of this port complex. These changes started since 2011, in a way that right now much of the west coast of the breakwater became landlocked.

b) This Part is located between Shahid Rajaee Port Complex and Shahid Bahonar port (Fig.2b). In this region, there are some industries such as Thermal Power Station of Bandar Abbas and the Special Industrial Zone Company of the Persian Gulf Mining and Processing Industry.

c) In Shahid Bahonar port complex (Fig.2c) shoreline changes are visible in both sides of the port over the years. However, the rate of change is higher in west side of the port. While due to the location of Khor Soro, in the east side of the port, more shoreline change in this side was expected.

d) The Poshte Shahr fishing port is developed in 2004, however the original structure of Shahid Haqqani ports existed since 1990 but has been reconstructed in 2000 (Fig2d).

e) Nimdayere structure (Fig2e) has been built since 2009 to develop beach tourism (water sports). The presence of Gorsouzan estuary in the west side of the structure seems to play main role in sedimentation processes.

f) This part consists of Khore Shilat and jetty structure (Fig2f). The presence of a jetty structure to the east of this water inlet is important due to the dominant pattern of east-west current in the area.

g) Nakhl e Nakhoda jetty and Shoor River estuary are shown in Fig.2g. Nakhl e Nakhoda jetty has been constructed since 2012. It seems that the presence of this jetty as a dam in the west of the Shoor River estuary as well as the prevailing current direction of the region from east to west (according to Reynolds [56]) play a major role in shoreline changes in this part.

3.2. Erosion and accretion

In order to estimate the amount of erosion or accretion, diagrams of shoreline changes as NSM (Figure 5) and SCE (Figure 6) are prepared. LRR (Figure 8) and EPR (Figure 9) diagrams are also plotted to estimate erosion and/or accretion rates. In all figures green shows maximum positive changes/rates and red indicates maximum negative changes/rates.

According to the NSM index, the largest shoreline change is related to the west of Shahid Rajaee Port Complex (fig.5a) and the Shoor River estuary area (Fig.5g), with more than 900 m recorded change. The changes in the west of region (Fig.5a) are due to the development of the Shahid Rajaee port complex. Besides, the drastic shoreline change in the Shoor River estuary could also be due to the sediment inflows. Shoor River estuary and Nakhl e Nakhoda jetty coast have been changed significantly (between 350 m and 900 m). The shoreline changes in western part of both Shahid Rajaee Port Complex and Shahid Bahonar port is positive and significant. Major part of this section is underdeveloped. It also consists of several water inflow branches. In recent years, the construction of a 3.5 km long jetty intensified the accretion trend in the region and surrounding areas. Based on a study by Najafabadi et al., [20] eastern part of Bandar Abbas coast (region "g" in this study) is at high risk considering the nature. Shoreline changes identified in region (g) confirms his findings. It is assumed that the main causes for this amount of shoreline changes are water inlet branches and underdeveloped area of this coastline.

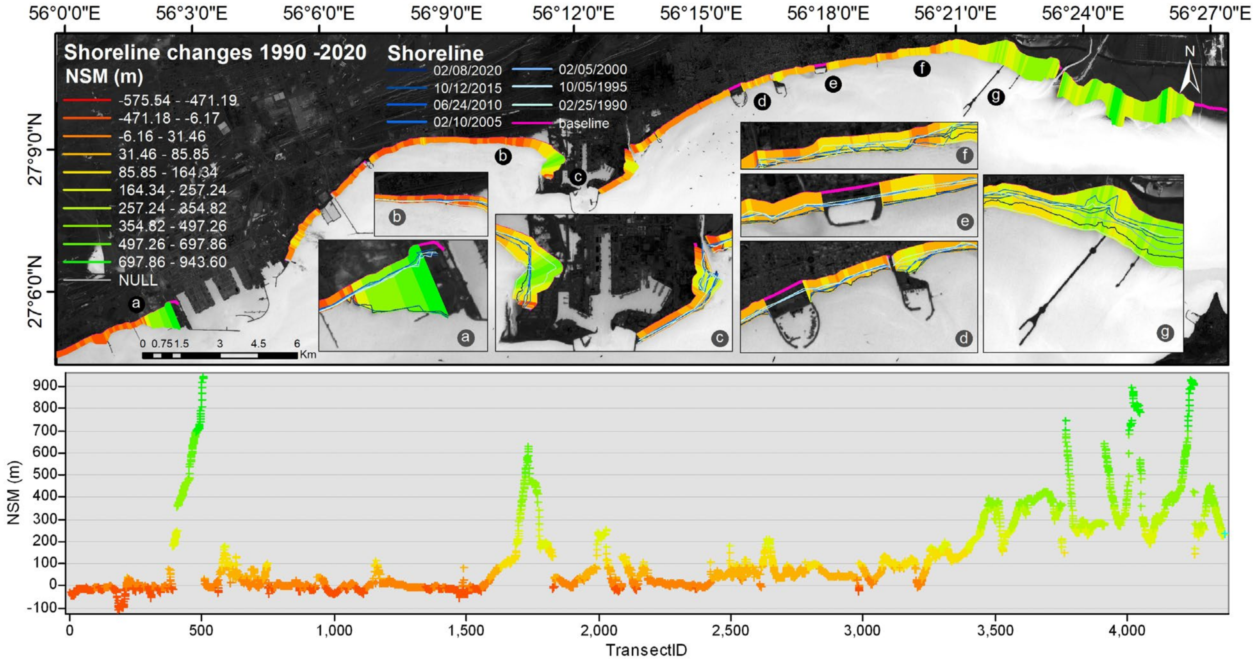

Figure 5: Shoreline changes (1990-2020) based on net shoreline movement (NSM) (m) along Bandar Abbas shoreline

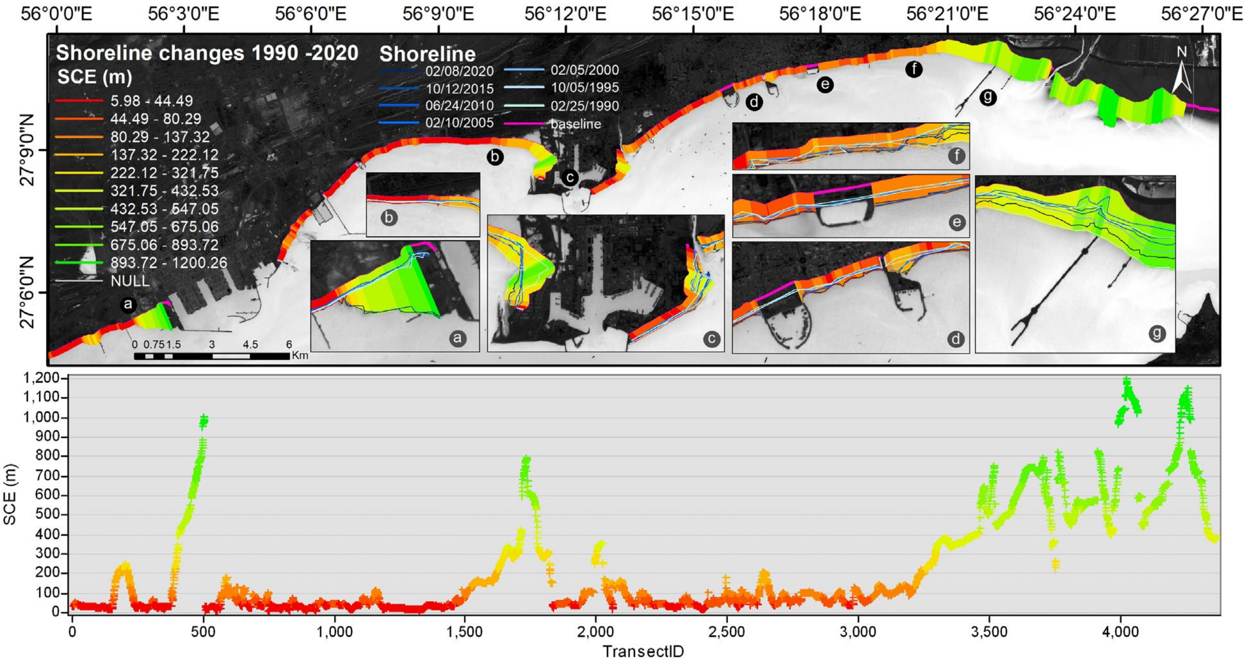

Figure 6: Shoreline changes (1990-2020) based on shoreline change envelope (SCE) (m) along Bandar Abbas shoreline

Diagram in Figure 7 shows that the SCE index is higher than the NSM index; meaning that the maximum value of SCE reaches up to 1200 m, while the NSM index is up to 900 m. The two NSM and SCE index has a correlation coefficient of 0.919, which indicates a strong correlation, but in the area "g" and "Shoor River estuary" (transectID approx. 3500 to 4000) there is a significant difference between the two indexes. According to the characteristics of NSM and SCE indexes, the reason for the difference between these two values is intermittent erosion and accretion, which is also highlighted by Himmelstoss et al., [55].

Both NSM and SCE diagrams show that zones (d), (e), and (f) have always had incremental changes during the years 1990 to 2020, although the amount of it was less than 100 m. While the shoreline around Shahid Haqqani ports and Poshte Shahr fishing port has changed approximately 200 m. Also, the area between Shahid Bahonar port and Shahid Rajaee Port Complex, which is the place of industrial activity (Fig.5 and 6 b), had a shoreline change of less than 100 m; even in some parts the changes are negative (Fig.5b and Fig.7 NSM index), which means erosion up to 50 m took place.

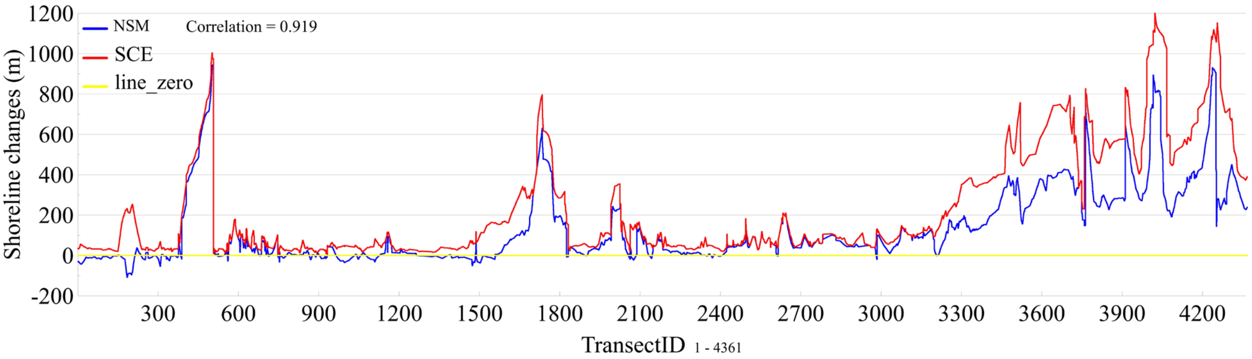

Figure 7: Comparison of NSM and SCE indexes in estimating shoreline changes from 1990 to 2020. The shoreline consists of 4361 transects with a distance of 10 m.

The LRR and EPR indexes have been used to estimate the rate of shoreline changes from 1990 to 2020 (over 30 years). Figures 8 and 9 show the shoreline changes based on the LRR and EPR index, respectively. The LRR and EPR indexes indicate major changes around marine structures, especially ports (as the two indexes, NSM and SCE showed). In short, on the west side of ports and breakwaters, the rate of shoreline changes is positive, which suggests sedimentation.

Comparing chart of LRR and EPR indexes (Fig.10), we found that the rate of change in the eastern region of Bandar Abbas (g) varies significantly, so that the correlation coefficient of these two indices is 0.429. But other shoreline sections have similar rates of change. A closer look at area (g) reveals that the final extracted shoreline (2020), is ahead of the old shorelines. This situation is most probably due to the construction of Nakhl e Nakhoda jetty. In addition, shoreline changes in the area varied from 1990 to 2015, indicating severe erosion and accretion. It seems that LRR index, despite its desirable features, is susceptible to deliver outlier effects and tends to underestimate the rate of change relative to other statistics, such as EPR. Such a shortcoming LRR is also reported by Dolan et al., [57] and Genz et al., [58]. Therefore, for detecting shoreline changes in this study results of the EPR index is taking to account.

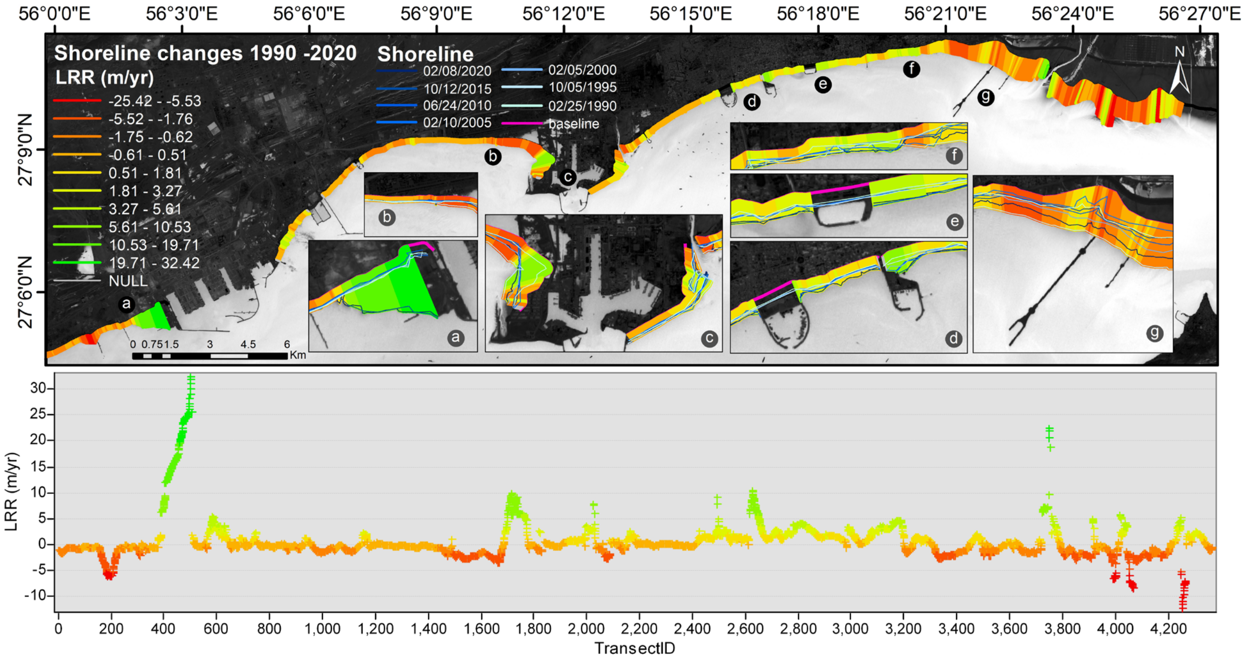

Figure 8: Rate of change in shorelines between 1990 and 2020 based on linear regression rate (LRR) (m/yr) along Bandar Abbas coastline

According to Fig. 8 and 9, the LRR and EPR indexes show that; high shoreline change rates are related to marine structures and ports. Also, the eastern part of Bandar Abbas has a high rate. In a few areas negative rate (erosion) has been detected, that corresponds to the part b (Fig 9 b); in which the maximum and minimum change rates are +3.79 m/yr and -1.7 m/yr, respectively, and the average change rate is about +0.010 m/yr (transectID 2200-3400). In areas where there is water inlet, the rate of change is variable, so water inlets and ports are sensitive areas that needs more attention. Areas (d), (e), and (f) generally have positive change rates of less than +5 m/yr. The highest and lowest rate of change are +10.75 m/yr and -0.65 m/yr, respectively, and the average rate of change is +2.35 m/yr (transectID 800-1500). This shows that; this part of the shore, which is an urban area, did not experience severe accretion, and coastal development and land reclamation had a low rate. The most important and sensitive parts of Bandar Abbas shore are Nakhl e Nakhoda jetty and Shoor River estuary, where the maximum and minimum rates of change are +31.07 m/yr and +4.83 m/yr, respectively, and the average rate is +12.34 m/yr (transectID 3400-4361). Therefore, any further coastal development and marine construction in this specific area should be evaluated more obsessively. It can even be said that the construction of Nakhl e Nakhoda jetty has increased the sensitivity of this region.

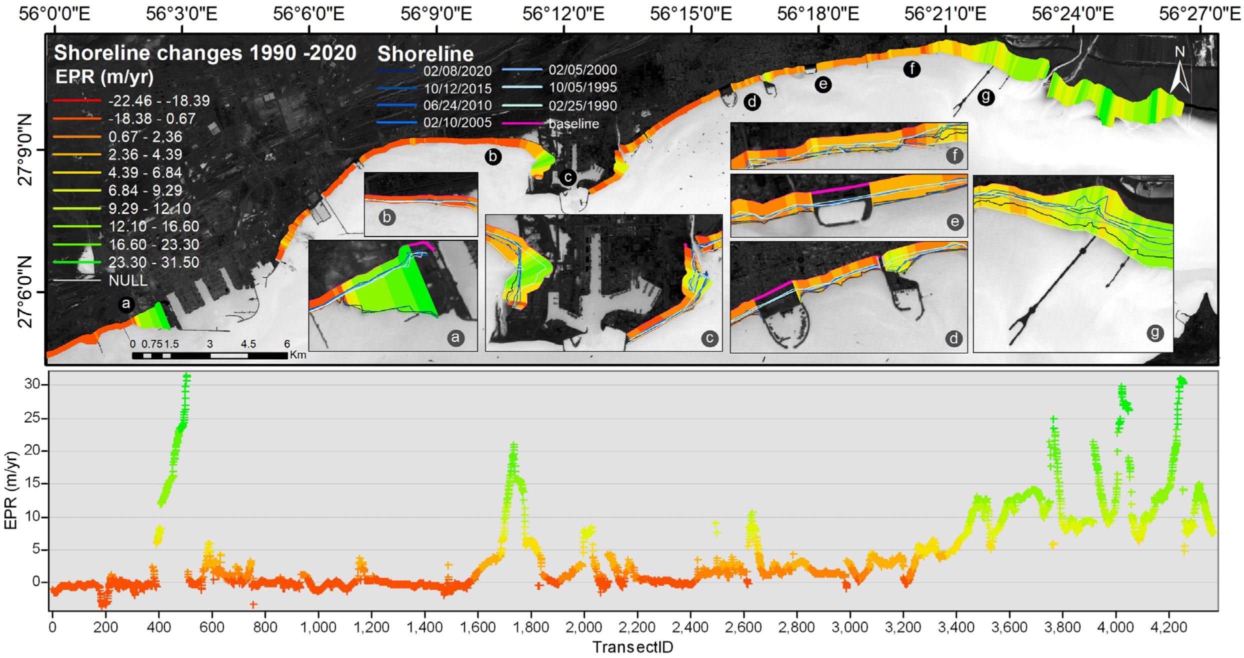

Figure 9: Rate of change in shoreline between 1990 and 2020 based on end point rate (EPR) (m/yr) along Bandar Abbas coastline

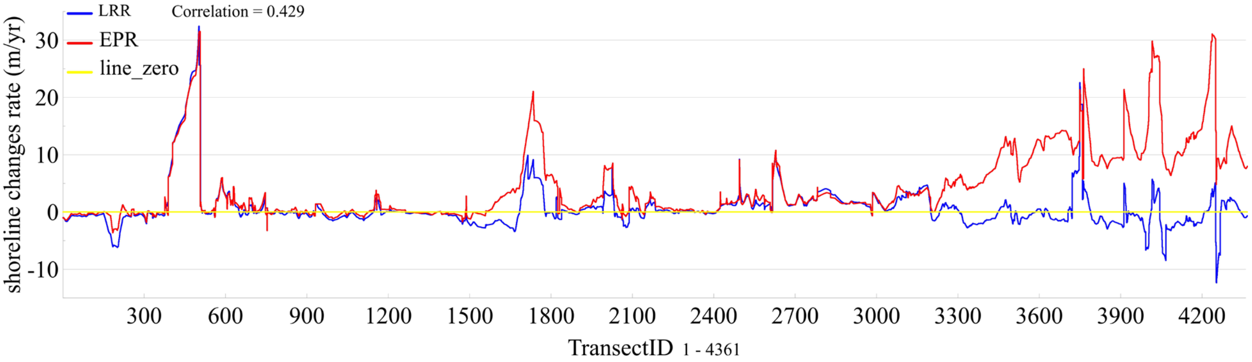

Figure 10: Comparison of LRR and EPR indexes, for estimating rate of change in shorelines of Bandar Abbas from 1990 to 2020. The shoreline consists of 4361 transects with a distance of 10 meters.

4. Discussion

Considering EPR index, the rate of shoreline changes is classified into five classes. The range of these five classes is selected according to the erosion and accretion values (Table 3). The rate of change of less than -0.5 m/yr is considered as erosion class, the highest erosion rate in this class is -3.61 m/yr. The total shoreline length, with rate of less than -0.5 m/yr, is 2747.9 m, which is 5% of the total shoreline of the study area. As shown in Figure 11, erosion occurred between the Shahid Rajaee Port Complex and the Shahid Bahonar port, although there is also erosion on the west side of the Shahid Rajaee Port Complex. In addition, there is erosion at the entrance to Khor Soro. The rate of change between +0.5 and -0.5 m/yr is considered as a Low Changes class. According to the results a significant length of Bandar Abbas shoreline has a rate of Low Changes, about 12408.88 m, which includes 25% of the shoreline and corresponds to the distance between Shahid Rajaee Port Complex and the Shahid Bahonar port and east of Shahid Bahonar port. The rate of change between +0.5 m/yr and 10.5 m/yr classified as a Low Accretion class. This class has the largest share in the shoreline classification of Bandar Abbas, with about 25980.82 m. In fact, more than half of the shoreline of Bandar Abbas has a low Accretion rate (according to Table 3). Most of this class is related to the urban shoreline area, ie (d), (e), and (f) sections (see fig 2). The rate of change between 10.5 and 20.5 m/yr is classified as Medium Accretion class and covers a length of 6294.95 m (13% of the study area). According to Figure 11, the western regions of the two major ports Shahid Rajaee and Shahid Bahonar and a main part of the eastern port of Bandar Abbas (Nakhl e Nakhoda jetty and Shoor River estuary) are categorized in this class. The rate of change above 20.5 m/yr is classified as High Accretion, which includes only 4% of the shoreline (1863.42 m). This class is only observed in the west of the Shahid Rajaee Port Complex and the Shoor River estuary. In general, shoreline changes in urban areas can be classified as Low Accretion. The shore of the western region, which is the place of industrial activity, is also classified as

Low Changes. The eastern regions of Bandar Abbas can be categorized as High accretion (see fig 2).

Table 3: Shoreline classification according to the rate of change in shorelines (EPR index) of Bandar Abbas from 1990 to 2020.

Category	Shoreline classification	Rate of shoreline change (m/year)	Length (m)	Percentage of shoreline (%)
1	*Erosion*	-3.61 to -0.5	2747.97	5
2	*Low Changes*	-0.5 to 0.5	12408.88	25
3	*Low Accretion*	0.5 to 10.5	25980.82	53
4	*Medium Accretion*	10.5 to 20.5	6294.95	13
5	*High Accretion*	20.5 to 31.5	1863.42	4
	Total length		49296.05	100

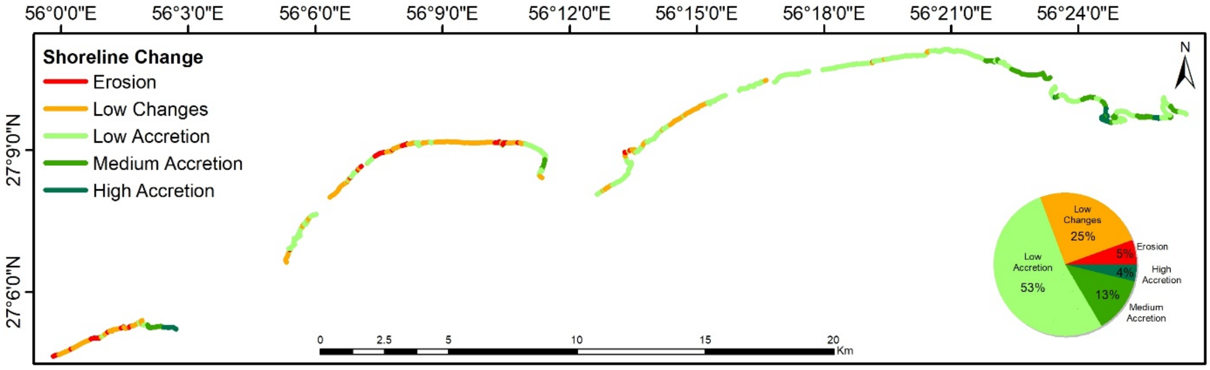

Figure 11: Rate of shoreline change (EPR index) according to five classes; erosion, low changes, low accretion, medium accretion and high accretion along the shoreline of Bandar Abbas.

5. Conclusions

Present study examines the rate of change in shorelines of Bandar Abbas city using satellite imagery over a period of 30 years (1990-2020). Landsat 5, 7, and 8 images, as well as Sentinel-2A images, were used to detect the shoreline changes along these years.

The results clearly show that Bandar Abbas shoreline is generally not subject to severe erosion or accretion. But parts of its coastline need specific attentions, especially when it comes to development goals. 53% of the shoreline of Bandar Abbas is in Low Accretion. The urban part of this shoreline can be mainly categorized in this class, where the rate of change is less than 10.5 m/year. Noteworthy to mention that coastal area within this sector is developing at a slow pace. It is suggested that the sensitivity of Gorsouzan estuary and Khor Soro be considered in case of development plans. In the eastern part of Bandar Abbas coast, the accretion rate is relatively high, so that the average rate of shoreline change is 12.34 m/yr, and the highest accretion has occurred in this area. Shoor River estuary sedimentation activity appears to be high and the presence of Nakhl e Nakhoda jetty exacerbates this problem. The western part of Bandar Abbas coast, which is the most active section in regard with industrial and ports construction, has a rate of change between -0.5 to +0.5 m/yr which means Low Change, however erosion occurred in some places. Along the whole shoreline of Bandar Abbas only 5% of the coastal erosion has been detected, which is mostly related to the western region of Bandar Abbas and the place of industrial activity.

In short, it is recommended to conduct sedimentation and erosion studies obsessively, in case of planning any further coastal development projects.

6.References

[1] K. S. S. Parthasarathy and P. C. Deka, "Remote sensing and GIS application in assessment of coastal vulnerability and shoreline changes: a review," ISH Journal of Hydraulic Engineering, vol. 00, no. 00, pp. 1–13, Apr. 2019, doi: 10.1080/09715010.2019.1603086.

[2] Tran Thi Van; Trinh Thi Binh, "Shoreline Change Detection to Serve Sustainable Management of Coastal Zone in Cuu Long Estuaries," International Symposium on Geoinformatics for Spatial Infrastructure Development in Earth and Allied Sciences. pp. 1–6, 2008.

[3] E. C. F. Bird and O. S. R. Ongkosongo, "Environmental changes on the coasts of Indonesia (resource management)." 1981.

[4] M. R. Muskananfola, S. Febrianto, and others, "Spatio-temporal analysis of shoreline change along the coast of Sayung Demak, Indonesia using Digital Shoreline Analysis System," Regional Studies in Marine Science, vol. 34, p. 101060, 2020.

[5] C. B. Boye, K. A. Addo, G. Wiafe, and K. Dzigbodi-Adjimah, "Spatio-temporal analyses of

shoreline change in the western region of Ghana," Journal of Coastal Conservation, vol. 22, no. 4, pp. 769–776, 2018.

[6] H. W. Blodget, P. T. Taylor, and J. H. Roark, "Shoreline changes along the Rosetta-Nile Promontory: Monitoring with satellite observations," Marine Geology, vol. 99, no. 1–2, pp. 67–77, 1991.

[7] A. T. K. Do, S. de Vries, and M. J. F. Stive, "The estimation and evaluation of shoreline locations, shoreline-change rates, and coastal volume changes derived from Landsat images," Journal of Coastal Research, vol. 35, no. 1, pp. 56–71, 2019.

[8] G. Mitri, M. Nader, M. Abou Dagher, and K. Gebrael, "Investigating the performance of sentinel-2A and Landsat 8 imagery in mapping shoreline changes," Journal of Coastal Conservation, vol. 24, no. 3, pp. 1–9, 2020.

[9] A. Novellino et al., "Mapping recent shoreline changes spanning the lateral collapse of Anak Krakatau Volcano, Indonesia," Applied Sciences, vol. 10, no. 2, p. 536, 2020.

[10] E. Tamassoki, H. Amiri, and Z. Soleymani, "Monitoring of shoreline changes using remote sensing (case study: coastal city of Bandar Abbas)," in IOP conference series: earth and environmental science, 2014, vol. 20, no. 1, p. 12023.

[11] D. Ghaderi and M. Rahbani, "Detecting shoreline change employing remote sensing images (Case study: Beris Port-east of Chabahar, Iran)," International Journal of Coastal and Offshore Engineering, vol. 3, pp. 1–8, 2020.

[12] V. Hadipour, F. Vafaie, and N. Kerle, "An indicator-based approach to assess social vulnerability of coastal areas to sea-level rise and flooding: A case study of Bandar Abbas city, Iran," Ocean & coastal management, vol. 188, p. 105077, 2020.

[13] M. Dadras, H. Z. M. Shafri, N. Ahmad, B. Pradhan, and S. Safarpour, "Six decades of urban growth using remote sensing and GIS in the city of Bandar Abbas, Iran," in IOP Conference Series: Earth and Environmental Science, 2014, vol. 20, no. 1, p. 12007.

[14] I. S. Yearbook, "Statistical center of Iran," Tehran, Iran, 2017. https://www.amar.org.ir/english/Population-and-Housing-Censuses/Census-2016-Detailed-Results (accessed Aug. 01, 2020).

[15] F. Allahyari, A. Behbahaninia, H. Rahami, M. Farahani, and S. Khadivi, "Development of a model for energy management in office buildings by neural networks (case study: Bandar Abbas)," International Journal of Environmental Science and Technology, vol. 17, no. 6. pp. 3279–3288, 2020, doi: 10.1007/s13762-019-02613-y.

[16] M. Valizadeh and A. Khoorani, "An evaluation of climatic conditions pertaining to outdoor tourism in Bandar Abbas, Iran," International Journal of Biometeorology, vol. 64, no. 1. pp. 29–37, 2020, doi: 10.1007/s00484-019-01790-2.

[17] F. Razkhaneh and M. Studies, "The Provision of Efficient Transport Services in the Iranian Maritime and Land Transport Interface." 2014.

[18] A. Jafari, S. Givehchi, and M. Nasrabadi, "Human Health Risk Assessment in Shahid Rajaee Container Terminal," Open Journal of Ecology, vol. 06, no. 11. pp. 686–698, 2016, doi: 10.4236/oje.2016.611063.

[19] M. Shirowzhan, M. Shanaki, M. H. Sebt, and H. N. Toosi, "Evaluating delay factors in the construction and operation of port operational areas (case study: Shahid Rajaee port complex)," Journal of Fundamental and Applied Sciences, vol. 8, no. 2. p. 732, 2016, doi: 10.4314/jfas.8vi2s.33.

[20] R. M. Najafabadi et al., "Identification of natural hazards and classification of urban areas by TOPSIS model (case study: Bandar Abbas city, Iran)," Geomatics, Natural Hazards and Risk, vol. 7, no. 1, pp. 85–100, 2016.

[21] H. Saeedi, "Availability of Venerid Clam, Amiantis umbonella as potential metal bioindicator in Bandar Abbas coast, the Persian Gulf," The Egyptian Journal of Aquatic Research, vol. 38, no. 2, pp. 93–103, 2012.

[22] M. Zare et al., "Outdoor investigation of air quality around Bandar Abbas-Iran oil refinery," International Journal of Environmental Health Engineering, vol. 1, no. 1, p. 9, 2012.

[23] M. H. Bordbar, M. Pedram, and S. Hassanzadeh, "Behaviour of surface atmospheric flow passing over the northeast of the Persian Gulf," Meteorological Applications, vol. 21, no. 2, pp. 271–277, 2014.

[24] E. H. Boak and I. L. Turner, "Shoreline definition and detection: a review," Journal of coastal research, vol. 21, no. 4 (214), pp. 688–703, 2005.

[25] T. Lillesand, R. W. Kiefer, and J. Chipman, Remote sensing and image interpretation. John Wiley & Sons, 2015.

[26] M. Louati, H. Saïdi, and F. Zargouni, "Shoreline change assessment using remote sensing and GIS techniques: a case study of the Medjerda delta coast, Tunisia," Arabian Journal of Geosciences, vol. 8, no. 6, pp. 4239–4255, 2015.

[27] A. Masria, K. Nadaoka, A. Negm, and M. Iskander, "Detection of shoreline and land cover changes around Rosetta promontory, Egypt, based on remote sensing analysis," Land, vol. 4, no. 1, pp. 216–230, 2015.

[28] United States Geological Survey, "EarthExplorer," 2020. https://earthexplorer.usgs.gov/ (accessed Aug. 02, 2020).

[29] M. Drusch et al., "Sentinel-2: ESA's optical high-resolution mission for GMES operational services," Remote sensing of Environment, vol. 120, pp. 25–36, 2012.

[30] X. Soria et al., "Validación de algoritmos para la estimación de la clorofila-a con Sentinel-2 en la Albufera de València," in Proceedings of the XVII

Congreso de la Asociación Española de Teledetección, 2017, pp. 289–292.

[31] ESA, “Copernicus Open Access Hub of the ESA,” 2020. https://scihub.copernicus.eu/ (accessed Aug. 02, 2020).

[32] ESA, “SNAP Download | STEP,” 2020. http://step.esa.int/main/download/snap-download/ (accessed Aug. 02, 2020).

[33] G. Navarro, I. Caballero, G. Silva, P.-C. Parra, Á. Vázquez, and R. Caldeira, “Evaluation of forest fire on Madeira Island using Sentinel-2A MSI imagery,” International Journal of Applied Earth Observation and Geoinformation, vol. 58, pp. 97–106, 2017.

[34] M. Pereira-Sandoval et al., “Evaluation of atmospheric correction algorithms over Spanish inland waters for sentinel-2 multi spectral imagery data,” Remote Sensing, vol. 11, no. 12, p. 1469, 2019.

[35] A. B. Ruescas, M. Pereira-Sandoval, C. Tenjo, A. Ruiz-Verdú, F. Steinmetz, and L. De Keukelaere, “Sentinel-2 atmospheric correction inter-comparison over two lakes in Spain and Peru-Bolivia,” in Proceedings of the Colour and Light in the Ocean from Earth Observation (CLEO) Workshop, Frascati, Italy, 2016, pp. 6–8.

[36] C. Brockmann, R. Doerffer, M. Peters, S. Kerstin, S. Embacher, and A. Ruescas, “Evolution of the C2RCC neural network for Sentinel 2 and 3 for the retrieval of ocean colour products in normal and extreme optically complex waters,” ESASP, vol. 740, p. 54, 2016.

[37] S. Sterckx, S. Knaeps, S. Kratzer, and K. Ruddick, “SIMilarity Environment Correction (SIMEC) applied to MERIS data over inland and coastal waters,” Remote Sensing of Environment, vol. 157, pp. 96–110, 2015.

[38] G. Chander, B. L. Markham, and D. L. Helder, “Summary of current radiometric calibration coefficients for Landsat MSS, TM, ETM+, and EO-1 ALI sensors,” Remote sensing of environment, vol. 113, no. 5, pp. 893–903, 2009.

[39] P. Tyagi and U. Bhosle, “Atmospheric correction of remotely sensed images in spatial and transform domain,” International Journal of Image Processing, vol. 5, no. 5, pp. 564–579, 2011.

[40] J. W. Rousel, R. H. Haas, J. A. Schell, and D. W. Deering, “Monitoring vegetation systems in the great plains with ERTS,” in Proceedings of the Third Earth Resources Technology Satellite—1 Symposium; NASA SP-351, 1973, pp. 309–317.

[41] S. K. McFeeters, “The use of the Normalized Difference Water Index (NDWI) in the delineation of open water features,” International journal of remote sensing, vol. 17, no. 7, pp. 1425–1432, 1996.

[42] H. Xu, “Modification of normalised difference water index (NDWI) to enhance open water features in remotely sensed imagery,” International journal of remote sensing, vol. 27, no. 14, pp. 3025–3033, 2006.

[43] G. L. Feyisa, H. Meilby, R. Fensholt, and S. R. Proud, “Automated Water Extraction Index: A new technique for surface water mapping using Landsat imagery,” Remote Sensing of Environment, vol. 140, pp. 23–35, 2014.

[44] C. Rashmi, S. Chaluvaiah, and G. H. Kumar, “An Efficient Parallel Block Processing Approach for K -Means Algorithm for High Resolution Orthoimagery Satellite Images,” Procedia Computer Science, vol. 89. pp. 623–631, 2016, doi: 10.1016/j.procs.2016.06.025.

[45] V. Jumb, M. Sohani, and A. Shrivas, “Color Image Segmentation Using K-Means Clustering and Otsu ’ s Adaptive Thresholding,” no. 9. pp. 72–76, 2014.

[46] A. Oliver, X. Muñoz, J. Batlle, L. Pacheco, and J. Freixenet, “Improving clustering algorithms for image segmentation using contour and region information,” 2006 IEEE International Conference on Automation, Quality and Testing, Robotics, AQTR, vol. 2. 2006, doi: 10.1109/AQTR.2006.254652.

[47] O. Ossama, H. M. O. Mokhtar, and M. E. El-Sharkawi, “An extended k-means technique for clustering moving objects,” Egyptian Informatics Journal, vol. 12, no. 1. pp. 45–51, 2011, doi: 10.1016/j.eij.2011.02.007.

[48] Y. Li and H. Wu, “A Clustering Method Based on K-Means Algorithm,” Physics Procedia, vol. 25. pp. 1104–1109, 2012, doi: 10.1016/j.phpro.2012.03.206.

[49] K. R. Ahmed and S. Akter, “Analysis of landcover change in southwest Bengal delta due to floods by NDVI, NDWI and K-means cluster with Landsat multi-spectral surface reflectance satellite data,” Remote Sensing Applications: Society and Environment, vol. 8, pp. 168–181, 2017.

[50] E. R. Thieler, E. A. Himmelstoss, J. L. Zichichi, and A. Ergul, “The Digital Shoreline Analysis System (DSAS) version 4.0-an ArcGIS extension for calculating shoreline change,” 2009.

[51] R. Bera and R. Maiti, “Quantitative analysis of erosion and accretion (1975--2017) using DSAS—A study on Indian Sundarbans,” Regional Studies in Marine Science, vol. 28, p. 100583, 2019.

[52] S. Roy, M. Mahapatra, and A. Chakraborty, “Shoreline change detection along the coast of Odisha, India using digital shoreline analysis system,” Spatial Information Research, vol. 26, no. 5, pp. 563–571, 2018.

[53] G. Qiao et al., “55-year (1960--2015) spatiotemporal shoreline change analysis using historical DISP and Landsat time series data in Shanghai,” International journal of applied earth observation and geoinformation, vol. 68, pp. 238–251, 2018.

[54] K. Nassar, W. E. Mahmod, H. Fath, A. Masria, K. Nadaoka, and A. Negm, “Shoreline change detection using DSAS technique: Case of North Sinai

coast, Egypt," Marine Georesources & Geotechnology, vol. 37, no. 1, pp. 81–95, 2019.

[55] E. A. Himmelstoss, R. E. Henderson, M. G. Kratzmann, and A. S. Farris, "Digital shoreline analysis system (DSAS) version 5.0 user guide," 2018.

[56] R. M. Reynolds, "Physical oceanography of the Gulf, Strait of Hormuz, and the Gulf of Oman—Results from the Mt Mitchell expedition," Marine Pollution Bulletin, vol. 27, pp. 35–59, 1993.

[57] R. Dolan, M. S. Fenster, and S. J. Holme, "Temporal analysis of shoreline recession and accretion," Journal of coastal research, pp. 723–744, 1991.

[58] A. S. Genz, C. H. Fletcher, R. A. Dunn, L. N. Frazer, and J. J. Rooney, "The predictive accuracy of shoreline change rate methods and alongshore beach variation on Maui, Hawaii," Journal of Coastal Research, vol. 23, no. 1 (231), pp. 87–105, 2007.

INTERNATIONAL JOURNAL OF
COASTAL & OFFSHORE ENGINEERING
IJCOE Vol.5/No. 2/Summer 2020 (65-70)

Available online at: www.Ijcoe.org

Design of Transit Capacity Development Model of Amirabad Port Special Economic Zone: A Qualitative Study

Maryam Kaveh[1], **Majid Fattahi** [2*], **Rahman Ghaffari** [3]

[1] PhD Student, Business Administration Department, Sari Branch, Islamic Azad University, Sari, Iran (kaveh.mry@gmail.com)
[2]Assistant Professor, Business Administration Department, Faculty of Humanities, Sari Branch, Islamic Azad University, Sari, Iran (* Corresponding Author) (majid.fattahi@iausari.ac.ir)
3 Assistant Professor, Public Administration Department, Faculty of Humanities, Sari Branch, Islamic Azad University, Sari, Iran (rghaffari@ut.ac.ir)

ARTICLE INFO

Article History:
Received: 20 July. 2020
Accepted: 02 Nov. 2020

Keywords:
Port
Transit
Amirabad Port
transit development algorithm
grounded theory (GT)

ABSTRACT

This study aims to identify an appropriate model for developing the transit capacity, known as an instrument that countries use in relation to their geographical locations to diversify their income sources. In international aspects, developing transit capacity can also provide a country with other advantages in foreign affairs. Moreover, it is necessary to develop transit by Iran because of reducing economic vulnerability and increasing deterrence against hostile activities of Iran's enemies. Therefore, transit opportunities and bottlenecks were identified in addition to reviewing previous studies and interviewing the experts. Considering the semi-structured and in-depth interviews given to 13 informed transit experts, this is a qualitative study in which the grounded theory was employed. Finally, the proper transit capacity development model was proposed by extracting causal, main category, intervening, and contextual conditions and outcomes.

1. Introduction

Todays, transit of goods is one of the most lucrative trades in the world and naturally the countries that are in the path of transit corridors can benefit the most from this trade (Mullighan & Rau, 2015). The transit of goods through a country will not only generate income economically, but also show the political credibility of the country in the international community, and in terms of security and relations with other countries in various fields of great importance for countries involved in transit (Poul Hansen, 2008). If a country is on the way to reach the consumer and the amount of goods transited through this route, the country will earn the same proportion of the cost of the goods (Rodrigue, & Notteboom, 2017). In this regard, in a study entitled Assistance to Latvia's GDP in international transport examined the services resulting from the transit of goods to Lithuania. The results of this study indicate that rail, sea, land, pipeline transit accounted for approximately 6.6% of GDP for 2010 (Bulis.A, Aleksis Orlovs, Roberts Škapars, 2011). Ports are the connecting lines that enable land-to-sea transport and serve as the basis for logistics, production, information transfer, and international trade, and can serve as a diving board for a country's economic development (SONG & Taylor, 2015)

Although it is now necessary for Iran to enter global and regional export markets and lay the foundations for Iran's non-oil exports in those markets, there are specific setbacks caused by the effects of various factors such as the unreal exchange rate, other structural constraints of Iran, and inconsistency with the governing structures of the world in different areas. In fact, the perception of these necessities and constraints highlights the fundamental importance of the tenth aspect of resistive economy policies where special attention is paid to transit and re-export of products (Iranshahi & Fakhrabadi, 2015).

The Islamic Republic of Iran is among the countries benefiting from decent transit advantages because of having a beneficial geographical location. Expanding the transportation network and reliable, efficient communications, this country can use these advantages to increase foreign exchange earnings and improve the strategic status in the region properly (Nazari et al., 2019). In other words, Iran's geopolitical status has potentially the highest capacity for intra-regional transit because of having land and sea borders with 15 countries and an approximate population of 400-500 million people in the neighboring countries (Hosseinpour, 2019). Located in the south of the Caspian Sea, Amirabad Port has tropical climate in comparison with the countries situated in the north, east, and west of this inland body of water; therefore, it can be considered the best route for the transportation of products from manufacturing countries in the East (China and the Indian Subcontinent) to consumer countries in Europe.

There is a theoretical and research gap regarding transit; in fact, there are only a few studies addressing the development of transit capacities in this region with respect to the potential opportunities for the transaction of products and services with the Commonwealth of Nations (Sayareh & Khosravani, 2019). Paragraph 4 of General Policies on the Sixth Economic Development Plan considers the importance of developing Iran's transportation transit with respect domestic capacities and potential. If the transit capacity of Amirabad Special Economic Zone is increased, the resultant earnings will definitely grow. It will then be possible to enhance countless capacities for employment in Iran by resorting to resistive economy policies in sanctions. The main research question is what will be the best model that can help develop transit capacities of Amirabad Special Economic Zone. How can this model be implemented?

2. Research Literature

2.1. International North-South Transport Corridor

After certain agreements were signed by Iran, Russia, and India in Saint Petersburg in 2000, the International North-South Transport Corridor was established. In fact, it is the most important corridor involving Iran's ports in transit. This corridor has now expanded by accepting eleven new members, namely Azerbaijan, Armenia, Kazakhstan, Kirgizstan, Tajikistan, Turkey, Ukraine, Belarus, Oman, Syria, and Bulgaria. The Islamic Republic of Iran has been selected as the country responsible for informing committed parties of new memberships in this agreement or withdrawal of each committed party. Designing this corridor, its founders decided to establish a kind of transit business communication between the markets of Southeast Asia, the Indian Ocean territory, and the Persian Gulf on the one hand and countries of Central Asia including the Caucasus and the Russian Federation as well as all of its surrounding countries, especially Scandinavia, on the other hand.

The starting point and destination of this corridor are located in Helsinki, Finland and Mumbai Port, India, respectively. Three major route have been defined between these two points; Iran is located on all three of these routes.

East of the Caspian Sea Route: Passing through the eastern coasts of the Caspian Sea and Kazakhstan, this route is divided into two branches, the first of which is older and was based on the railway network of the Soviet Union. This route passes through Kazakhstan, Uzbekistan, and Turkmenistan and enters Iran through Sarakhs. Inaugurated in December, 2014, the second branch of this route acts as a shortcut that enters Turkmenistan directly from Kazakhstan and then enters Iran through Incheboron. It is preferable to the first branch for the transit of products of Northern Europe, Russia, and Kazakhstan. This branch was developed in the Project Railway Corridor No.4 of the Economic Cooperation Organization.

West of the Caspian Sea Route: This route enters Iran from Azerbaijan; however, a part of it covering the railway between Astra-Rasht and Qazvin has not been completed yet. The other route goes from Armenia to the Black Sea; it inauguration is in progress under the Persian Gulf–Black Sea Corridor Agreement.

The Caspian Sea Route: This route is directly connected from Astrakhan Port in the north of the Caspian Sea to the northern ports of Iran, i.e. Amirabad Port and Anzali Port. However, Anzali Port has not been connected to this railway network yet.

Table 1 shows the route segments of this corridor. It takes 18 days to pass through this route which stretches for nearly 7340 km (Ports and Maritime Organization Outlook, 2018).

Table 1. Route Segments of North-South Corridor (Main Route) Outside Iran

Corridor Path		Corridor Segment
Joint routes (Railway and Road)		Helsinki – Moscow
		Moscow – Astrakhan
		Bandar Abbas – Mumbai
Maritime Route of the Caspian Sea	Via Anzali Port	Astrakhan Port – Bandar Anzali
	Via Amirabad Port	Astrakhan Port – Amirabad Port
Railway and Road Route of the West Caspian Sea (via Azerbaijan)		Astrakhan Port - Baku
		Baku – Astra
Railway and Road Route of the West Caspian Sea (via Armenia)		Georgia (Batumi) – Armenia (Meghri)
		Armenia (Meghri) – Jolfa Border
Railway and Road Route of the East Caspian Sea (via Kazakhstan-Uzbekistan-Turkmenistan)		Kazakhstan (Gano Shinko – Karakalpakiya) – Uzbekistan (Karakalpakiya – Bukhara) – Turkmenistan (Chardzhou - Sarakhs)
Railway and Road Route from the East of Caspian Sea (via Kazakhstan-Turkmenistan)		Kazakhstan (Ozon) – Turkmenistan (Barkat - Atrak) – Inchedoron

2.2. Transit Procedure Performance Analysis in Amirabad Port:

Amirabad Port was constructed in the North-South Corridor for transit development; therefore, it might face more demands for transit in the near future when Chabahar routes join the national transportation center in addition to improvements made in the regional business atmosphere.

It is obvious from Figure 1 that the transit load has an ascending trend in this port. In other words, it appears that this port is going through the early phases of transit load attraction and that its transit load share will grow gradually if other logistic systems are supportive.

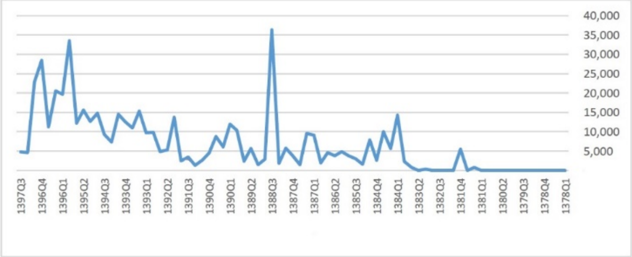

Figure 1. Transit Load of Amirabad Port from March 1999 to 2018 (digits, ton in season)

Table 2 shows the arrangement of transit load in Amirabad Port.

Table 2. Rate and Arrangement of Seasonal Transit Load in Amirabad Port from 2013 to 2018 (ton)

Container Transit		Dry Non-Food Bulk Transit		Dry Food Bulk Transit		General Transit		Season
Share of Container	Ton	Share of Dry Non-Food Bulk	Ton	Share of Dry Non-Food Bulk	Ton	Share of Total General Load	Ton	
67.81%	1،974	1.01%	1،828	0	0	0.33%	1،123	1392 Q3
43.59%	1،625	0	0	0	0	2.54%	8،216	1392 Q4
39.04%	1،213	0	0	0	0	1.71%	8،579	1393 Q1
39.50%	1،074	0	0	0	0	3.02%	14،265	1393 Q2
42.25%	526	1.42%	2،503	0	0	2.94%	8،008	1393 Q3
36.15%	342	0.31%	522	0	0	6.85%	11،727	1393 Q4
18.98%	374	0	0	0	0	4.58%	14،140	1394 Q1
7.37%	100	0	0	0	0	3.65%	7،288	1394 Q2
18.77%	95	0	0	0	0	6.51%	9،228	1394 Q3
42.89%	540	0	0	0	0	16.46%	14،292	1394 Q4
93.32%	559	0	0	0	0	9.64%	12،140	1395 Q1
63.38%	424	0	0	0	0	8.41%	15،220	1395 Q2
56.33%	445	0	0	0	0	13.51%	11،776	1395 Q3
81.13%	847	0	0	0	0	19.82%	32،664	1395 Q4
80.73%	955	0	0	0	0	12.96%	18،706	1396 Q1
41.51%	1،483	0	0	0.08%	453	11.63%	18،622	1396 Q2
49.54%	1،949	0	0	0	0	9.85%	9،347	1396 Q3
17.13%	1،475	0	0	0	0	23.37%	27،006	1396 Q4
39.56%	1،394	0	0	0	0	12.69%	21،462	1397 Q1
49.27%	1،514	0	0	0	0	1.91%	3،115	1397 Q2
30.62%	1،573	0	0	0	0	4.24%	3،274	1397 Q3

Accordingly, the transit load of Amirabad Port comes from general and container loads. The dry food and non-food products had a key role in transit loading and unloading. In the comparison drawn between general and container transits, previous performance shows that although the largest share of transit performance of Amirabad Port came from the general load in the past five years (12867 tons of general load performance of each season compared with the performance of 975 tons of transit containers in each season), transit containers account for nearly 46% of container performance of Amirabad Port. In other words, nearly half of the containers loaded and unloaded in Amirabad Port in the past five years were transit loads. However, this ratio is only 8.41% for general loads, a finding indicating that container load attraction to Amirabad Port depends greatly on the port transit demand (Ports and Maritime Organization Operation Statistics System, 2019).

3. Research Methodology

The research method in the present study is descriptive-survey according to the research subject and from the perspective of purpose and basic category, the research is applied. Also, among the two quantitative and qualitative approaches, the present research is a qualitative research. Examples of this research also include five hundred port and maritime transport specialists, which included operator companies, owners of goods, shipping lines, special economic zone investors, experts and maritime and port managers of the Ports and Maritime Organization.

The data collection tool was an interview. For this purpose, the activists in this field were interviewed individually and continued until the data was saturated and no new data was available. In the quantitative part of this research, using grounded theory method and using open, axial and selective coding steps, the data were analyzed and 93 basic concepts, 33 subcategories, 19 main categories were extracted, including causal conditions, contextual conditions, mediating and intervening conditions are strategies and consequences. Table 3 shows the characteristics of research participants separately:

Table 3. Characteristics of Interviewees

No.	Title	No.	Title
1	Board Member, Deputy of Port and Economic Affairs of Ports and Maritime Organization	8	Head of the Special Zone, Marketing, and Investment Office
2	Director of the Special Economic Zone and Amirabad Port	9	General Director of Amirabad Port Customs
3	Deputy of Port Affairs and Special Zone	10	Product Owner
4	Deputy of Maritime Affairs	11	Shipping Line Owner
5	Resource Planning and Development Deputy	12	Product Owner's Representative
6	General Director of Strategic Research and Analysis	13	Road Transportation Representative
7	Head of the Multidimensional Transportation and Logistics Office of Ports and Maritime Organization		

Regarding the optimal transit model, there are only a few studies worldwide having insufficient depth. For this purpose, it is necessary to employ qualitative methods. Since this study aims to propose a transit development model and identify transit challenges, opportunities, strategies and weaknesses, the grounded theory was employed along with Strauss and Corbin's systematic approach to discover the intangible aspects of the matter. In fact, this method can help propose a model based on different factors and their relationships. The causal factors are usually those events that affect phenomena. In other words, causal conditions affect the main category (Bazargan, 2016; Strauss & Corbin, 2013) and apply to the events that result in the occurrence or growth of the main research phenomenon. These conditions are prior to the main phenomenon on a temporal basis (Roshanel Arbatani et a., 2017).

4.Research Findings

4.1. Analysis

The interviews and coding processes helped identify two categories as causal factors: analysis of regional markets for the identification of potential capacities and participation in the international transit chain (See the Appendix).

4.1.1. strategies

According to experts' opinions and coding processes, the research strategies include identifying potential markets, reducing transportation and loading costs, employing multifaceted companies, synergy and coevolution of policies, futurology and futurism of markets, using tax incentives, utilizing advanced technologies, creating value-added on products, clientelism and transparency, developing and enhancing container transportation, wise diplomacy, finding optimal routes for product transit, using appropriate packaging, employing space-based technologies, transfer fund facilitation, and private sector participation (See the Appendix).

4.1.2. Contextual Factors

According to the interviews and coding processes, the contextual conditions of research include reducing bureaucracy, creating trust, homogenizing tariffs, coordinating organizations, facilitating rules, creating necessary infrastructures, enhancing transit culture, and complying with international standards (See the Appendix).

4.1.3. Intervening Conditions

The interviews and coding processes identified sanction as the intervening factor (See the Appendix).

4.1.4. Consequences

According to the interviews with experts and coding processes, the consequences were identified as enhancing domestic and foreign transit, creating income nationwide and for Mazandaran Province, establishing an attractive atmosphere for stakeholders, and removing product transit barriers (See the Appendix).

For the ultimate research purpose, i.e. designing a transit capacity development model for Amirabad Port Special Economic Zone, according to the Figure 2 and Figure 3, the grounded theory was implemented to extract a model from the extraction of interviews with experts.

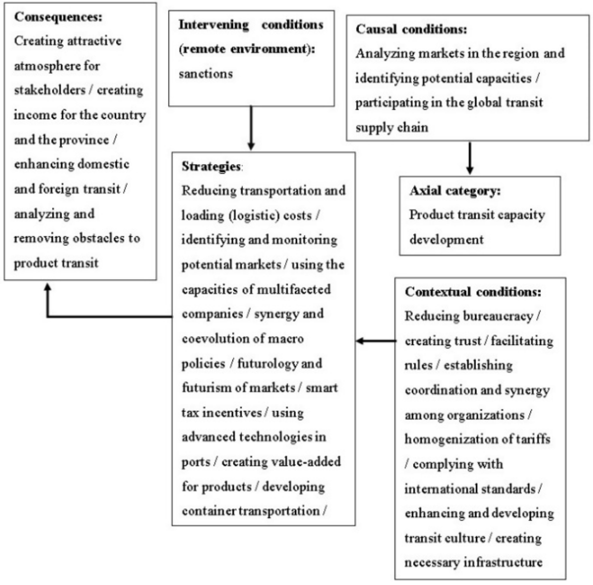

Figure2. Paradigmatic Model for Transit Capacity Development

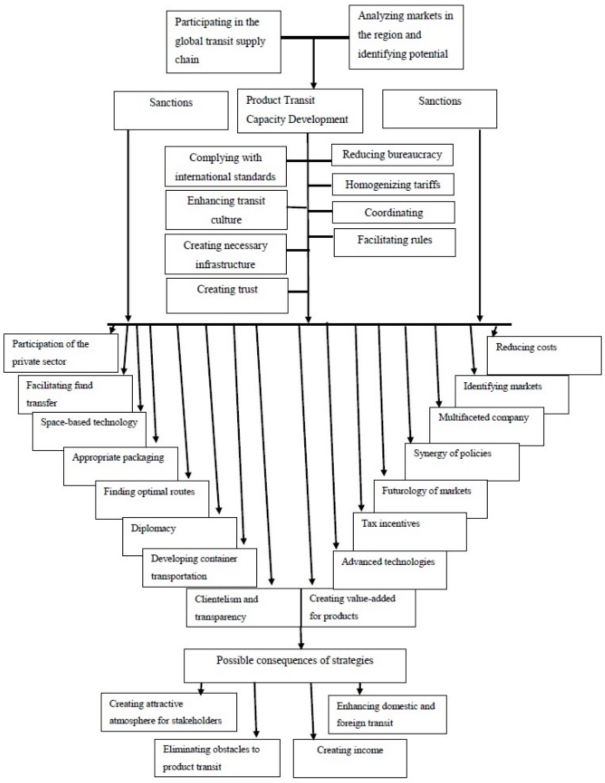

Figure3. Schematic Model for Transit Capacity Development

5. Discussion and Conclusions

This study tried to propose a product transit capacity development model for Amirabad Port Special Economic Zone. According to the results of coding and categorizing data in several steps, many factors should be taken into account in order to successfully implement the conceptual model of transit capacity development model. Moreover, some of these factors are related directly to other factors; therefore, the type of their relationships and effects should also be considered. The interviews indicated helped identify causal conditions, axial category, intervening conditions, contextual conditions, strategies, and consequences.

The causal conditions affecting transit capacity development include analyzing regional markets, identifying potential capacities, and participating in the international transit supply chain. The interviewees believed that finding and focusing on market potential could help develop the transit capacity. In addition, identifying the investment advantages in the Persian Gulf countries and other neighbors can provide golden opportunities for economic and commercial activists. At the same time, identifying and satisfying potential customers can help fulfill transit development. In the Caspian Sea Zone, there are only five countries meeting the sear, whereas the others are bordered by land. Hence, this constraint can be used as a potential capacity. Moreover, estimating the amount of load for Central Asia and analyzing product groups of regional countries can indicate what products these countries produce in addition to their needs and what deficits they face in different areas. This can play a major role in improving and developing Iran’s transit.

Regarding participation in the international transit supply chain, it should be stated that the third-generation ports are regarded as the logistic centers in the product supply chain. In fact, after products and raw materials are unloaded from stripes along with supplementary processes performed on them by repackaging and loading the stuff, they are then shipped to distribution and consumption centers. If economy globalization, supply chain management, logistics, use of modern technologies in production factors and commerce between productions, processing, or product consumption production sites, and minimization of manufacturing costs are for the final producer and consumer, then the role of ports as the input and output bases of products are become more important every day than the last.

The sanction problem was identified as an intervening factor. In fact, sanctions can be considered one of the most important factors preventing transit development and reducing national income through the transit industry because international sanctions are now the most important obstacle to product transit by Iran. The relevant consequences include creating an attractive atmosphere for stakeholders, creating income for the country, enhancing domestic and foreign transit, and analyzing product transit obstacles. According to the experts, adopting appropriate strategies and developing transit can increase the foreign exchange earnings of Iran and local incomes in Mazandaran Province. Therefore, inbound and outbound transit affairs thrive; as a result, it is possible to create an attractive atmosphere in the port for product owners, businesspeople, and investors.

The contextual conditions include reducing bureaucracy, creating trust, facilitating rules, complying with international standards, infusing coordination and synergy into organization, providing necessary infrastructure, and enhancing and developing transit culture. Regarding the existing bottlenecks and setbacks, the interviewees talked about the bureaucracy of organizations and defined bureaucracy reduction and facilitation as an opportunity for organizations to accelerate the transit process. In addition, lack of occupational trust and honesty is another factor preventing container transportation and causing problems in transit development. Furthermore, there are cumbersome rules in transit affairs. If these rules are modified or facilitated, it will be possible to develop transit. Given the existing conditions, some of the rules can be localized and customized for specific ports. At the same time, changing some rules based on the political relationships of countries can help businesspeople select more reliable paths for their transit routes. It is recommended that rules or their intervals should be determined. Furthermore, product standard consistency of other countries with Iran can lay the foundations for product transit development.

For instance, product standard inconsistency between Russia and Iran resulted in the return of many agricultural products such as citrus or even chickens sent to Russia; thus, traders and businesspeople incurred heavy costs because they were not acquainted with the standards of the destination country due to the lack of proper market research.

6. References

1- Brooks, M. R., and Schellinck, T., (2015), *Measuring port effectiveness: what really determines cargo interests' evaluations of port service delivery,* Maritime Policy & Management, 42(7), p. 699-711.

2- Chou, C. C., (2010), *AHP model for the container port choice in the multiple-ports region*. Journal of Marine Science and Technology, 18(2), p. 221-232.

3- Chu, L., Fwa, T. F., and Nishima, H., (2013). *Container Port Operational Performance Assessment*, Journal of the Eastern Asia Society for Transportation Studies, 10, p. 2197-2209.

4- Corbin, J., and Strauss, A., (2008), *Basics of qualitative research: Techniques and procedures for developing grounded theory.*

5- Dutra, A., Ripoll-Feliu, V. M., Fillol, A. G., Ensslin, S. R., and Ensslin, L., (2015), *The construction of knowledge from the scientific literature about the theme seaport performance evaluation*. International Journal of Productivity and Performance Management, 64(2), p. 243-269.

6- Gutiérrez, E., Lozano, S., Adenso-Díaz, B. and González, T., (2015), *Efficiency assessment of container operations of shipping agents in Spanish ports*. Maritime Policy & Management, 42(6), p.591-607.

7- Pak, J. Y., Thai, V. V., and Yeo, G. T., (2015), *Fuzzy MCDM approach for evaluating intangible resources affecting port service quality.* The Asian Journal of Shipping and Logistics, 31(4), p.459-468.

8- Rezaei, J., Van Wulfften Palthe, L., Tavasszy, L., Wiegmans, B., and Van der Laan, F., (2019), *Port performance measurement in the context of port choice: an MCDA approach*. Management Decision, 57(2), p.396-417.

9- Shiau, T. A., and Chuang, C. C., (2015), *Social construction of port sustainability indicators: a case study of Keelung Port.* Maritime Policy & Management, 42(1), p.26-42.

10- Song, D. W., and Yeo, G. T., (2015), *A Competitive Analysis of Chinese Container Ports Using the Analytic Hierarchy Process*. Port Management.London. p. 339-359.

11- Wiegmans, B., and Dekker, S., (2016), *Benchmarking deep-sea port performance in the Hamburg-Le Havre range.* International Journal, 23(1), p. 96-112.

12- Yeo, G. T., Ng, A. K., Lee, P. T. W., and Yang, Z., (2014), *Modelling port choice in an uncertain environment*. Maritime Policy & Management, 41(3), p. 251-267.

13- Yeo, G. T., Roe, M., and Dinwoodie, J., (2011), *Measuring the competitiveness of container ports: logisticians' perspectives.* European Journal of Marketing, 45(3), p.455-470.

14- Iranshahi, S., and Fakhrabadi. N., (2015), *Transit, a bridge between land and coastal developing countries and a tool for achieving a sea-based resilient economy*, International Congress on Management, Economics and Business Development.

15- Sayareh. J., and Khosravani. E., (2019), *Identification and Prioritization of Factors Affecting the Attraction of Regular Container Shipping Lines to Ports (Case Study: Shahid Rajaei Port).* Transportation Research Journal,16(1).

16- Arbatani, T., Hasangholipor, T., Ebrahimipour, H., and Ramazani, M., (2016), *Providing a Suitable Model of Advertising for Exporting Non-Oil Products of East Azarbaijan Province to CIS Countries.* International Business Management, 15(10),p. 2935-2940.

17- Mullighan, S. and Rau, J., (2015), *The Integrated Transport and Land Use Plan*, Government of south Australia.

18-Poul Hansen, L., (2008), *Facilitating Cross-Border Movement of Goods: A Sustainable Approach,* Conference on Trade and Development (UNCTAD), p. 67-76.

19-Rodrigue, J. P., and Notteboom, T., (2017), *Transport Costs. The Geography of Transport Systems, Fourth Edition.*

20-Bulis, A., Orlovs, A. and Škapars, R., (2012), *Reliability and Statistics in Transportation and Communication,* Contribution of International Transit Transport to Latvian GDP, (12), p. 128–135.

21-SONG, Y., Yue, W. L., and Taylor, M. A., (2015), *The role of transportation in logistics chain*, Eastern Asia Society for Transportation Studies.